

DISSERTATION

SOFT X-RAY LASER INTERFEROMETRY OF DENSE COLLIDING PLASMAS AND
PLASMA JETS

Submitted by

Jonathan Grava

Department of

Electrical and Computer Engineering

In partial fulfillment of the requirements

For the degree of Doctor of Philosophy

Colorado State University

Fort Collins, Colorado

Fall 2010

Doctoral Committee:

Department Head: Anthony Maciejewski

Advisor: Jorge Rocca

Carmen Menoni
Mario Marconi
Stephen Lundeen

ABSTRACT

SOFT X-RAY LASER INTERFEROMETRY OF DENSE COLLIDING PLASMAS AND PLASMA JETS

This dissertation describes the study of dense plasmas created by laser irradiation of solid targets of various geometries using soft x-ray laser interferometry and hydrodynamic simulations. High contrast interferograms yielded electron density maps describing the evolution of several different plasmas that due to their high density gradients cannot be probed with optical lasers.

In a first series of experiments, the evolution of dense aluminum plasmas produced by laser irradiation of 500 μm diameter semi-cylindrical targets was studied. Plasmas created heating the cavity walls with optical laser pulses of $\sim 1 \times 10^{12} \text{ W cm}^{-2}$ peak intensity and 120 ps duration were observed to expand and converge on axis to form a localized high density plasma focus. Electron density maps were obtained using a 46.9 nm wavelength table-top capillary discharge soft x-ray laser probe in combination with an amplitude division interferometer based on diffraction gratings. The measurements showed that the plasma density on axis exceeds $1 \times 10^{20} \text{ cm}^{-3}$. The electron density profiles were compared with simulations conducted using the hydrodynamic code HYDRA, which showed that the abrupt density increase near the axis is caused by the convergence of plasma generated at the bottom of the groove and the side walls during laser irradiation. At late times in the plasma evolution, extreme ultraviolet radiation is emitted along a narrow arc outside the cavity. Complementary measurements of this lower electron density region were performed using optical interferometry.

These measurements combined with two dimensional hydrodynamic simulations show that the emission results from a long lasting collisional shock that arises from the collision of counter-streaming plasmas originating from within the cavity and the surrounding flat walls of the target. The shock is sustained through tens of nanoseconds by the continuous arrival of plasma ablated by radiation emitted by the plasma itself.

A second series of experiments was conducted to study collisional aluminum plasma jets created by optical laser irradiation of triangular grooves at an intensity of $1 \times 10^{12} \text{ W cm}^{-2}$. The dynamics and formation mechanism of dense plasma jets are of interest for basic plasma physics understanding and in some cases astrophysics, and motivate this series of experiments. Series of high-contrast soft x-ray laser interferograms obtained with the 46.9 nm laser mapped the plasma density evolution of an initially narrow plasma jet that expands along the symmetry plane and evolves into a broader plasma plume with significant side lobes. Simulations reveal that the jet formation is initiated by accelerated material ablated from the vertex of the cavity and is augmented by the continual sequential arrival of wall material along the symmetry plane, where it collides and is redirected outward. Radiative cooling is identified as an important process in maintaining the collimation of the jet.

The last series of experiments demonstrates that high electron density ($n_e > 1.5 \times 10^{21} \text{ cm}^{-3}$) plasma jets can be generated by irradiation of cone targets with a laser pulse of only $\sim 1 \text{ J}$ energy. Two dimensional electron density maps of jets created by irradiation of conical Cu targets at an intensity of $6 \times 10^{12} \text{ W cm}^{-2}$ were obtained using soft x-ray laser interferometry. Radiation hydrodynamic simulations agree with experiments in showing that very high jet densities can be obtained with these relatively low laser pulse energies. The simulations revealed that radiation cooling of the plasma plays an important role in the jet evolution and collimation.

These results further establish the use of soft x-ray laser interferometry as a powerful diagnostic tool for dense plasmas.

Acknowledgements

The experiments performed herein could not have been done by one person alone, but was the result of a whole team of people that I would like to acknowledge. First and foremost, I would like to thank Dr. Jorge Rocca for the great opportunity that was presented to me. Jorge is a knowledgeable scientist that motivated me to achieve excellence in my research, and working with him has proved to be very rewarding.

A great thanks goes to Jorge Filevich and Michael Purvis, my two companions from the now-disbanded “Team B308”. They were always present to help and support the Frenchman, both at work and outside the lab. I also wish to thank Duncan Ryan for his help with the late night sessions spent taking the data presented herein. Last, I want to thank all the people I have interacted with at the ERC, for their moral support, be it simple jokes in the corridor or lengthy discussions about physics and science.

Thank you all,

Jono

Table of Contents

Chapter 1. Introduction	1
1.1. Motivations for the study of dense plasmas.....	1
1.2. Plasma definition, characterization and classification	4
1.2.1. Definition	4
1.2.2. Plasma parameters and classification.....	7
1.3. Laser generation of dense plasmas	9
1.4. Techniques for measuring the electron density in dense plasmas.....	12
1.4.1. Index of Refraction of a plasma	12
1.4.2. Grid Image Refractometry (GIR).....	14
1.4.3. Optical Interferometry.....	17
1.5. Review of dense plasma jets studies	19
1.5.1. Plasma jets in space and in the laboratory	19
1.5.2. Dense plasma jets characterization	20
1.5.3. Review of laser-created dense plasma jets experiments	23
1.6. Conclusions.....	26
1.7. References:.....	28
Chapter 2. Soft x-ray laser interferometry of dense plasmas	32
2.1. Soft x-ray laser interferometry	32

2.1.1. Extending the limits of interferometry using SXRLs.....	33
2.2. Soft x-ray interferometers	36
2.2.1. Lloyd’s mirror soft x-ray laser interferometer	37
2.2.2. Fresnel bi-mirror configuration.....	38
2.2.3. Mach Zehnder soft x-ray laser interferometer.....	40
2.3. References.....	43
Chapter 3. Experimental Setup.....	46
3.1. Introduction.....	46
3.2. Main diagnostic: Soft x-ray laser interferometry	48
3.2.1. Diffraction Grating Interferometer (DGI).....	48
3.2.2. Probe beam: capillary discharge soft x-ray laser	51
3.2.3. Detection system	56
3.3. Complementary diagnostics.....	56
3.3.1. Visible interferometry	57
3.3.2. Spectrometer	58
3.4. Target geometries	58
3.4.1. Half-cylindrical targets	58
3.4.2. V-grooved targets.....	60
3.4.3. Conical targets.....	61
3.5. Irradiating laser	62
3.6. Data analysis.....	64

3.6.1. Fringe shift map to electron densities: 2D approximation	66
3.6.2. Fringe shift map to electron densities in 3D plasmas: Analytical Spline Abel Inversion (ASAI) technique	67
3.7. References.....	72
Chapter 4. Dynamics of colliding dense plasmas in semi-cylindrical cavities studied using soft x-ray and optical interferometry	75
4.1. Introduction.....	75
4.2. Soft x-ray interferometry of dense Al colliding plasmas	76
4.2.1. Experimental results.....	76
4.2.2. Discussion	80
4.3. Soft x-ray interferometry of dense copper plasmas	83
4.4. Study of bow shock formation and evolution in laser-created copper colliding plasmas .	87
4.4.1. Experimental results.....	87
4.4.2. Simulations and discussion	92
4.5. Conclusions.....	96
4.6. References.....	96
Chapter 5. Dynamics of a dense laboratory plasma jets investigated using soft x-ray laser interferometry	99
5.1. Plasma jets generated from v-shaped cavities.....	99
5.1.1. Introduction.....	99
5.1.2. Experimental results.....	101

5.1.3. Simulations and discussion	106
5.2. Generation of dense plasma jets from irradiation of conical cavities	117
5.2.1. Experimental setup.....	117
5.2.2. Experimental results and discussion	118
5.3. Conclusions.....	123
5.4. References.....	124
Chapter 6. Conclusions	129
Appendix A. Numerical Hydrodynamic simulations	132
A.1. Discretization and meshing techniques	133
A.1.1. Meshing: Eulerian method	133
A.1.2. Meshing: Lagrangian method	134
A.1.3. Meshing: Arbitrary Lagrangian Eulerian (ALE) method.....	134
A.2. Fluid hydrodynamics: a basic description for plasmas	135
A.2.1. Equation for the motion of fluid	136
A.2.2. Equation of state (EOS)	138
A.2.3. Thermal conductivity	139
A.3. Radiation transport within the plasma	140
A.3.1. Overview of radiation	140
A.3.2. Collisional-radiative model.....	141
A.3.2. Radiation transport equation and the diffusion approximation.....	145
A.3.3. Rosseland mean opacities and the multi-group technique	148

A.4. References:	149
Appendix B. Analytic Spline Abel Inversion (ASAI) MATLAB Implementation	151

LIST OF FIGURES

Figure 1.1. Illustration of the Debye shielding in a plasma (a). The function to the right (b) represents the potential distribution near a grid held at a potential Φ_0	5
Figure 1.2. Various plasmas ordered by their temperature and density	8
Figure 1.3. Electron temperature and density in the plasma (in yellow) created by laser irradiation (incident from the right) onto a solid target (gray)..	11
Figure 1.4. Principle of Grid Image Refractometry (GIR)..	15
Figure 1.5. (a) X-ray laser GIR picture of the interaction region. (b) X-ray pinhole camera image of the plasma. (c) Two dimensional image and contour of the plasma obtained from the GIR data. (adapted from [20]).	16
Figure 1.6. Schematic of a Mach-Zehnder interferometer.	17
Figure 2.1. Ray refraction inside a plasma.....	34
Figure 2.2. Maximum plasma size probed for different laser probe wavelength as a function of the electron density.	35
Figure 2.3. Schematics of a Lloyd's mirror soft x-ray interferometer	37
Figure 2.4. Diagram of a Fresnel bi-mirror interferogram.....	39
Figure 2.5. Diagram of the Mach-Zehnder soft x-ray interferometer.	41
Figure 2.6. Schematic drawing of a Mach Zehnder diffraction grating interferometer (DGI)..	42
Figure 3.1. Schematic diagram of the complete experimental setup	47

Figure 3.2. Diagram of the diffraction grating interferometer (DGI)..	49
Figure 3.3. Picture of the tabletop Ne-like Ar 46.9 nm capillary discharge soft x-ray laser.	53
Table 3.1. Capillary discharge soft x-ray laser parameters.	53
Figure 3.4. Modified soft x-ray laser main spark gap..	54
Figure 3.5. Histogram of 128 consecutive laser-triggered SXRL shots..	56
Figure 3.6. Schematic view of the semi-cylindrical targets..	59
Figure 3.7. Schematic view of the V-groove targets.....	60
Figure 3.8. Schematic view of the conical target.	61
Figure 3.9. Schematic of the Titanium Sapphire (Ti:Sa) table top laser.....	63
Figure 3.10. First step of the data analysis of an Al plasma jet from a v-grooved target configuration.	65
Figure 3.11. Top view of the target, with soft x-ray travelling along the z axis, through the laser-created plasma.....	66
Figure 3.12. Abel inversion parameters on a transversal slice of cylindrically symmetric plasma jet.	69
Figure 3.13. Fringe shift map of a Cu plasma jet at 5.5 ns, before Abel inversion.....	72
Figure 4.1. Sequence of soft x-ray laser interferograms describing the evolution of plasmas created by irradiating a semi-cylindrical Al cavity with a 120 ps pulse at an intensity of 1.1×10^{12} Wcm ⁻²	78
Figure 4.2. Measured electron density maps of the aluminum plasma corresponding to the interferograms of Figure 4.1.	79
Figure 4.3. Calculations of the relative drift velocity and ion mean free path as a function of the angle between two parts of the plasma	82
Figure 4.4. Sequence of soft x-ray interferograms describing the evolution of Cu plasma created by irradiation of a semi-cylindrical cavity.	84

Figure 4.5. Electron density maps of Cu plasmas corresponding to the interferograms of Figure 4.4.	85
Figure 4.6. Time integrated self emission of a Cu plasma focus.	87
Figure 4.7. Sequence of interferograms depicting the evolution of the Cu bow shock.	89
Figure 4.8. Electron density maps obtained from the interferograms of Figure 4.6.	90
Figure 4.9. Sequence of interferograms and electron density maps for C plasmas.	91
Figure 4.10. Simulated electron density maps from the code HYDRA.	93
Figure 4.11. Velocity vector field map at 20 ns in the evolution of the copper plasma.	94
Figure 5.1. Time integrated emission of the laser-created aluminum plasma jet.	101
Figure 5.2. Sequence of soft x-ray interferograms mapping the evolution of laser-created aluminum plasma jets	103
Figure 5.3. Electron density maps corresponding to the interferograms of Figure 5.2.	105
Figure 5.4. Simulated electron density maps obtained with HYDRA.	107
Figure 5.5. HYDRA simulated maps of the electron temperature T_e of the laser-created aluminum plasma.	108
Figure 5.6. Time integrated aluminum spectra in the region between 3.5 and 7.5 nm.	110
Figure 5.7. Computed plasma pressure distribution for different times measured respect to the onset of the irradiation pulse.	111
Figure 5.8. Comparison of Al plasma jet experimental data (left column) to HYDRA simulations with radiation transport (center column) and for an optically thick plasma (right column).	113
Figure 5.9. HYDRA simulations of particles trajectories leaving the target at different times during the laser heating pulse.	115
Figure 5.10. Sequence of interferograms describing the evolution of the laser-created plasma jet	119

Figure 5.11. Two dimensional electron density maps of the laser-created plasma jets obtained from the interferograms using numerical Abel inversion.	120
Figure 5.12. Simulated electron density maps from the hydrodynamic code HYDRA.	122
Figure A.1. An energy level diagram depicting some of the atomic processes occurring between levels in an atom.	141
Figure A.2. Light can have its intensity I_v modified when traveling through a volume V of cross section dA and thickness ds	145

Chapter 1. Introduction

1.1. Motivations for the study of dense plasmas

Plasmas, also known as the fourth phase of matter, are the most common form of matter in the observable universe, accounting for 99.9% of the mass in our own Solar System [1]. The Sun, like all stars, is made of hot dense plasma. Interstellar clouds such as the Eagle nebula or the Crab nebula [2] are composed of dusty, cold plasmas. The solar wind is a stream of plasma constantly ejected from the Sun's upper atmosphere [3], and most of the astrophysical phenomena observed to date (supernovae remnants, Herbig-Haro objects, etc...) are some form of plasma. While the vast majority of plasmas are found in space, matter on our own planet can spontaneously reach the fourth phase under certain specific circumstances. Lightning and polar auroras are examples of low density plasmas that can naturally occur on earth. Industrial plasmas have been developed for arc welding torches and etching techniques, and the use of fluorescent light bulbs, a type of plasma discharge, is widely spread nowadays.

Plasmas of higher densities are also of interest for several applications, including the production of high average power incoherent extreme ultra violet (EUV) light for the lithography of the next generation of computer integrated circuits, lasers in the x-ray spectral region and controlled thermonuclear fusion. As these plasmas often have high density and steep gradients,

there is a need for developing accurate diagnostic tools and techniques for probing these hot dense plasmas.

An important application that requires a good understanding of dense plasmas is the generation of EUV and soft x-ray (SXR) light. Hot dense plasmas contain large densities of highly ionized atoms that under appropriate conditions can sustain large population inversion, ideal for lasing in the EUV and SXR spectral regions. Since these hot dense plasmas are short lived, the use of optical cavities is limited and the resulting lasers are in general single pass. The short duration of the laser upper levels requires the rapid and efficient delivery of the pump energy. High power optical infrared or visible lasers or fast electrical discharges are proven methods used to quickly deliver energy to the initial medium and create plasmas with the appropriate conditions for lasing. In order to engineer laser sources with high average power, the gain medium needs to be well understood and controlled, creating a strong motivation for the development of advanced plasma diagnostic techniques.

Another application that benefits from high precision diagnostics tools of dense plasmas is controlled thermonuclear fusion. One approach is to use high power lasers to rapidly bring a Deuterium-Tritium (D-T) pellet to very high temperatures (typically 100 million K), creating a very dense plasma. In this regime, Deuterium can collide and fuse with Tritium, releasing an enormous amount of energy that can be harvested for a variety of use, including the production of electricity. If controlled thermonuclear fusion is attained, it will be possible to generate a very large amount of cheap and clean energy. However, achieving the required plasma parameters (temperature, density, and confinement time) over a sufficiently large volume is very challenging and difficult to achieve. A large international effort is underway to reach ignition by use of intense laser called inertial confinement, but also using magnetic fields to maintain a lower density plasma for several seconds to reach fusion requirements, called magnetic confinement.

The development of methods capable to reach these plasma conditions requires proper tools to accurately measure important plasma parameters.

The study of dense plasmas is also important from the point of view of basic plasma physics and numerical simulations validation. Many linear and non-linear processes can take place in plasmas, depending on the temperature and density of the particles. Energy transport inside the plasma by conduction and radiation can be very complex. Computer codes are created to attempt to model the physics behind such dense plasmas, but are typically only valid for a limited range of density and temperature. Therefore, extensive experimental data is needed to verify the accuracy of these simulations. Laboratory-created plasmas can provide important information on temperature, electron density and mean ionization to compare with numerical code output. This stresses the important of accurate diagnostics tools for dense plasmas.

This dissertation focuses on the study of dense plasmas created by laser irradiation of solid targets of different shapes. Two dimensional density maps of the electron density of plasma focus and dense plasma jets were obtained experimentally using soft x-ray laser interferometry. The experimental results were combined with hydrodynamic simulations to infer the dynamics and formation mechanisms of these plasmas.

The next section describes the concept of plasma and the important parameters used to characterize and classify them. Section 1.3 focuses on the use of lasers to generate the dense plasmas of interest. Experimental techniques that were developed to measure the electron density in dense plasmas are described in Section 1.4, including soft x-ray interferometry, the main diagnostic method used in the experiments presented in this dissertation. After a brief description on dense plasma jets and the parameters used to characterize them, a review of the previous work in the field will be given in section 1.5.

1.2. Plasma definition, characterization and classification

1.2.1. Definition

A rigorous definition of a plasma can be stated as follows: a plasma is a *quasi-neutral* collection of *charged and neutral particles* which exhibits a *collective behavior* [4]. When a material is heated enough so that free electrons can acquire sufficiently high energy to ionize atoms, a plasma is created. It is typically composed of neutral atoms, ions in various excited states and free electrons. In order for this collection of particles to behave as a plasma, three conditions must be met: it must have a Debye length smaller than the characteristic size of the plasma, have a large enough number of particles within a Debye sphere (determined by the Debye length) and a large plasma frequency compared to the collision frequency. Those requirements are described next.

A fundamental characteristic of a plasma is its ability to shield out any electric potential that is applied to it. Suppose a positively charged ball is introduced inside a plasma, as shown in Figure 1.1a. This ball would attract particles of the opposite charge, resulting in a cloud of electrons immediately forming around the positively charged ball. In the case of a cold ionized gas, when no thermal motion is present, there would be as many charges in the cloud as in the ball and the shielding would be perfect. However, in the case of a plasma, the finite temperature means that some of the particles at the edge of the cloud would have enough energy to escape the electrostatic potential created by the ball, causing some finite electric fields to exist there. In that case, the approximate thickness of the charged cloud can be computed.

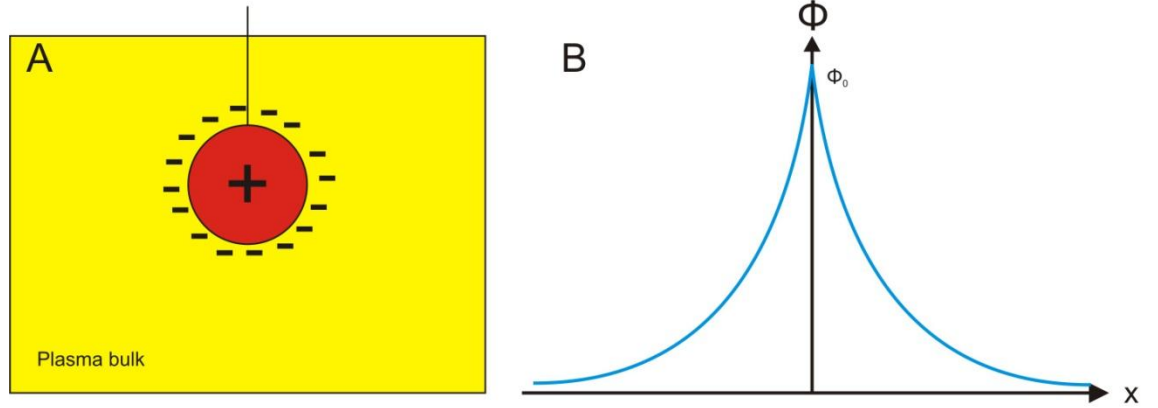


Figure 1.1. Illustration of the Debye shielding in a plasma (a). The function to the right (b) represents the potential distribution near a grid held at a potential Φ_0 .

Considering a plane at $x=0$ held at a potential Φ_0 by a perfectly transparent grid. The Poisson equation used to compute the potential distribution $\Phi(x)$ can be written as:

$$\epsilon_0 \nabla^2 \Phi = -e(n_e - n_i) \quad (\text{eq.1.1})$$

where ϵ_0 is the permittivity of free space (8.85×10^{-12} F/m), e is the charge of the electron (1.6×10^{-19} C), n_e is the electron density, and $n_i \sim n$ the bulk density far away from the charged grid. Solving this equation yields:

$$n_e = n \exp\left(-\frac{e\phi}{kT_e}\right)$$

where k is Boltzmann constant (1.38×10^{-23} J/K) and T_e the electron temperature inside the plasma. After substitution for n_e in equation (eq.1.1):

$$\epsilon_0 \frac{d^2 \phi}{dx^2} = en \left\{ \exp\left(\frac{e\phi}{kT_e}\right) - 1 \right\}$$

In the region where $\left| \frac{e\phi}{kT_e} \right| \ll 1$, the exponential can be expanded in a Taylor series, yielding:

$$\epsilon_0 \frac{d^2 \phi}{dx^2} = \frac{ne^2}{kT_e} \phi \quad (\text{eq.1.2})$$

From this equation, the Debye length is defined as:

$$\lambda_D = \left(\frac{\epsilon_0 k T_e}{n e^2} \right)^{1/2} \text{ (eq.1.3)}$$

and the solution for the potential distribution $\Phi(x)$ (illustrated in Figure 1.1b) is:

$$\phi = \phi_0 \exp(-|x|/\lambda_D)$$

The Debye length is a measure of the shielding distance in the plasma, also called the thickness of the plasma sheath. If the characteristic length of a plasma is much larger than λ_D , whenever a local concentration of charge arises, it will be immediately shielded out after a few Debye length, leaving the bulk of the plasma free of electric potentials. Notice that the Debye length decreases as the plasma density increases, since each layer of plasma will contain more electrons. The Debye length also increases with temperature: without any thermal motion, the charge cloud would collapse to an infinitely small layer. In the bulk of the plasma, for a characteristic plasma length $L \gg \lambda_D$, $\nabla^2 \Phi$ is small, $n_e \sim n_i$. The plasma is then *quasi-neutral*, in the sense that it is neutral within the bulk at a microscopic level, but electromagnetic forces can still influence its behavior at the macroscopic level.

The Debye shielding is only valid if a sufficient number of particles are present in the charged cloud. Using equation (eq.1.3), the number N_D of particles in a Debye sphere can be computed:

$$N_D = n_e \frac{4}{3} \pi \lambda_D^3 \text{ (eq.1.4)}$$

For $N_D \gg 1$, the plasma will have a *collective behavior*, with the charged particles inside the Debye sphere influencing many nearby particles.

The last condition that an ionized gas must satisfy in order to behave as a plasma is related to particle collisions. The frequency of the plasma oscillation ω has to be large compared to τ , the mean time between collisions with neutral atoms. When $\omega\tau > 1$, the motion of the

charged particles in a plasma is dominated by electromagnetic forces rather than by hydrodynamic forces as would be the case for ordinary gas kinetics.

1.2.2. Plasma parameters and classification

A plasma can be characterized by its density, temperature and degree of ionization. The plasma density refers to the electron density of the plasma, the number of free electrons per unit volume. For example, a nebula only has a density of a few atoms per centimeter cube. In comparison, the solid density of aluminum is $\sim 10^{23} \text{ cm}^{-3}$. The measured electron density of the plasmas studied herein range from 5×10^{17} to $1.5 \times 10^{21} \text{ cm}^{-3}$.

Inside a plasma, the particles can have many different velocities, with typically non uniform distributions compared to gas in thermal equilibrium. However, when a sufficient number of collisions occur, plasmas can reach a local thermodynamic equilibrium, and the velocities u of the particles can be describe by a Maxwellian distribution:

$$f(u) = A \exp\left(-\frac{1}{2}mu^2/kT\right)$$

where m is the mass of the particles, k is the Boltzmann constant and T is defined as the plasma temperature. The plasma temperature is usually given as kT and measured in eV or Kelvin. For example, a fluorescent light tube (which is a discharge plasma) has a temperature of $kT \sim 1.5$ eV (or ~ 20000 K). Higher temperatures (exceeding 1000 eV) can be reached in plasmas, such as the temperatures found inside the Sun.

Another parameter is the mean degree of ionization $\langle Z \rangle$: as the temperature gets higher, the plasma can reach higher states of ionization. Plasmas can range from a few times ionized to fully ionized.

There exist plasmas of various size, density and temperature. In the laboratory, plasmas sizes can be in the millimeter (or smaller) scale, while in space they can reach up to 10^{25} m in size, as is the case of intergalactic nebulae. Plasmas densities can cover over 20 orders of magnitude, with dusty plasma composing auroras having only a few atom per centimeter cube, up to the high densities ($> 10^{23}$ cm^{-3}) found in the core of stars. Plasma temperatures also span a large range, from a few hundred degrees in high pressure arcs to millions of degrees or higher for plasmas found in fusion applications or inside stars. Figure 1.2 categorizes different plasmas as a function of their densities and temperatures.

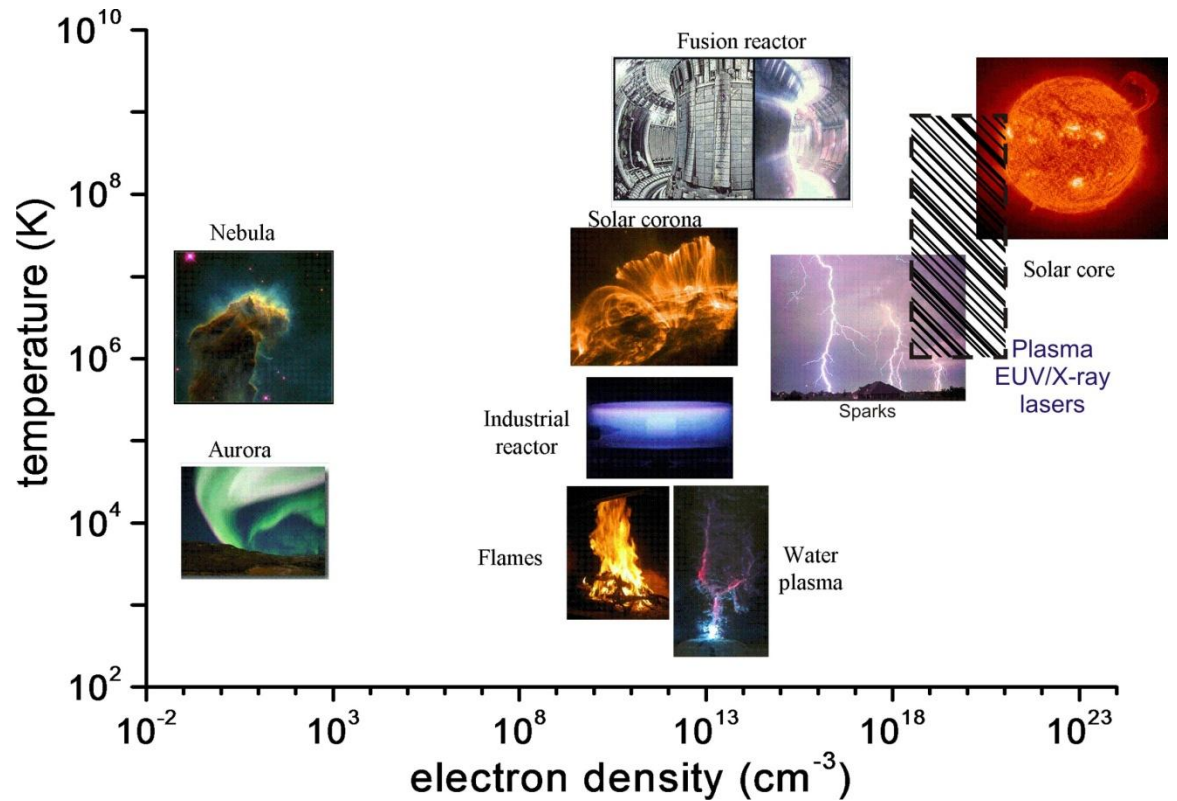


Figure 1.2. Various plasmas ordered by their temperature and density (adapted from: www.lpp.com).

This graph shows that plasmas span many orders of magnitude in both density and temperature. In particular, dense plasmas used to generate EUV/x-ray lasers and the plasma jets

described in this dissertation cover the temperature range of a few tens of eV ($\sim 10^6$ K) to a few keV ($\sim 10^9$ K), with electron densities reaching $\sim 5 \times 10^{18}$ to 10^{21} cm^{-3} .

The dense colliding plasmas and plasma jets of the experiments presented in this dissertation were created by irradiation of a solid target with a high energy short duration laser pulse. The physics of laser-generated plasmas is introduced next.

1.3. Laser generation of dense plasmas

Generating hot dense plasmas requires large amounts of energy to be transferred rapidly and efficiently to the initial material in its solid or gas phase. Such dense plasmas can be created for example using high energy density facilities built in the past decades [5-8]. These large lasers have high energy per pulse (> 100 J), short duration (ns to ps) but low repetition rates. More recently, the advent of powerful laboratory laser systems that can fit on several optical tables (i.e. table top lasers) have been used to generate dense plasmas [9-10]. While these lasers are typically a lot smaller with lower output energy (several joules), their very short pulse duration (ps to fs) and high repetition rate (several Hz) are a definite advantage for designing repeatable dense plasmas experiments such as those presented in this dissertation. The table-top short pulse high energy Titanium Sapphire laser used in the experiments presented herein is discussed in Chapter 3.

Table-top laser systems typically make use of low energy laser oscillator that provides a high quality beam. This seed is then subsequently amplified by propagating through and extracting energy from suitable crystals such as Neodymium doped glass (Nd:glass) or Titanium doped Sapphire (Ti:Sa) through a chirp pulse amplification (CPA) setup. Such lasers can have several amplification stages for increased output energy, and a pulse compression scheme can be

used to reduce the laser pulse duration. A series of optical elements focus the beam onto a solid target to increase energy deposition per unit area. At the same time, part of the beam can be used as diagnostics for the laser-created plasma.

As the laser pulse irradiates the solid target, the material at the surface is initially shocked by the laser beam. The shock wave travels into the material, increasing the surface temperature, and the resulting ablated mass results in the generation of a hot plasma. The rapid heating and ionizing of the target material sets up large pressure gradients near the target wall that force the plasma to expand away from the target. For irradiation intensities below $1 \times 10^{14} \text{ W cm}^{-2}$ (as is the case for creating the plasmas presented herein), energy is transferred from the laser into a thin layer of the plasma typically through the absorption mechanism of inverse Bremsstrahlung. In this process, also called free-free absorption, the free electrons of the initial plasma are accelerated by the electric field of the laser. The excited electrons absorb radiation as they are randomly scattered by the Coulomb field of the ions. This process converts the scattered energy into random thermal energy. The heating rate is proportional to the electron-ion collision frequency [11]. This energy transfer is most efficient in a small region where the electron density n_e is just below the critical density n_c . Laser rays impinging onto regions of the plasma with an electron density higher than the critical density will be reflected back. Close to the target surface, the electron density continues to increase thanks to thermal conduction from the plasma to the target surface.

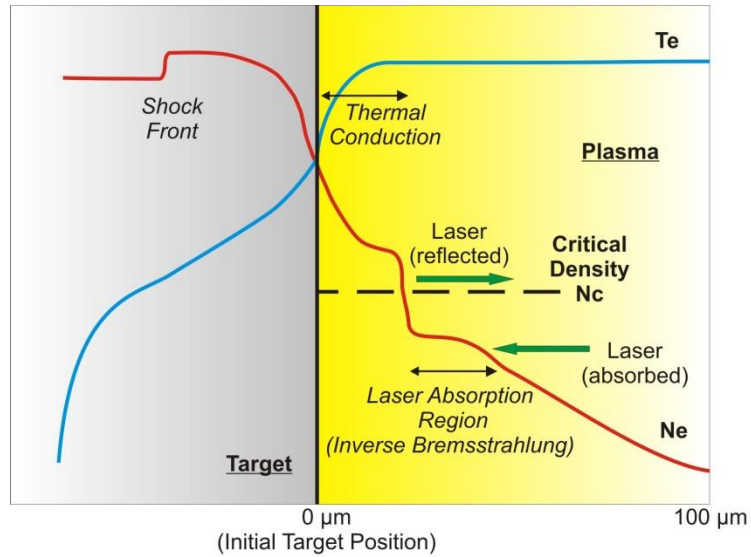


Figure 1.3. Electron temperature and density in the plasma (in yellow) created by laser irradiation (incident from the right) onto a solid target (gray). Thermal conduction is responsible for the increase in electron density closest to the target, while the laser energy is most efficiently absorbed in a small region before reaching the critical density through Inverse Bremsstrahlung. (Adapted from ref. [11]).

The choice of the target geometry, thickness and material plays an important role in the dynamics of the laser-created plasma. Conical targets [5], flat targets [12], hohlraum (for fusion application) and half-hohlraum [13], thin foils [14] or foam targets [15] made out of CH, carbon, aluminum, copper or gold are but a sample of the many choices available to create dense plasmas with very different properties and evolution.

In order to completely characterize laser-created dense plasmas and record their evolution and dynamics, it is necessary to use several diagnostic techniques. In the next section, several techniques are presented for characterizing one of the most important plasma parameters: the free electron density.

1.4. Techniques for measuring the electron density in dense plasmas

The electron density plays an important role in phenomena such as non-resonant absorption of radiation and collisional processes. In order to experimentally measure the electron density, the diagnostic method used must be accurate, reliable and robust. In the particular case of hot dense plasmas, high temperatures often prevent the possibility of internal diagnosis by material probes. Instead, radiation originating from physical processes inside the plasma can be observed and used to deduce information about the state of the plasma. Spectroscopy techniques are usually useful to compute the plasma temperature and electron density, but obtaining information on the latter from this measurement can be very complex [16-17].

Alternatively, techniques that rely on using electromagnetic waves travelling through a plasma can be used to deduce its electron density. Using electromagnetic waves to probe dense plasmas presents several advantages. It is a non-perturbing method that can determine internal plasma parameters without the use of a material probe. If the intensity of those waves is not too high, their influence on the plasma can be neglected but important information can still be obtained. An important plasma property for the measurement of the electron density is the index of refraction.

1.4.1. Index of Refraction of a plasma

Treating the plasma as a continuous medium in which current can flow and using Maxwell's equations in vacuum, an electromagnetic wave propagating through a plasma is described by the following equations:

$$\nabla \times E = -\frac{\partial B}{\partial t}, \quad \nabla \times B = \mu_0 j + \mu_0 \epsilon_0 \frac{\partial E}{\partial t} \quad (\text{eq.1.4.1})$$

where j represents the current flowing through the plasma. Then, the magnetic field B can be eliminated from equation (eq.1.4.1) to get:

$$\nabla \times (\nabla \times E) + \frac{\partial}{\partial t} \left(\mu_0 j + \mu_0 \epsilon_0 \frac{\partial E}{\partial t} \right) = 0 \quad (\text{eq.1.4.2})$$

Assuming the plasma is homogeneous in time and space, and the wave fields are small enough that the current is a linear function of the electric field, we can write:

$$j(k, \omega) = \sigma(k, \omega) \cdot E(k, \omega)$$

where $\sigma(k, \omega)$ is the conductivity of the plasma. Writing equation (eq.1.4.2) for a single Fourier mode:

$$k \times (k \times E) + i\omega(\mu_0 \sigma \cdot E - \mu_0 \epsilon_0 i\omega E) = 0$$

which can be rewritten as:

$$\left(k k - k^2 + \frac{\omega^2}{c^2} \epsilon \right) \cdot E, \quad \text{with}$$

$$\epsilon = \left(1 + \frac{i}{\omega \epsilon_0} \sigma \right) \quad (\text{eq.1.4.3})$$

Here ϵ is the dielectric tensor. Solving it for the transverse electric wave yields:

$$-k^2 + \frac{\omega^2}{c^2} \epsilon = 0$$

where ϵ is the plasma conductivity. This equation can be rewritten to show the refractive index of the plasma η :

$$\eta \equiv \frac{kc}{\omega} = \sqrt{\epsilon} \quad (\text{eq.1.4.4})$$

The next step is to compute the plasma conductivity and therefore its permittivity. A simple approach is to consider that the electrons in the plasma are taken at rest, except for the motions induced by the wave fields, and compute the resulting electron current to obtain the conductivity tensor. Following the derivations found in [18], the relationship between the index

of refraction of the plasma η , the plasma frequency $\omega_p = \left(\frac{n_e e^2}{\epsilon_0 m_e}\right)^{1/2}$ (eq.1.4.5) and the frequency of the travelling electric wave ω can be obtained:

$$\eta^2 = 1 - \frac{\omega_p^2}{\omega^2} \quad (\text{eq.1.4.6})$$

When an electromagnetic wave propagates through a plasma, there is a cutoff frequency called the critical density $n_c = \frac{\epsilon_0 \omega^2 m}{e^2}$ that directly depends on the wavelength of the wave.

Combining this equation and (eq.1.4.5) into (eq.1.4.6):

$$\eta^2 = 1 - \frac{n_e}{n_c}$$

Therefore, there is a relationship between η and the plasma density n_e , such that a direct measurement of the index of refraction can yield the electron density. Measuring the index of refraction can be done using light and one of various techniques such as grid image refractometry (GIR) and interferometry.

1.4.2. Grid Image Refractometry (GIR)

This technique, illustrated in Figure 1.4, makes use of a simple grid to effectively break the probe beam into a two dimensional set of “rays”, one for each point of the grid. In the presence of plasma, the rays will be refracted, resulting in a deformation of the grid. A typical ray, which would originate from a point P_0 if no plasma were present, is refracted through an angle θ_x in the (x,z) plane, and a corresponding θ_y in the (y,z) plane, and would appear to come from the point P_1 . The refraction angle of each ray (in the two planes perpendicular to the direction of propagation) can then easily be determined from the difference between the apparent positions of

the grid elements in two object planes divided by the distance between those planes. Knowing the refraction angle, the index of refraction of the plasma at this point can be calculated:

$$\theta = \frac{d\varphi}{dy} \frac{\lambda}{2\pi} = \frac{d}{dy} \int \eta dl$$

where $\varphi = \int \frac{\omega}{c} \eta dl$ is the total phase difference along the beam path [19]. Another method to determine the refraction angle from imaging only one plane in the plasma is to use a ray-tracing program [20].

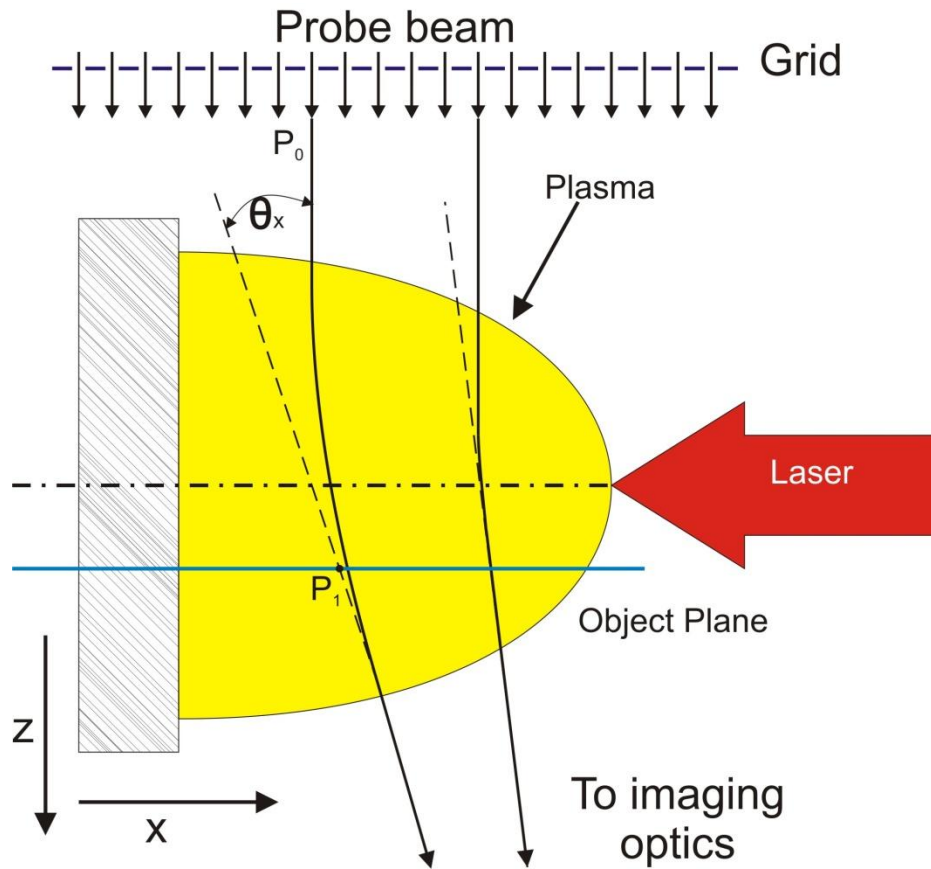


Figure 1.4. Principle of Grid Image Refractometry (GIR).

This technique has been used by Katahashi *et al.* [20] to measure the electron density in overdense plasmas. A plastic target was irradiated by $1.053 \mu\text{m}$ light at an intensity of $2 \times 10^{17} \text{ W/cm}^2$, resulting in a dense plasma. A soft x-ray probe beam (19.6 nm) was guided into the plasma using a flat mirror, and a spherical multilayer mirror imaged the plasma onto a CCD camera with $12\times$ magnification. Assuming the refractive index given by the electron density as $\eta^2 = 1 - \frac{n_e}{n_c}$, electron density profiles of the plasmas were evaluated from the distorted grid image using an iterative ray-tracing technique. Density profiles as high a 10^{22} cm^{-3} were measured using this method (Figure 1.5).

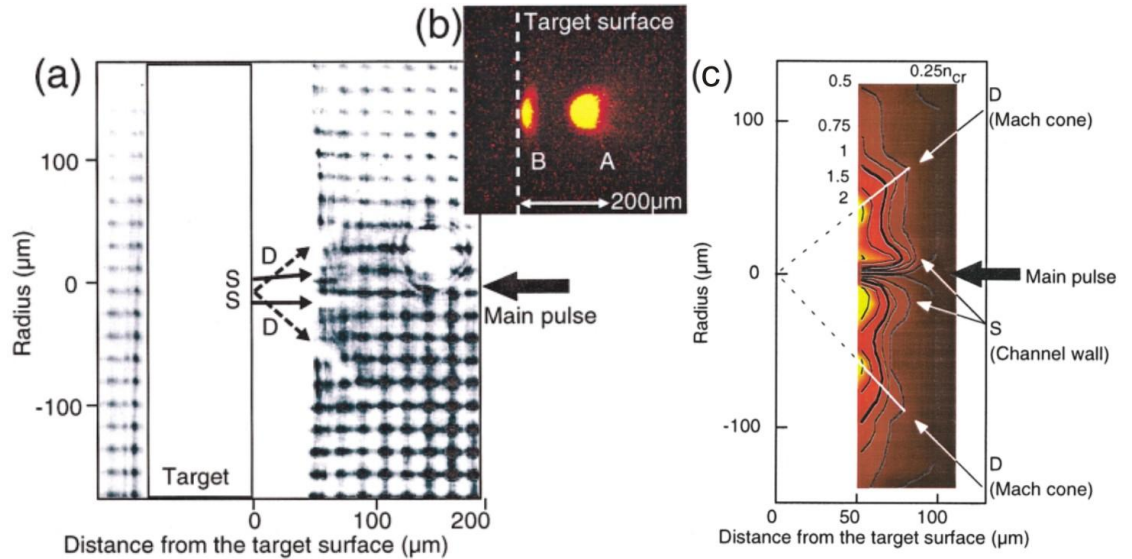


Figure 1.5. (a) X-ray laser GIR picture of the interaction region. (b) X-ray pinhole camera image of the plasma. (c) Two dimensional image and contour of the plasma obtained from the GIR data. (adapted from [20]).

GIR is a good technique that is especially valuable for plasmas with high density gradients, as larger refraction angles can be measured more accurately. However, this method suffers from several disadvantages. The spatial resolution of the measurement depends strongly

on the detection system and imaging optics, and errors can be introduced if the duration of the probe beam is larger than the time scale of the plasma hydrodynamic motion.

1.4.3. Optical Interferometry

The most widely used method for obtaining the electron density of hot dense plasmas is optical interferometry. An interferometer is a device in which two or more waves interfere by coherent addition of electric fields [21]. When the electric fields are in phase, constructive interferences are observed, whereas destructive interferences are created by out of phase electric fields. Consider a simple Mach-Zehnder interferometer in which monochromatic light of wavelength λ is separated by a first beam splitter then recombined together at the output, as shown in Figure 1.6.

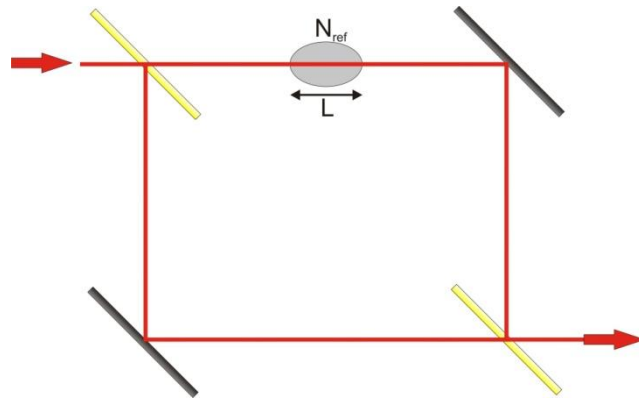


Figure 1.6. Schematic of a Mach-Zehnder interferometer. Light is split in two by a first beam splitter, and then each arm is redirected towards a second beam splitter, where they are recombined. The resulting fringe pattern will shift when introducing an object with index of refraction N_{ref} in one arm of the interferometer.

In the absence of plasma, any small phase difference between the two beams creates a pattern of alternating dark and light fringes corresponding to destructive and constructive interferences. The phase different between the two beams is given by:

$$\delta = \frac{2\pi}{\lambda} m$$

A bright fringe is obtained for $m = 0, 1, 2 \dots$ and a dark fringe for $m = \frac{1}{2}, \frac{3}{2}, \frac{5}{2} \dots$ Now, an object of length L and index of refraction η is introduced onto the path of one arm of the interferometer. This added phase in the beam path translates into a “shifting” of the fringes. The number of fringe shift is related to the index of refraction:

$$N_{fringe} = \frac{1}{\lambda} \int_0^L (1 - \eta) dl = \frac{1}{\lambda} \int_0^L \left(1 - \sqrt{1 - \frac{n_e}{n_c}}\right) dl$$

Therefore, the measurements of fringe shifts can lead to the values of the index of refraction, which in turn yield the electron density of the plasma.

Interferometry is a powerful metrology tool. Early interferometers used white light, such as the demonstration done by Young in his double-slit experiment in 1805 [22]. More recently, laser sources at visible and infrared wavelengths with high temporal and spatial coherence helped the development of robust and accurate interferometers. This optical interferometry technique has also spawned a wide range of application in engineering, physics and other fields including surface profiling [23], velocity measurements [24] and mechanical stress analysis [25]. Optical interferometry is particularly suited to measure the index of refraction of materials and therefore to study the electron density evolution in different types of plasmas [26-28]. This technique provides a robust method to measure the index of refraction η of a plasma, which is related to the

electron density n_e by $\eta = \sqrt{1 - n_c/n_e}$, where n_c is the critical density ($n_c = \frac{\epsilon_0 \omega^2 m}{e^2} \approx \frac{1.1 \times 10^{21}}{\lambda^2 (cm)}$,

m is the electron mass, e the electron charge, ω the frequency of the probe light and ϵ_0 the

permittivity in free space). The critical density is the density at which the frequency of the probing light is equal to the frequency of the plasma, and therefore at lower probe frequencies there is no propagation of light inside the plasma. The critical density is inversely proportional to the square of the probe's wavelength λ .

In principle one could expect to be able to probe densities up to the critical density. However, in practice there is a limit to the plasma densities that can be probed using a given wavelength, mainly because of refraction of the probe beam by the plasma, but also due to free-free absorption and the maximum number of fringe shift that in practice can be resolved by the detectors. These limitations can be overcome by reducing the wavelength of the probe beam, since all these effects scale down as the wavelength decreases. Therefore the use of soft x-ray laser as light source for interferometry is particularly well suited for studying hot dense plasmas. Soft x-ray laser interferometry is the main diagnostic method used to study the plasmas presented herein, and described in more details in Chapter 2.

1.5. Review of dense plasma jets studies

1.5.1. Plasma jets in space and in the laboratory

The formation and propagation of plasma jets is of interest to the astrophysics community. Highly collimated plasmas with length-to-width ratio well over 100 are everywhere in the universe, from active nuclei galaxies [2] to Herbig Haro objects [29]. Observational data, along with theoretical and computational modeling, have led to an improvement in their understanding, but questions still remain about both jet launching and propagation. In inertial confinement

fusion (ICF), the formation and stability of plasma jets are fundamental issues for achieving optimum x-ray generation and uniform target irradiation [30-31]. With the advent of powerful lasers, plasma jets can be studied in the laboratory and in some cases insight on their dynamics can be provided.

An advantage of experiments is the ability to produce plasma with a wide range of physical conditions for jets created in various geometries. Therefore, in order to characterize and compare them, a set of dimensionless parameters can be used. After defining those parameters, dense plasma jets experiments from the literature are reviewed.

1.5.2. Dense plasma jets characterization

Several dimensionless parameters can be computed in order to characterize plasma jets. This can be useful in comparing two systems that are orders of magnitude apart in size and lifespan but whose dynamics are similar in the hydrodynamic point of view. The dimensionless parameters discussed next find their root in astrophysics, but can still be applied to characterize laboratory dense plasma jets. In order to compare two similar hydrodynamic systems, a number of conditions must be met: both systems must behave as *fluids* where *heat conduction* and *viscosity* are *negligible*. To quantify those conditions and compare plasma jets, a number of dimensionless parameters can be computed. They are the localization parameter (also called collisionality), the Peclet number, the Reynolds number, the cooling parameter and the Mach number. Each of these parameters is briefly discussed next.

The localization parameter indicates how collisional the hydrodynamic system is. For a collisional system, the scales at which collisions occur must be small compared to h , the

characteristic length of the system. The localization parameter usually referred to as δ , is computed as:

$$\delta = \frac{l_c}{h}$$

Where l_c is the collisional mean free path, usually computed using the Braginski formula for ion-ion mean free path [32]. The localization condition then can be written as:

$$\frac{l_c}{h} \sim 3 \times 10^{13} \frac{T^2(\text{eV})}{\Lambda h n_i} \approx 8 \times 10^{-12} \frac{v_d^2}{\Lambda h n_i}$$

With n_i the ion density, Λ the Coulomb logarithm, $T \approx mv_d^2/2$ the temperature and h the characteristic length. The laboratory plasma jets created in the experiments presented in this dissertation are dense plasmas ($n \sim 10^{20}$ or higher) with typical characteristic length of mm or shorter, making those systems extremely collisional ($\delta \ll 1$).

The dimensionless parameter that describes the role of heat transport by particles within the plasma jet is the Peclet number P_e , corresponding to the ratio of heat convection to heat conduction. The Peclet number can be computed as:

$$P_e = \frac{r_{jet} v_{jet}}{\kappa}$$

Here r_{jet} and v_{jet} are the jet radius and velocity respectively, and κ is the thermal diffusivity for electrons, the main contributors to the heat conduction. Braginskii [32] gives the thermal diffusivity as:

$$\kappa \sim \frac{n_e T_e}{m_e} \tau_e$$

where n_e is the electron density, T_e the electron temperature, m_e the electron mass and

$\tau_e = \frac{6\sqrt{2}\pi^{3/2}\epsilon_0^2\sqrt{m_e}T_e^{3/2}}{\ln\Lambda e^4 n_e}$ the electron collision time. The thermal diffusivity can then be expressed

as:

$$\kappa(\text{cm}^2.\text{s}^{-1}) \sim 3.3 \times 10^{-3} \frac{ZT(\text{eV})^{5/2}}{\Lambda\rho(\text{g}.\text{cm}^{-3})}$$

Typical values for the Peclet number of laboratory dense plasma jets are large ($P_e > 10^{15}$), signifying negligible heat transport by conduction.

The next dimensionless parameter to discuss is related to the viscous effects in the plasma.

The Reynolds number R_e is computed as:

$$R_e = \frac{r_{jet}V_{jet}}{\nu}$$

where ν is the kinematic viscosity, the ratio between inertial and viscous forces. In the collisional limit, the kinematic viscosity is dominated by the ion viscosity, computed from Braginskii [32]:

$$\nu(\text{cm}^2.\text{s}^{-1}) = \nu_i \approx 2 \times 10^{19} \frac{T(\text{eV})^{5/2}}{\Lambda\sqrt{AZ^4}n_i(\text{cm}^{-3})}$$

Where A is the atomic number of the considered atoms, Z its mean ionization and T the temperature in eV. Typical Reynolds numbers in dense plasma jets range from ~ 10 to ~ 15000 . Since $R_e \gg 1$, viscous effects in the plasma can be neglected [33].

The effect of radiation in both astrophysical jets and laboratory plasma jets has been found to vary greatly, but can be an important mechanism of the plasma dynamics. In the case of supernovae expansion, the energy fluxes carried by radiation are small when compared to the material fluxes (i.e. a very fast expansion) of the system. In astrophysical jets, radiation cooling removes heat from the system, lowering the pressure inside the jet. This leads to narrower, more compact jets that maintain a high length to width aspect ratio for a long period of time. The same

effect has been observed in laboratory plasma jets when the atomic number of the material was varied [5]. In order to estimate the effect of radiation, the dimensionless cooling parameter χ can be computed:

$$\chi = \frac{v_{jet} \tau_{rad}}{R_{jet}}$$

The radiative cooling time τ_{rad} is defined as the ratio of the total kinetic plasma energy content to the radiative flux q_{rad} : $\tau_{rad} = \frac{3k(T_e n_e + T_i n_i)}{2q_{rad}}$ and v_{jet} and R_{jet} are the jet expansion velocity and radius. If the cooling parameter χ is smaller than one, radiative effects play a dominant role in the dynamics of the jet. For values of χ larger than one, the jet expands adiabatically, with little effect from radiation. The cooling parameter can be tailored experimentally by changing the target material, as radiation increases with higher Z atoms.

Another useful dimensionless parameter associated with jets is the Mach number

$$M = \frac{v_{jet}}{c_s}, \text{ where } c_s = \left(\gamma Z k T_e / m_i \right)^{1/2}$$

is the sound speed within the jet. Laboratory plasma jets have been produced with Mach number ranging from subsonic ($M < 1$) to highly supersonic ($M > 20$).

1.5.3. Review of laser-created dense plasma jets experiments

Over the past decade, a number of experiments were performed to study the dynamics of plasma jets in various regimes. Imaging, spectroscopy and interferometry technique have been used to characterize the plasmas in these experiments. Experimental results were used to validate various numerical simulations, and dimensionless jet parameters were computed and compared to astrophysical jets.

Farley *et al.* (1999) performed an experiment at Lawrence Livermore National Laboratory in which high Mach number, radiatively cooled jets were created [5]. Conical gold targets 800 μm in diameter were irradiated with five overlapping beams from the Nova laser at an intensity of $2 \times 10^{15} \text{ W/cm}^2$. Gated x-ray pinhole cameras recorded two dimensional, time resolved shadowgrams of the jet. A side-on diagnostic used an x-ray framing camera to record the plasma jet self-emission. High Mach number ($M > 10$), rapidly evolving jets with narrow profiles were measured. 2D LASNEX simulations were performed and showed good agreement with the experiments. Radiation cooling was demonstrated as an important cooling mechanism that help the jet retain its large length-to-width aspect ratio. The dimensionless parameters of this experiment scaled well to astrophysics in term of Mach number ($M \sim 20$) and cooling parameter ($\chi \sim 1$), but did not match well in density contrast. This experiment demonstrated the possibility to create dense plasma jets in a radiative regime in a laboratory environment.

Shigemori *et al.* (2000) [6] used a similar conical target configuration to create plasma jets using six beams of the frequency-doubled GEKKO XII Nd:Glass laser [34] at the Institute of Laser Engineering in Osaka University. The 1.6 mm diameter cone targets were uniformly irradiated at an intensity of $\sim 3 \times 10^{14} \text{ W/cm}^2$, creating high Mach number plasma jets in the radiative regime (i.e. the jets were strongly cooled by radiation escaping from the plasma). X-ray self-emission recorded for plasmas created on CH, aluminum, iron and gold targets clearly showed that higher Z material jets were more collimated. Two dimensional LASNEX simulations were performed to reproduce essential features of the experiment with good agreement, indicating that radiative cooling is an important mechanism for the formation of well-collimated jets. Computed dimensionless parameters included the Mach number M and the cooling parameter χ . The Mach numbers of the experimental jets were on the same order of magnitude that the astrophysical case ($M \sim 20$), and the cooling parameter was found to vary between 40 for the CH jet to 0.7 for the gold jet. This experiment clearly demonstrated that jets could be produced that

spanned a wide range of conditions, from nearly adiabatic to radiatively cooled expansion. An important conclusion was that the radiative cooling time is an important parameter for the formation of well collimated jets.

Other geometries have been used to create supersonic laboratory astrophysical jets from laser-created plasmas. Loupiau *et al.* (2007) generated high speed plasma jets using foam-filled cone targets at the LULI2000 laser facility in France [15]. The two kilojoule nanosecond beams of the laser facility were focused with an intensity of $\sim 10^{14}$ W/cm² on the back of the target to drive a strong shock through a two layer target. A first thin (20 μ m) layer of CH acted as an ablator/pusher to create the shock, with a 3 μ m thick Ti layer to prevent x-rays from preheating the foam. The shock then propagated through the foam to generate a dense hot plasma. The density of the foam could be varied. The conical shape of the target helped guide, confine and accelerate the plasma flow to produce a supersonic jet. X-ray radiography, interferometry and Self Optical Pyrometry (SOP) were used to infer the jet velocity, radial evolution and temperature. The dimensionless numbers calculated for this experiment showed that a scaling to Herbig-Haro objects was possible. While the Mach number was comparable, the experimental jets were adiabatically expanding ($\chi > 10^3$), and radiation did not play a very significant role in the evolution of those jets, contrary to other experiments.

Plasma jets were also created using colliding laser-created plasmas from thin foils [14] performed at the VULCAN facility. The plasmas were created irradiating the back side of two aluminum thin foils placed at 90 degree with respect to each other. The resulting plasma flow collided on axis, resulting in a collisional jet. The electron density of those plasmas were obtained using interferometry at $\lambda = 264$ nm. Jet velocity and extent were also measured from the experimental data. The dimensionless scaling parameters computed for this particular experiment suggested that the jets were in a regime where they could be relevant to Young Stellar Object (YSO) jets. However the authors noted that in order to improve the similarity between

experiments and YSO jets, the geometry of the experiment should be improved to match the cylindrical symmetry of astrophysical jets.

In 2006, Nicolai *et al.* demonstrated the formation and evolution of dense collimated radiative jets launched from flat targets [8]. Using the laser facility at PALS, the laser beam was focused onto the target in a spot of radius varying between 35 to 500 μm . The intensity used in this experiment was $\sim 10^{14}$ W/cm^2 and the flat targets were made out of aluminum, copper and silver. To study the expansion of the ablated plasma, a three-frame interferometry system using the third harmonic ($\lambda = 438\text{nm}$) of the irradiating beam was employed. Electron density distributions were recorded at three simultaneous times during the evolution of the plasma (2 ns, 5 ns and 8 ns). The plasma shape was found to vary as a function of spot radius: larger spot radii were found to create plasmas expanding further away from the target surface. It was also reported that increasing the atomic number of the target yielded tighter, more collimated, jets. Using a two-dimensional hydrodynamic code, electron density and temperature distributions were simulated. The simulation results matched the experimental case only when radiation was taken into account, once again confirming that radiation cooling plays an important role in shaping and collimating these plasma jets. The dimensionless parameters computed in this experiment yielded a high Mach number ($M > 10$), low cooling parameter and high Reynolds and Peclet number, in agreement with other radiative jets experiments and astrophysical objects.

1.6. Conclusions

There is a significant interest in studying plasmas. Basic knowledge about our universe can be gained by observing and understanding astrophysical plasmas such as supernova remnants, collimated jets from young stellar object, and stellar cores. In our daily life, plasmas are routinely

used around us, in devices such as lighting fluorescent tubes and plasma televisions. Hot dense plasmas are also of great interest to generate incoherent and coherent extreme ultraviolet and x-ray radiation, for both applications such as the lithography of the next generation of computer chips, as well as fundamental research and for achieving controlled thermonuclear fusion.

The production of dense plasmas in the laboratory also opened the road for high energy density laboratory astrophysics (HEDLA), where the study of plasma dynamics in the laboratory can provide insights to some astrophysical phenomena. In particular, there is an interest in studying dense plasma jets. Experiments showed that it was possible to create dense collimated radiative jets in the laboratory using laser, both high power laser facilities, and lower energy table-top lasers. The dynamics of those dense plasmas can be studied using a variety of tools, and in particular interferometry for measuring the evolution of the free electron density.

The experiments presented in this dissertation aim to study the evolution of dense plasmas created using a much smaller laser system (only a few optics tables long) to irradiate solid targets of various geometries using intensities of $\sim 10^{11}$ to 10^{13} W/cm². Laser interferometry at soft x-ray wavelength is the main diagnostic technique used to study these plasmas, as their high density-length product and high density gradients prevent any measurements using optical laser probes. The soft x-ray laser interferometry measurements were complemented by self-emission imaging and emission spectroscopy. The choice of the target shape was selected to create plasmas with different dynamics such as plasmas focus, bow shocks, highly collisional dense radiative or adiabatic jets. The interpretation of the experimental results was assisted using model simulations conducted with the hydrodynamic code HYDRA.

Chapter 2 explains in details soft x-ray interferometry, the main diagnostic technique used in the experiments performed in this dissertation. In Chapter 3, the complete experimental setup is presented. The last two chapters focus on the results obtained for three different target

geometries: dense plasma focus using half-cylindrical targets (Chapter 4), and dense plasma jets obtained using v-grooved and conical targets (Chapter 5).

1.7. References:

- [1] D. A. Gurnett, A. Bhattacharjee, *Introduction to Plasma Physics: With Space and Laboratory Applications*: Cambridge University Press, 2005.
- [2] J. Sollerman, P. Lundqvist, D. Lindler *et al.*, “Observations of the Crab Nebula and Its Pulsar in the Far-Ultraviolet and in the Optical,” *Astrophys. J.*, vol. 537, pp. 861-874, 2000.
- [3] D. J. McComas, S. J. Bame, P. Barker *et al.*, “Solar Wind Electron Proton Alpha Monitor (SWEPAM) for the Advanced Composition Explorer,” *Space Science Reviews*, vol. 86, no. 1, pp. 563-612, 1998.
- [4] F. F. Chen, *Introduction to Plasma Physics and Controlled Fusion*, 2nd edition ed.: Plenum Press, 1984.
- [5] D. R. Farley, K. G. Estabrook, S. G. Glendinning *et al.*, “Radiative jet experiments of astrophysical interest using intense lasers,” *Phys. Rev. Lett.*, vol. 83, no. 10, pp. 1982-1985, 1999.
- [6] K. Shigemori, R. Kodama, D. R. Farley *et al.*, “Experiments on radiative collapse in laser-produced plasmas relevant to astrophysical jets,” *Phys. Rev. E*, vol. 62, no. 6, pp. 8838-8841, 2000.
- [7] L.B. Da Silva, T.W. Barbee Jr., R. Cauble *et al.*, “Electron density measurements of high density plasmas using soft x-ray laser interferometry,” *Phys. Rev. Lett.*, vol. 74, no. 20, pp. 3991-3994, 1995.

- [8] P. Nicolai, V. T. Tikhonchuk, A. Kasperczuk *et al.*, “Plasma jets produced in a single laser beam interaction with a planar target,” *Phys. Plasmas*, vol. 13, no. 062701, 2006.
- [9] J. Grava, M. A. Purvis, J. Filevich *et al.*, “Dynamics of a dense laboratory plasma jet investigated using soft x-ray laser interferometry,” *Physical Review E*, vol. 78, no. Copyright (C) 2010 The American Physical Society, pp. 016403, 2008.
- [10] M. A. Purvis, J. Grava, J. Filevich *et al.*, “Collimation of dense plasma jets created by low-energy laser pulses and studied with soft x-ray laser interferometry,” *Phys. Rev. E*, vol. 81, no. 3, pp. 036408, 2010.
- [11] M. H. Key, and I. J. Spalding, “Interactions of intense laser radiation with plasma,” *Phil. Trans. R. Soc. Lond. A*, vol. 300, pp. 599-612, 1981.
- [12] A. Kasperczuk, T. Pisarczyk, S. Borodziuk *et al.*, “Stable dense plasma jets produced at laser power densities around 10^{14} W/cm²,” *Phys. Plasmas*, vol. 13, no. 062704, 2006.
- [13] J. Grava, M. A. Purvis, J. Filevich *et al.*, “Dynamics of a dense laboratory plasma jet investigated using soft x-ray laser interferometry,” *Physical Review E (Statistical, Nonlinear, and Soft Matter Physics)*, vol. 78, no. 1, pp. 016403, 2008.
- [14] C. D. Gregory, J. Howe, B. Loupiau *et al.*, “Astrophysical jet experiments with colliding laser-produced plasmas,” *Astrophys. J.*, vol. 676, pp. 420-426, 2008.
- [15] B. Loupiau, M. Koenig, E. Falize *et al.*, “Supersonic-Jet Experiments Using a High-Energy Laser,” *Physical Review Letters*, vol. 99, no. 26, pp. 265001, 2007.
- [16] S. S. Harilal, B. O'Shay, M. S. Tillack *et al.*, “Spectroscopic characterization of laser-induced tin plasma,” *J. Appl. Phys.*, vol. 98, no. 013306, 2005.
- [17] T. Atwee, and H. J. Kunze, “Spectroscopic investigation of two equal colliding plasma plumes of boron nitride,” *J. Phys. D: Appl. Phys.*, vol. 35, pp. 524-528, 2002.
- [18] I. H. Hutchinson, *Principles of Plasma Diagnostics*, p. 105, 2002.

- [19] R. S. Craxton, F. S. Turner, R. Hoefen *et al.*, “Characterization of laser-produced plasma density profiles using grid image refractometry,” *Phys. Fluids B*, vol. 5, no. 12, pp. 4419-4431, 1993.
- [20] K. Takahashi, R. Kodama, K.A. Tanaka *et al.*, “Laser-hole boring into overdense plasmas measured with soft x-ray laser probing,” *Phys. Rev. Lett.*, vol. 84, no. 11, pp. 2405-2408, 2000.
- [21] E. Hecht, *Optics (third edition)*: Addison-Wesley, 1998.
- [22] Heinrich F. Beyer, Viacheslav Petrovich Shevel'ko, “Introduction to the physics of highly charged ions,” pp. 35, 2003.
- [23] Paul J. Caber, “Interferometric profiler for rough surfaces,” *Applied Optics*, vol. 32, no. 19, pp. 3438-3441, 1993.
- [24] P. M. Celliers, G. W. Collins, L. B. Da Silva *et al.*, “Accurate measurement of laser-driven shock trajectories with velocity interferometry,” *Applied Physics Letters*, vol. 73, no. 10, pp. 1320-1322, 1998.
- [25] S. Yoshida, M. Muhamad, R. Widiastuti *et al.*, “Optical interferometric technique for deformation analysis,” *Opt. Express*, vol. 2, no. 13, pp. 516-530, 1998.
- [26] D. Hinshelwood, B. Weber, J. M. Grossmann *et al.*, “Density redistribution in a microsecond-conduction-time plasma opening switch,” *Physical Review Letters*, vol. 68, no. 24, pp. 3567, 1992.
- [27] B. V. Weber, D. D. Hinshelwood, “He-Ne interferometer for density measurements in plasma opening switch experiments,” *Rev. Sci. Instr.*, vol. 63, no. 10, pp. 5199, 1992.
- [28] F. Leipold, R. H. Stark, A. El-Habachi *et al.*, “Electron density measurements in an atmospheric pressure air plasma by means of infrared heterodyne interferometry,” *J. Phys. D: Appl. Phys.*, vol. 33, pp. 2268-2273, 2000.

- [29] P. Hartigan, J. Raymond, and L. Hartmann, "Radiative bow shock models of Herbig-Haro objects," *Journal Name: Astrophys. J.; (United States); Journal Volume: 316*, pp. Medium: X; Size: Pages: 323-348, 1987.
- [30] S.R. Goldman, S.E. Caldwell, M.D. Wilke *et al.*, "Shock structuring due to fabrication joints in targets," *Phys. Plasmas*, vol. 6, no. 8, pp. 3327-3336, 1999.
- [31] S.R. Goldman, C.W. Barnes, S.E. Caldwell *et al.*, "Production of enhanced pressure regions due to inhomogeneities in inertial confinement fusion targets," *Phys. Plasmas*, vol. 7, no. 5, pp. 2007-2013, 2000.
- [32] S. I. Braginskii, *Transport processes in a plasma*, 1965.
- [33] R. P. Drake, *High-Energy-Density Physics: Fundamentals, Inertial Fusion, and Experimental Astrophysics (Shock Wave and High Pressure Phenomena)*: Springer Press, 2006.
- [34] C. Yamanaka, S. Nakai, T. Yamanaka *et al.*, "High thermonuclear neutron yield by shock multiplexing implosion with Gekko-XII green laser," *Nucl. Fusion*, vol. 27, pp. 19-30, 1987.

Chapter 2. Soft x-ray laser interferometry of dense plasmas

This chapter describes soft x-ray laser interferometry, the main diagnostic technique used in the experiments presented in this dissertation. After introducing the technique, we will show that the limitations of conventional optical interferometry can be overcome by using laser sources of shorter wavelength. The detailed interferometer scheme used at Colorado State University is presented in Chapter 3.

2.1. Soft x-ray laser interferometry

Soft x-ray laser (SXRL) interferometry has been demonstrated as a powerful tool to probe a wide area of plasma parameter space [1-4]. While optical interferometry has been used for a long time, the earliest proof-of-principle experiments using soft x-ray laser interferometry of laser-created plasmas were conducted in the 1990's. The experiments used laboratory-size soft x-ray lasers with very low repetition rates (a few shots per day). In 1995, Da Silva *et al.* used soft x-ray laser interferometry combined with the NOVA laser to probe millimeter size laser-created dense plasmas with micron spatial resolution [4]. Later on, the interaction and dynamics of counter-streaming high density laser-created colliding plasmas were studied with the same setup by A.S. Wan *et al.* [5]. More recently, compact soft x-ray lasers [6-7] have been used in combination with improved interferometers to conduct studies in a variety of laser-created

plasmas [1-3, 8]. The advantages of using shorter wavelength for the probe laser are described in the next section.

2.1.1. Extending the limits of interferometry using SXRLs

The short wavelength of the soft x-ray lasers (SXRLs) available nowadays, 10 to 50 nm, presents several advantages for extending the limits of plasma interferometry. The shorter wavelength reduces refraction and absorption, and improves the spatial resolution of interferograms. Moreover, the high monochromaticity of SXRLs allows for the use of multilayer-coated optics as filters to discriminate the probe beam from the strong self-emission of the hot dense plasmas. Lastly, recent advances in laser engineering enabled the creation of table-top soft x-ray lasers with spectral purity and brightness that equals or exceeds their laboratory size predecessors, at much higher repetition rates [6, 9-12]. All the advantages of SXRLs make them excellent sources for probing hot denser plasmas with millimeter scale lengths.

The aforementioned advantages of reducing the wavelength of the probe beam can be seen simply by looking at the mathematical expressions for absorption and refraction of the plasma. The free-free absorption coefficient in plasma is given by:

$$\alpha \approx 2.44 \times 10^{-37} \frac{\langle Z^2 \rangle n_e n_i}{\sqrt{kT} (h\nu)^3} \left[1 - \exp\left(\frac{-h\nu}{kT}\right) \right]$$

where $\langle Z \rangle$ is the mean ion charge, n_e is the electron density, n_i is the ion density, and kT the electron temperature [13]. The absorption is proportional to the square of the wavelength. Thus, a reduction by an order of magnitude in wavelength reduces the absorption coefficient by two orders of magnitude. The number of fringe shift N_{fringe} that can be resolved is usually limited by the resolution of the detection system, and decreases as $1/\lambda$, showing yet another advantage of

using shorter wavelengths. However, in practice the main factor limiting the plasma densities and sizes that can be probed is often refraction. In the presence of strong density gradients, the probe beam can only travel a certain distance inside the plasma before being refracted off. This distance is called the refraction length $L_r = \frac{d}{2} \sqrt{n_c/n_e}$ [14], where d is the plasma diameter, as illustrated in Figure 2.2a.

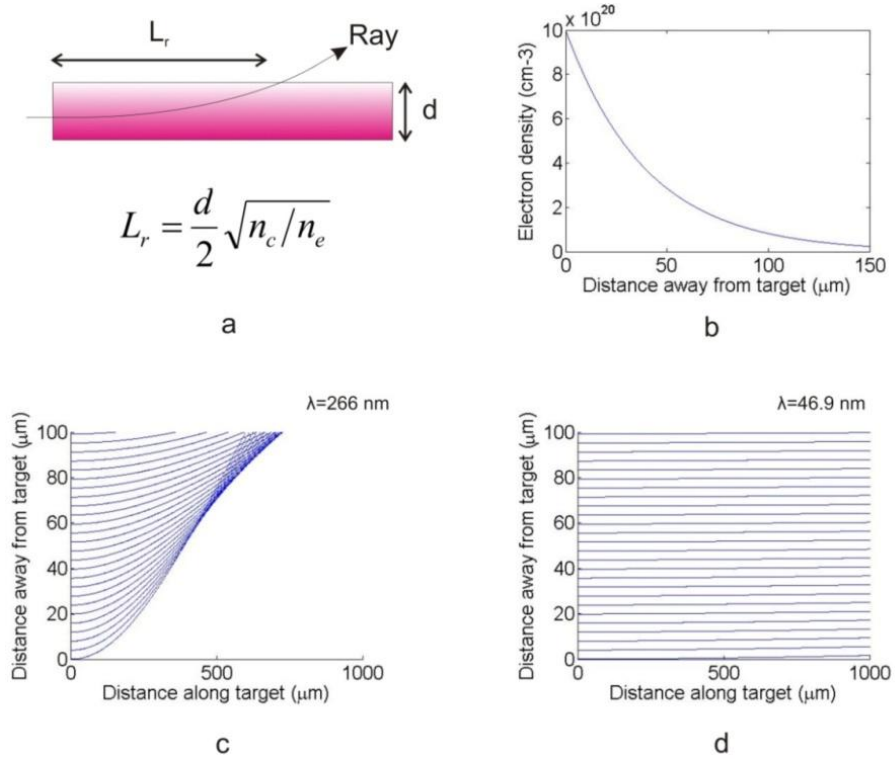


Figure 2.1. Ray refraction inside a plasma. Figure (a) shows the relationship between the refraction length and the index of refraction of the plasma. Computation of rays traveling inside a 1mm long plasma are shown for 266 nm (4th harmonic of YAG laser, c) and 46.9 nm (soft x-ray laser, d) probes with the electron density profile shown in (b). The shorter wavelength is significantly less refracted, allowing probing closer to the target.

The refraction length increases for higher plasma critical density. Since the critical density increases with a decrease in the wavelength of the probe beam (n_c proportional to $1/\lambda^2$),

the refraction length scales as the inverse of the probe beam wavelength. This is illustrated in Figure 2.2c, where ray traces have been computed for two probe beam wavelength traveling along a 1 mm long plasma with a maximum electron density of $\sim 10^{21} \text{ cm}^{-3}$ close to the target and an exponentially decreasing profile away from the target. In the case of $\lambda = 266 \text{ nm}$ light (4th harmonic of an Nd: YAG laser with a critical density $n_c \sim 10^{21} \text{ cm}^{-3}$, Figure 2.3.c), the rays travel only about 500 μm before they are completely refracted outside of the plasma. However, when shorter wavelength ($\lambda = 46.9 \text{ nm}$), in the soft x-ray range with $n_c \sim 5 \times 10^{23} \text{ cm}^{-3}$, Figure 2.2.d) is used the refraction of the rays can be neglected. Figure 2.3 summarizes how reducing the wavelength can increase the parameter space (electron density vs. plasma length) accessible for plasma probing, as determined by both the probe beam absorption and refraction. Three laser probe wavelength are considered: 4th YAG harmonic (266 nm), Ne-like Ar (46.9 nm) and Ni-like Pd (14.6 nm). The plasma temperature is assumed to be 100 eV. As the wavelength is reduced, denser and longer plasmas can be probed, as the effects of absorption and refraction is greatly reduced.

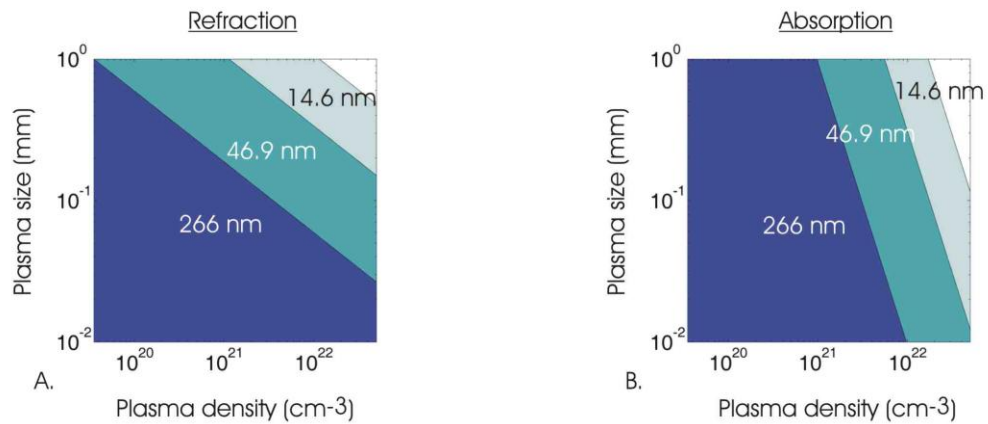


Figure 2.2. Maximum plasma size probed for different laser probe wavelength as a function of the electron density. The plasma temperature is 100 eV. The effect of wavelength reduction on refraction (a) and absorption (b) is illustrated. In both cases, shorter wavelengths enable the probing of plasmas with larger density and longer size.

Soft x-ray interferometry has been demonstrated as a powerful tool for probing dense laser-created plasmas [1-2, 4, 15-19]. Numerous experiments used a variety of interferometer configurations in combination with various soft x-ray laser sources. The next section discusses the soft x-ray interferometer configurations, along with the diffraction grating interferometer (DGI) used in the experiments presented herein.

2.2. Soft x-ray interferometers

As discussed in Chapter 1, in order to produce a high contrast fringe pattern, the output of two coherent sources must interfere. However two separate sources with the exact same coherence are difficult to find in nature. This problem was first solved by Thomas Young in his classic double-slit experiment [20], where he took a single wavefront, split it in two waves and had them interfere. Two coherent waves can be generated from a single source by dividing the wavefront of the emitted light or its amplitude. The first method is called wavefront-division interferometry and needs a source with very good degree of spatial coherence since two different region of the same wave must interfere to produce fringes. The latter, called amplitude-division interferometry, based on the amplitude of the wave, can produce good interference even if the source does not have a high spatial coherence. However, in both cases, good temporal coherence is required. Several interferometer schemes are discussed next, with their advantages and adaptation for use at soft x-ray wavelength.

2.2.1. Lloyd's mirror soft x-ray laser interferometer

The Lloyd's mirror interferometer is the simplest wavefront division interferometer, as it only requires a single mirror (see Figure 2.4). When using a gold coated mirror at grazing incidence, it is particularly well suited for soft x-ray wavelength sources [8].

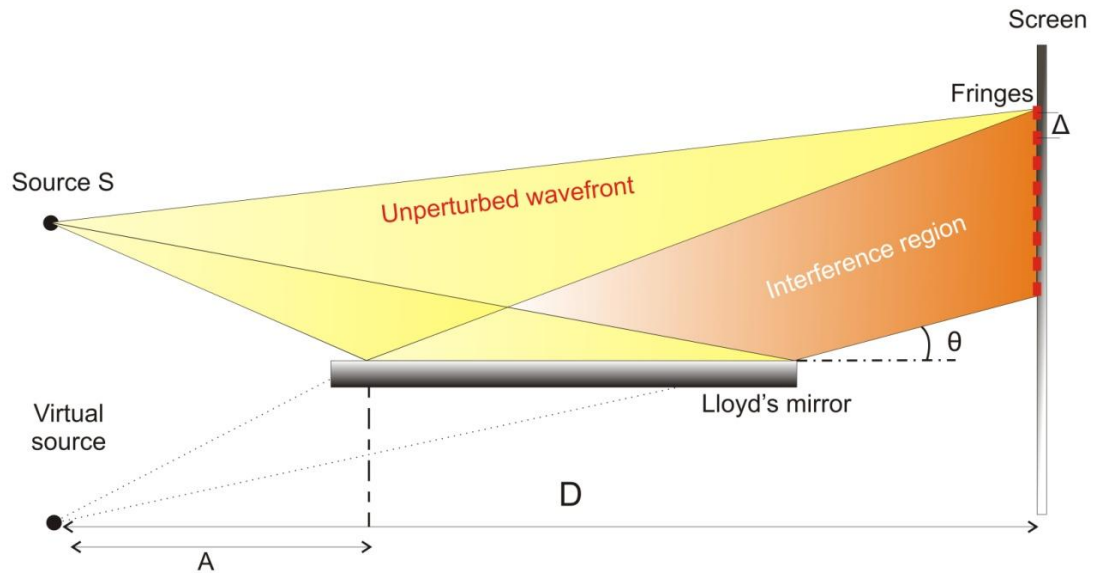


Figure 2.3. Schematics of a Lloyd's mirror soft x-ray interferometer [8]. The source S and virtual source S' are separated by a distance A. Calling the source to screen distance D, the separation between fringes is given by $\Delta = \frac{D\lambda}{2A\theta}$.

In this setup, part of the original wavefront is split by the mirror while the other portion directly travels towards the detector plane, where both wavefronts are recombined and interferences are observed. While this interferometer has the advantage of simplicity, the paths traveled by both wavefront do not have the same length, and if the path difference is larger than the coherence length of the source, no fringes will be seen at the detection plane.

2.2.2. Fresnel bi-mirror configuration

Another useful wavefront-division interferometer is the Fresnel double mirror configuration [2]. It consists of two plane mirrors inclined to each other at a small angle θ , as shown in Figure 2.4. A portion of the wavefront coming from the source S is reflected from the first mirror, and another portion of the wavefront is reflected from the second mirror. Those two reflected waves interact and generate the interference pattern visible on the screen. The two equivalent virtual sources $S1$ and $S2$ can be considered as two independent coherent sources located from the center of the two mirrors at a distance A . The fringe separation in this case is $\Delta = \frac{(D+A)\lambda}{2A\theta}$, with D the distance between the center of the mirror and the screen, again in the small angle approximation. Notice that in this configuration, both interfering waves are reflected off a mirror, while in the case of the Lloyd's mirror, only one part of the beam was reflected, introducing a 180 degree phase shift in this case. Because of this phase shift, an intensity maximum in the case of the Lloyd's mirror configuration corresponds to an intensity minimum in the Fresnel configuration. Also, in the Fresnel double mirror configuration both reflected waves travel the same distance before interfering, and thus interferences can be obtained using sources with lower temporal coherence (such as a discharge lamp for instance). The angle θ between the two mirrors can be changed to modify the separation of the fringes: as θ decreases the fringes broaden.

Notice that both the Fresnel bi-mirror configuration can be used with any type of source that meets the coherence requirements, in particular with laser light. However in the case of a soft x-ray source, grazing incidence reflection must be used in order to avoid excessive intensity losses on the optics.

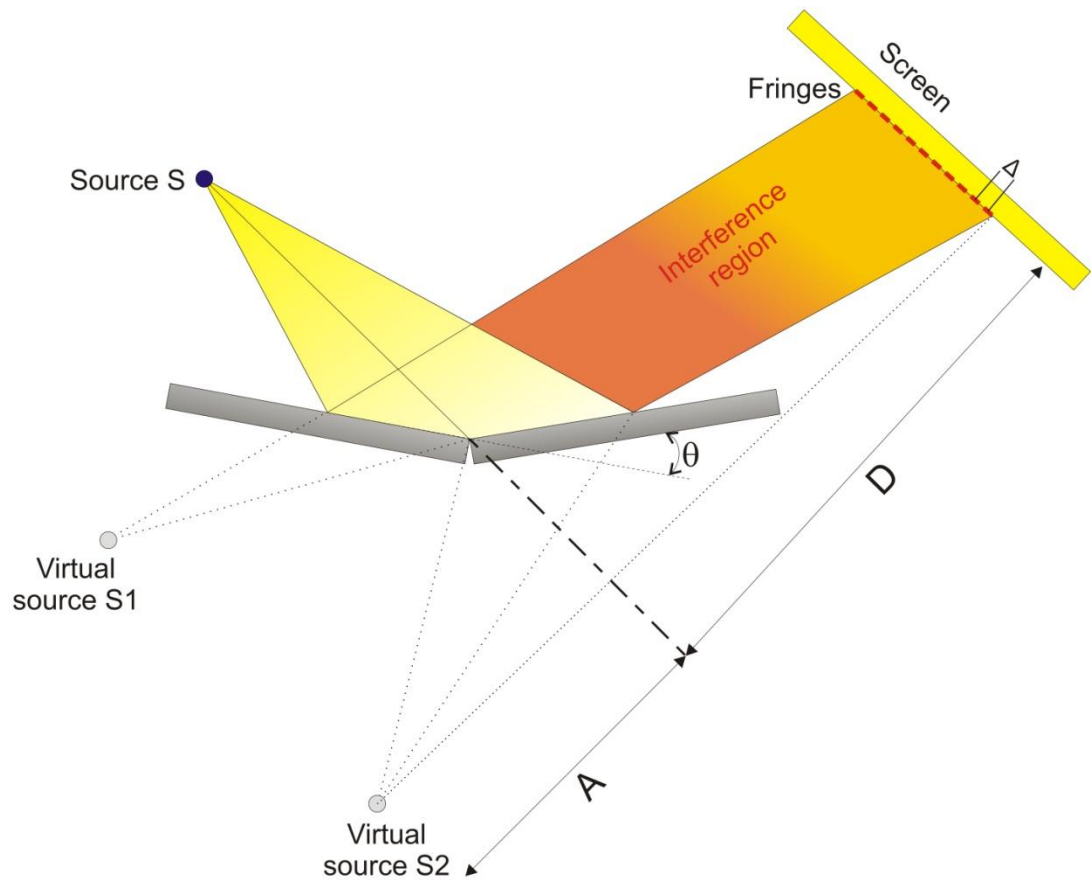


Figure 2.4. Diagram of a Fresnel bi-mirror interferogram [2]. The shield prevents light from the source to directly impinge on the screen. The small angle θ can be modified to change the spacing of the fringes observed at the screen.

In 2004, a collaboration between the French group from Université Paris-Sud and the Japanese group at the Japan Atomic Energy Research Center (JAERI) presented results on Aluminum plasma diagnostics realized with soft x-ray interferometry [3]. The probe beam, a transient Nickel-like Silver x-ray laser operating at 13.9 nm (several picoseconds pulse duration [6]), was combined with the wavefront-division imaging Fresnel bi-mirror interferometer illustrated in Figure 2.4. Interferograms of the Al plasma probed between 0 and 5 ns after the

peak of the heating pulse (a 1.2 ns IR laser) were obtained and fringe shifts were clearly observed as a consequence of the plasma evolution.

2.2.3. Mach Zehnder soft x-ray laser interferometer

In amplitude-division interferometers, the initial wavefront is split in two wavefronts of similar intensity by mean of an optical device (for example, a thin film beam splitter or a diffraction grating). They are subsequently recombined at the output of the interferometer, where interferences will be observed as long as the original coherence between the two waves is retained. In other words, if the path length difference between the two waves is greater than the coherence length of the original wave (related to its temporal coherence), then no interference pattern would be observed when the waves are recombined. Thus in amplitude-division interferometers, the two paths (also called arms) of the interferometer must have nearly the same length (i.e. within a coherence length L_c). The Mach-Zehnder interferometer, schematically illustrated in Figure 2.5, is an amplitude-division interferometer that uses a robust setup capable of producing fringes with excellent contrast and high visibility. Since the two paths are separated, the interferometer is relatively difficult to align but is highly stable.

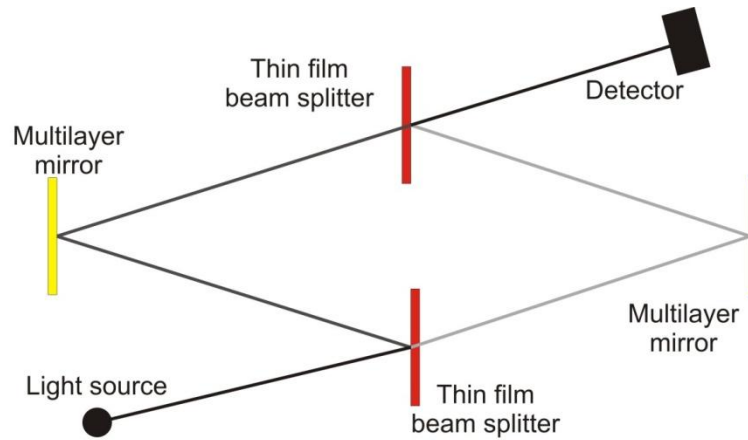


Figure 2.5. Diagram of the Mach-Zehnder soft x-ray interferometer [4]. The paths of both arms are of nearly equal length (within the coherence length of the source), condition required to observe an interference pattern on the detector when recombining the two waves. In the version presented here, thin film beam splitters are used for the short wavelength laser source.

In 1995, Da Silva *et. al* [4] have used for the first time this soft x-ray interferometer configuration to probe large laser-created plasmas with micron spatial resolution. The probe beam, a Neon-like Yttrium laser operating at 15.5 nm (~200 ps pulse duration), was combined with a laboratory size Mach-Zehnder interferometer using multi-layer coated beam splitters to obtain electron density profiles of dense laser-produced plasmas, as shown in Figure 2.5. The plasmas were created irradiating a CH target with the fusion class NOVA laser at an intensity of $2.7 \times 10^{13} \text{ Wcm}^{-2}$. Fringes were resolved as close as 0.025 mm from the target surface and the measured electron density profile was compared to a 1-D magneto hydrodynamic simulation. The simulation results predicted higher electron densities than measured, the error increasing with the distance from the target. This discrepancy was attributed to the fact that the plasma was also expanding laterally, leading to significantly lower electron densities in the experiment. Nevertheless, this work proved that the development of soft x-ray interferometer could play an

important role in probing dense plasmas, providing extensive data to correct the deficiencies of numerical models. However, a drawback of this setup is the use of thin film beam splitters that are easily damaged by the plasma, and have to be replaced after every shot.

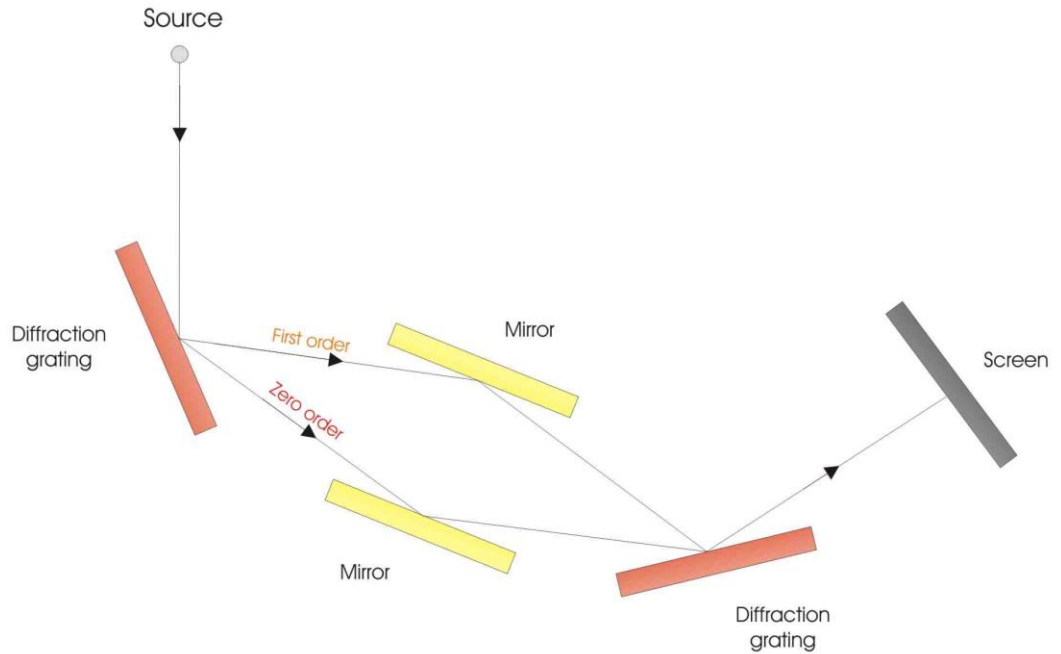


Figure 2.6. Schematic drawing of a Mach Zehnder diffraction grating interferometer (DGI). This interferometer is specifically design to operate at short wavelength (50-10 nm), and can be scaled by changing the ruling and blaze angle of the gratings.

Another implementation of the Mach Zehnder interferometer for specific use at soft x-ray wavelength is to use diffraction gratings as beam splitters [17] (Figure 2.6). The ruling and blaze angle can be tailored to have similar intensities on two different orders, and the use of grazing incidence increases the reflectivity at soft x-ray wavelengths. The specific design of the diffraction grating interferometer used in the experiments presented in this dissertation is discussed in-depth in the next chapter.

2.3. References

- [1] C.H. Moreno, M.C. Marconi, K. Kanizay *et al.*, “Soft x-ray laser interferometry of a pinch discharge using a tabletop laser,” *Phys. Rev. E*, vol. 60, no. 1, pp. 911-917, 1999.
- [2] F. Albert, D. Joyeux, P. Jaegle *et al.*, “Interferograms obtained with a X-ray laser by means of a wavefront division interferometer,” *Optics Com.*, vol. 142, pp. 184-188, 1997.
- [3] H. Tang, O. Guilbaud, G. Jamelot *et al.*, “Diagnostics of laser-induced plasma with soft X-ray (13.9 nm) bi-mirror interference microscopy,” *Appl. Phys. B*, vol. 78, pp. 975-977, 2004.
- [4] L.B. Da Silva, T.W. Barbee Jr., R. Cauble *et al.*, “Electron density measurements of high density plasmas using soft x-ray laser interferometry,” *Phys. Rev. Lett.*, vol. 74, no. 20, pp. 3991-3994, 1995.
- [5] A.S. Wan, J. T.W. Barbee, R. Cauble *et al.*, “Electron density measurement of a colliding plasma using soft x-ray interferometry,” *Phys. Rev. E*, vol. 55, no. 5, pp. 6293-6296, 1997.
- [6] T. Kawachi, M. Kado, M. Tanaka *et al.*, “Gain saturation of nickel-like silver and tin x-ray lasers by use of a tabletop pumping laser system,” *Physical Review A*, vol. 66, no. 3, pp. 033815, 2002.
- [7] J. J. Rocca, “Table-top soft x-ray lasers,” *Rev. Sci. Instrum.*, vol. 70, pp. 3799, 1999.
- [8] J.J. Rocca, C.H. Moreno, M.C. Marconi *et al.*, “Soft x-ray laser interferometry of a plasma with a tabletop laser and a Lloyd's mirror,” *Optics Lett.*, vol. 24, no. 6, pp. 420-422, 1999.

- [9] J. Dunn, A. L. Osterheld, J. Nilsen *et al.*, “Saturated output tabletop x-ray lasers,” *7th international conference on X-ray lasers, Saint-Malo, France, 2000*.
- [10] J.J. Rocca, D.P. Clark, J. A. Chilla. *et al.*, “Energy extraction and achievement of the saturation limit in a discharge-pumped table-top soft x-ray amplifier,” *Phys. Rev. Lett.*, vol. 77, no. 8, pp. 1476-1479, 1996.
- [11] B. M. Luther, Y. Wang, M. A. Larotonda *et al.*, “Saturated high-repetition-rate 18.9-nm tabletop laser in nickel-molybdenum,” *Opt. Lett.*, vol. 30, no. 2, pp. 165-167, 2005.
- [12] M. Grisham, S. Heinbuch, D. Martz *et al.*, “Demonstration of a desk-top size high repetition rate soft x-ray laser,” *Opt. Express*, vol. 11, no. 13, pp. 4050-4055, 1998.
- [13] D. T. Attwood, *Soft x-rays and extreme ultraviolet radiation: principles and applications*: Cambridge University Press, 2000.
- [14] R. A. London, “Beam optics of exploding foil plasma x-ray lasers,” *Phys. Fluids*, vol. 31, no. 1, pp. 184, 1988.
- [15] D. Joyeux, R. Mercier, D. Phalippou. *et al.*, “An Interferometric microimaging system for probing laser plasmas with an x-ray laser,” *SPIE Proceedings*, 2000.
- [16] F. Polack, D. Joyeux, J. Svatos *et al.*, “Applications of wavefront division interferometers in soft x rays,” *Rev. Sci. Instrum.*, vol. 66, no. 2, pp. 2180-2183, 1995.
- [17] J. Filevich, K. Kanizay, M. C. Marconi *et al.*, “Dense plasma diagnostics with an amplitude-division soft x-ray interferometer based on diffraction gratings,” *Optics Lett.*, vol. 25, no. 5, pp. 356-358, 2000.
- [18] J. Filevich, J. J. Rocca, E. Jankowska *et al.*, “Two-dimensional effects in laser-created plasmas measured with soft x-ray laser interferometry,” *Phys. Rev. E*, vol. 67, no. 056409, 2003.
- [19] R.F. Smith, J. Dunn, J. Nilsen *et al.*, “Picosecond x-ray laser interferometry of dense plasmas,” *Phys. Rev. Lett.*, vol. 89, no. 6, pp. 065004(4), 2002.

[20] E. Hecht, *Optics (third edition)*: Addison-Wesley, 1998.

Chapter 3. Experimental Setup

3.1. Introduction

This chapter describes the experimental setup used in the soft x-ray laser interferometry experiments discussed in this dissertation. Figure 3.1 schematically shows the complete soft x-ray laser interferometry setup. The main diagnostic used to probe the laser-created dense plasmas is a table-top capillary discharge soft x-ray (46.9 nm) laser combined with a robust diffraction grating interferometer. The plasmas are created irradiating solid targets of various shapes with a high energy (up to 1 J) short duration (120-220 ps) 800 nm Titanium Sapphire laser. Each element of this setup is individually presented next, along with the different target shapes used in the various experiments and the data analysis techniques employed to obtain two dimensional electron density maps of the plasma from the interferograms.

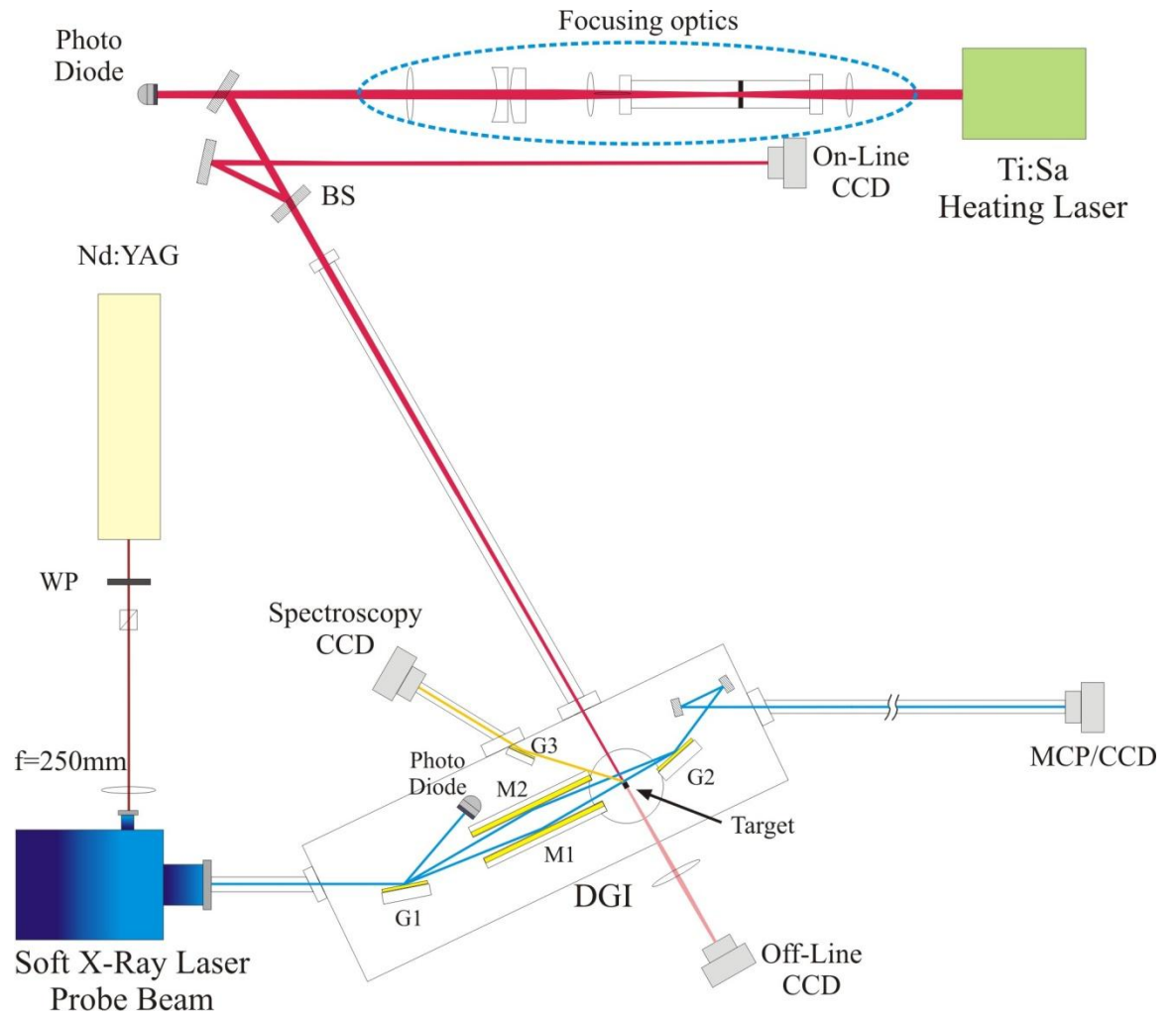


Figure 3.1. Schematic diagram of the experimental setup showing the soft x-ray laser interferometer, the 46.9 nm wavelength probe generated by a laser-triggered capillary discharge laser (SXRL), and the target irradiation beam produced by a chirped-pulse amplification Ti: Sapphire laser. This beam is shaped with lenses to obtain a spot or line focus. BS is a beam splitter (~4% reflection) redirecting part of the beam to a monitoring CCD. The inserts show CCD camera images of the line focus beam used to irradiate the target, and the interferogram resulting of probing the plasma. The timing between the probe pulse and heating pulse is determined using two photodiodes (PD). A time integrated spectroscopy measurement from the plasma self-emission was recorded onto the spectroscopy CCD after being diffracted off grating G3.

3.2. Main diagnostic: Soft x-ray laser interferometry

The laser-created plasmas presented in this dissertation were studied using a combination of a soft x-ray capillary discharge laser operating at a wavelength of 46.9 nm with a robust high throughput diffraction grating interferometer. These elements are presented next.

3.2.1. Diffraction Grating Interferometer (DGI)

The interferometer used at Colorado State University is a robust amplitude division interferometer implemented by using diffraction gratings as beam splitters [1]. As shown in Figure 3.2, this DGI interferometer uses two blazed gratings and two elongated grazing incidence mirrors in a skewed Mach-Zehnder configuration. The zero and first diffracted orders off the first grating (G_1) are used as the two arms of the interferometer. In order to obtain good fringe visibility, the gratings were ruled at a blaze angle of 1.33 degrees. This allows the generation of zero and first order beams of the same intensity when positioned at an angle of 79 degrees. Each beam is subsequently intercepted by an elongated grazing incidence mirror (M_1 or M_2) that directs it towards a second grating G_2 , where both beams are recombined to produce the interference pattern. After the second grating, a combination of a $f = 30$ cm spherical imaging mirror and a flat relay mirror is used to image the plane of the plasma target with $25\times$ magnification onto a detection system (see 3.1.3) placed ~ 7 m away. Both the elongated mirrors and the diffraction gratings are gold coated for enhanced reflectivity. The spacing and orientation of the generated fringes can be modified by changing the angles of the long mirrors and the tilt of the second grating. In the presented experiments, vertical fringes parallel to the front surface of

the target are preferred, since the plasmas are expected to evolve mostly perpendicular to the vertical target surface.

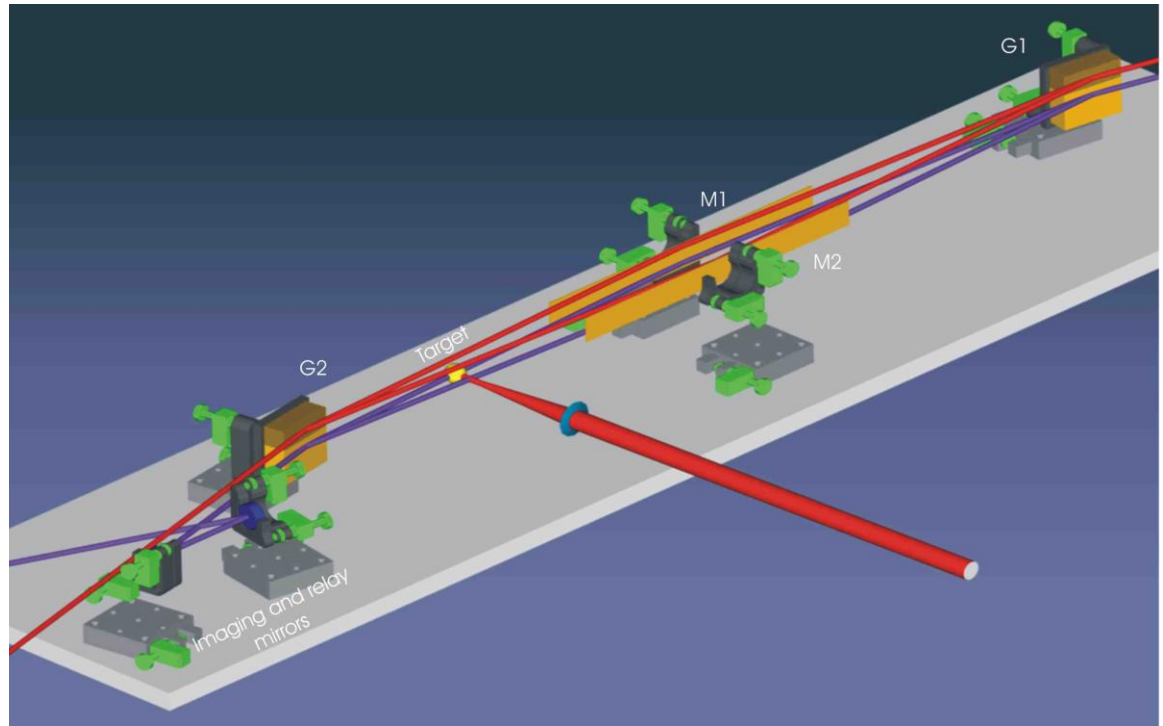


Figure 3.2. Diagram of the diffraction grating interferometer (DGI). The diffraction gratings (G1 and G2), the elongated gold-coated mirrors (M1 and M2), and the target are also shown. A set of imaging and relay mirrors is used to image the target plane onto a MCP/CCD system with a 25x magnification. The red and blue beams correspond respectively to the IR alignment laser and soft x-ray laser path. The red beam perpendicular to the target represents the Ti: Sapphire laser.

The plasmas to be studied were produced on the path of the 0th order beam, between the long mirror M1 and the second grating G2. Both relay and imaging mirrors were coated with Si-Sc multilayer, yielding to a normal incidence reflectivity of $\sim 40\%$ [2]. The multilayer coatings also help to separate the soft x-ray laser from part of the light emitted by the plasma. A set of

pinholes was placed between the target and the second grating in order to further reduce the strong light emitted from the laser-created plasma. This interferometer has the advantages of high throughput ($\sim 6\%$ per arm, excluding losses due to the imaging and relay mirrors) and significant robustness against plasma debris. This interferometer also showed good stability against vibrations of the optical components.

This interferometer was designed specifically for operation at the 46.9 nm wavelength of the Ne-like Ar capillary discharge soft x-ray laser [3]. Therefore, alignment of the interferometer at this wavelength must be done under vacuum, which is very challenging. In order to simplify the alignment process, the interferometer was designed such that an IR and a visible laser could be used to pre-align it. The first step of the alignment, conducted at atmospheric pressure, consists in directing the beam of the visible laser operating at $\lambda = 640$ nm along the input path of the soft x-ray laser. This visible laser beam is then used to align the zero order path of the interferometer, through the imaging and relay mirrors, and onto the detector. The alignment of the first order arm is done using an infrared semi-conductor laser (SDL-5401-G1) operating at $\lambda = 824$ nm, that has a temporal coherence length similar to the soft x-ray laser (~ 250 μm). In order for the IR laser to propagate along the same first order path as the soft x-ray laser, the gratings were ruled with two sets of vertically spaced rulings, where the ratio of the line densities is equal to the ratio of the wavelengths of the soft x-ray laser (46.9 nm) and infrared laser (824 nm). The corresponding line spacing is then 300 lines/mm for the soft x-ray laser and 16 lines/mm for the IR beam. This makes possible to use the infrared beam to equalize the path length of both arms of the interferometer and obtain interference fringes at atmospheric pressure. Subsequently, only minor adjustments are needed under vacuum to optimize the fringe contrast with the soft x-ray laser. All the relevant motions of the optics were motorized to allow for the optimization of the interferometer under vacuum.

3.2.2. Probe beam: capillary discharge soft x-ray laser

In 1994, Rocca *et al.* used a fast capillary discharge in Argon to demonstrate the generation of laser pulses at 46.9 nm. The device was the size of an optical table [4]. Gain saturation in this tabletop soft x-ray laser was achieved in 1996 [5-6]. Subsequent work resulted in the generation of a high average output power (~ 1 mW) and small divergence beam (~ 4.5 mrad) as well as a high degree of spatial coherence [7]. This very compact high repetition rate source (up to 10 Hz) opened the door to a wide variety of new applications. In particular, it constitutes an excellent source for soft x-ray interferometry.

The 46.9 nm capillary discharge soft x-ray laser used in the interferometry experiments can be seen on Figure 3.3. In this laser, amplification is obtained by excitation of an argon filled capillary channel with a fast discharge current pulse. The magnetic force generated by the fast current pulse rapidly compresses the Ar gas to form a dense and hot plasma column with a high concentration of neon-like ions. The plasma column has a very good axial uniformity and a length to diameter ratio higher than 1000:1. Collisional electron impact excitation from the ground state to the $3p^1p_0$ of the Ne-like ions produces a population inversion between the 3p and 3s levels, that results in the amplification of a single line at 46.9 nm [4]. The argon plasma column is created in a 3 mm diameter aluminum oxide capillary filled with Argon at a pressure of 460 mTorr. The excitation is provided by a fast current pulse of ~ 25 kA peak amplitude and 25 ns rise time. The current pulse is produced by discharging a water capacitor through a pressured spark gap switch that is connected in series with the capillary load. Deionized water serves as liquid dielectric for the capacitor which is pulse-charged in about 1 μ s by a Marx generator. The water is circulated to cool the capillary when operating at high repetition rates. Before excitation with this fast current pulse, a pre-ionizing current pulse of ~ 1.2 μ s duration and ~ 80 A is used to create a plasma in the

capillary channel. The use of this pre-pulse, creating an initial plasma column with very high uniformity, contributes to reduce the instabilities that deteriorates the symmetry of high current discharges [8]. The plasma column resulting from the rapid compression caused by the 25 kA current pulse is 200-300 μm in diameter. Lasing occurs when the electron temperature reaches 60-80 eV, and the electron density is rapidly rising [6]. The electron density peaks a few ns later at a value of about $1 \times 10^{19} \text{ cm}^{-3}$. The very good axial uniformity of these plasma columns is corroborated by the very good spatial coherence of the resulting beam [9].

The laser output energy and pulse duration depend on the plasma column length, determined by the capillary length. The saturation intensity is reached for capillaries of ~ 14 cm in length, when the beam intensity reaches 56 - 78 MW/cm^2 . For longer capillaries, the intensity of the plasma column increases linearly. In the particular case of the experiment described in this thesis, a 27.3 cm long aluminum oxide capillary with a 3.2 mm diameter was used at an Ar gas pressure of 465 mTorr. The resulting laser pulses are of about 0.15 mJ energy and ~ 1.2 ns (FWHM) in duration. The far field divergence of this beam was measured to be ~ 4.5 mrad [9]. Measurements corresponding to capillaries of about 36 cm in length demonstrated close to full spatial coherence, and a peak spectral brightness of $\sim 2 \times 10^{25}$ photons/(s $\text{mm}^2 \text{ mrad}^2$ 0.01 % B.W.) [9]. This makes this table-top laser a very bright soft x-ray source. Combined with its high monochromaticity and very good degree of spatial coherence, this source allows the generation of high contrast interferograms. Table 3.1 summarizes the most relevant parameters of this soft x-ray laser.

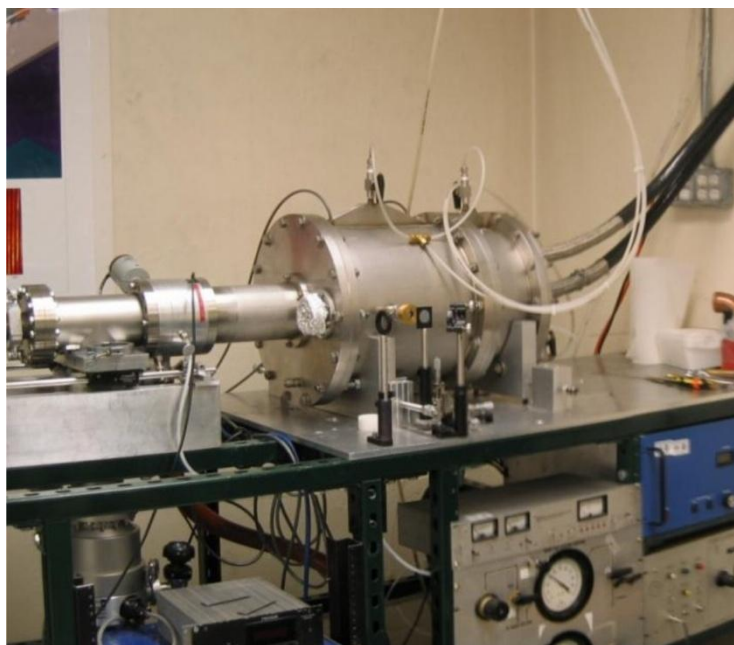


Figure 3.3. Picture of the tabletop Ne-like Ar 46.9 nm capillary discharge soft x-ray laser.

Wavelength	Pulse Energy	Peak Power	Pulse Duration	Beam Divergence	Spectral Brightness
46.9 nm	~ 0.2 mJ	~ 0.15 mW	~ 1.2 ns	~ 4.5 mrad	5×10^{24} ph/(mm ² mrad ² s 10 ⁻⁴ BW)

Table 3.1. Capillary discharge soft x-ray laser parameters.

The jitter (shot to shot time variation) of the laser pulse is important for the experiment described herein. Previous experiments with this laser source in other applications did not require ns jitter either because the experiment was performed in a time integrated regime, or because the evolution of the phenomena being studied was long enough for a large jitter to be acceptable. However, in experiments described herein where the duration of the process to be studied is relatively short (tens of ns or less), improving the probing laser jitter becomes critical.

A good control over the probe beam results in fewer shots needed to map the complete evolution of the plasmas of interest, or focusing on taking shots at critical moments. The most important source of jitter was the untriggered SXRL spark gap switch. The typical jitter of this system was typically 15 to 20 ns, resulting in a poor control over the soft x-ray laser firing time. Selecting a precise timeframe to probe the plasma evolution is difficult with such high jitter, especially since this jitter value is of the order of the characteristic time scale of the plasmas to probe. Therefore, laser triggering of the laser spark gap switch has been implemented to reduce its jitter. Laser triggered schemes have been demonstrated to be capable to achieve reproducible low jitter [10]. The soft x-ray laser spark gap was modified to allow triggering with a commercial 1064 nm Nd:YAG laser, as illustrated in Figure 3.4.

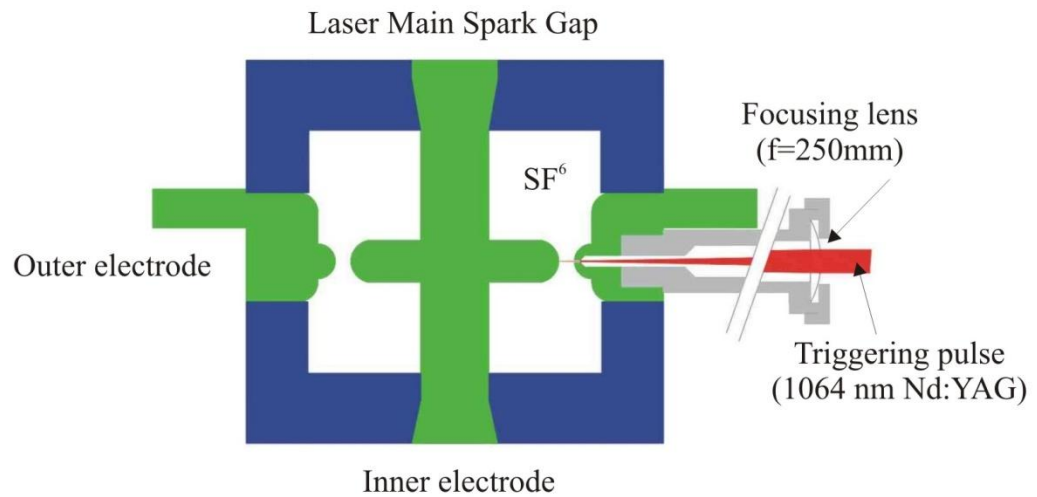


Figure 3.4. Modified soft x-ray laser main spark gap. A hole was drilled in the outer electrode to allow for the Nd:YAG pulse to focus onto the inner electrode, creating a small plasma that initiates breakdown of the spark gap switch with high precision. The inherent jitter (shot-to-shot variation) of the system was reduced from 15-20 ns down to 2 ns.

The pressurized spark gap consists of two concentric brass electrodes. The electrodes are separated by a 5 mm gap. A hole drilled in the outer electrode allows the triggering pulse to go through it and impinges on the inner electrode. This Nd:YAG laser pulse (~ 30 mJ energy and 5 ns duration) is focused at normal incidence onto the inner electrode of the spark gap by an $f = 250$ mm lens, creating a small plasma. The triggering laser pulse is timed to arrive when the voltage build up across the spark gap is about 90% of the self-breakdown voltage. The electrons from this plasma are rapidly accelerated towards the opposite electrode by the applied electric field. These electrons and the high energy photons generated by the plasma produce ionization that causes the spark gap to break down. The ability to consistently create plasma inside this spark gap by laser triggering allows controlling the soft x-ray laser firing time with typical standard deviation of about 2 ns (Figure 3.5). This jitter is smaller than the time scale of the plasmas to be probed. Careful alignment and optimization of the laser triggering pulse allow for sub-nanosecond jitter, but daily operations generally give this larger but still acceptable value for the jitter.

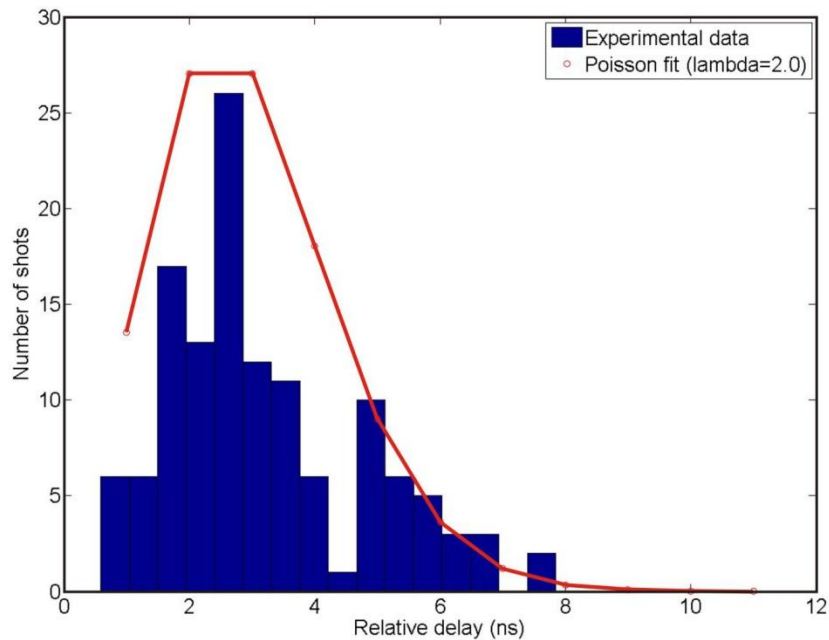


Figure 3.5. Histogram of 128 consecutive laser-triggered SXRL shots. The data taken are shown with a Poisson fit with $\lambda=2.0$ (in red). The calculated standard deviation (i.e. the jitter) in the case of this distribution is $\sqrt{\lambda}=1.4$ ns.

3.2.3. Detection system

The detection system consists of a micro channel plate (MCP), a phosphorous screen, an image intensifier and a charge coupled device (CCD). This setup is placed ~ 7 m away from the output of the interferometer, yielding a $25\times$ magnification of the target plane with the use of the spherical mirror used for imaging. The soft x-ray light coming from the output of the interferometer first impinges onto a micro channel plate. Photons entering the channels will generate electrons by secondary emission, effectively increasing the output signal. The resulting electrons then encounter the phosphor screen and are converted to visible photons. An image intensifier is used in front of the CCD to further increase the output signal. The CCD contains a 1 inch by 1 inch array of 1024×1024 pixels. To further reduce the background light caused by the strong plasma emission collected by the detector, a set of 1 mm diameter pinholes were placed after the plasma and before the second grating. The pinholes were small enough to limit the collection angle of the spherical mirror, but large enough to let through the highly collimated soft x-ray laser. The interferograms obtained have a high fringe visibility (> 0.7) over the entire field of view.

3.3. Complementary diagnostics

In addition to soft x-ray laser interferometry, other diagnostics instruments were set up in order to record important complementary information about the plasmas. A visible interferometer operating at 532 nm was used to obtain electron density maps of the plasma at lower densities (1×10^{17} to 1×10^{18} cm^{-3}), and time integrated spectra of the plasma in the 3.5 – 18.5 nm range were also recorded.

3.3.1. Visible interferometry

In the particular case of the half-cylindrical cavities, a dense laser-created plasma focus can be seen to evolve for several tens of nanoseconds, with a bow shock developing outside the cavity later in time (see Chapter 4). However, the densities of this feature are too low to be diagnosed with the soft x-ray interferometer. Therefore, a visible interferometer at $\lambda=532$ nm was also built to probe the later times of the c-grooves plasma focus.

The interferometer uses a Mach-Zehnder configuration with two beam splitters and mirrors. The laser source used for this interferometer was the output of a Nd:YAG laser operating at $\lambda=1064$ nm, that was subsequently frequency doubled using a KDP crystal. The target was placed into the path of the laser in one arm of the interferometer. The plane of the target was imaged onto the CCD detector described previously using a focusing lens, yielding the same magnification as with the soft x-ray interferometer (25 \times). The beam splitters used in this setup were all coated at 532 nm for 50% reflection/transmission. Because this is a visible interferometer, the alignment procedure was easier than the soft x-ray interferometer as it could be fully aligned before putting the system under vacuum, requiring only minor adjustments on the motorized mirrors. The longer wavelength of the probe beam means that lower electron densities (1×10^{17} to 1×10^{19} cm^{-3}) can be probed.

3.3.2. Spectrometer

In the laser-created plasma jets experiment described in Chapter 5, another diagnostic instrument was added to the soft x-ray interferometer in order to record the time integrated spectra of the plasma jet. Soft x-ray emission from the plasma jet was obtained using a variable-space grating that is aberration-corrected for operation at a grazing incidence angle of 3 degrees [11]. The spectra were recorded using a back-illuminated 1024×1024 pixels charge-coupled device camera, positioned to collect light in the 35–185 Å wavelength range. A 200-nm-thick Zr filter was used to block visible light.

3.4. Target geometries

Different target shapes of various materials were used in the experiments presented herein. In all cases, the target is placed on a motorized holder inside the interferometer to enable precise positioning of the target with respect to the irradiating and probe beams. The target is moved to a new groove after every two to three shots to allow for reproducible plasma conditions.

3.4.1. Half-cylindrical targets

The base for these targets is a thin slab of material 1 mm in width, 5 mm depth and 5 cm in height. A precise drill bit 500 μm in diameter is used to drill holes through the width of the target, separated by 1 mm each. The target is then subsequently sanded to obtain 1 mm long half cylinders, 500 μm at the opening. In a single target slab, 30 to 40 of these *C-grooves* can be accessed for the experiment. Figure 3.6 shows a schematic drawing of the c-grooved target. The resulting plasma focus and late bow shock are discussed in Chapter 4.

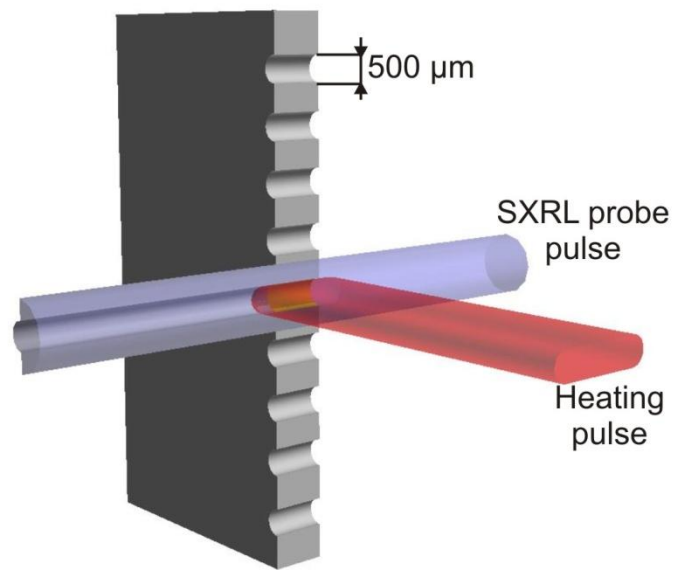


Figure 3.6. Schematic view of the semi-cylindrical targets. The cavities are 500 μm in diameter along the 1 mm long target, and separated by 1 mm.

3.4.2. V-grooved targets

In order to create planar plasma jets (studied in Chapter 5), triangular grooves were machined in thin slabs of aluminum, copper or carbon 1 mm wide, 5 mm deep and 5 cm high. The 1 mm long grooves are 250 μm deep and 500 μm wide at the target surface. A small saw is used to machine precisely those *v-grooves*, separated by 1 mm. A single target contains 30-40 such grooves. A typical grooved is presented on Figure 3.7.

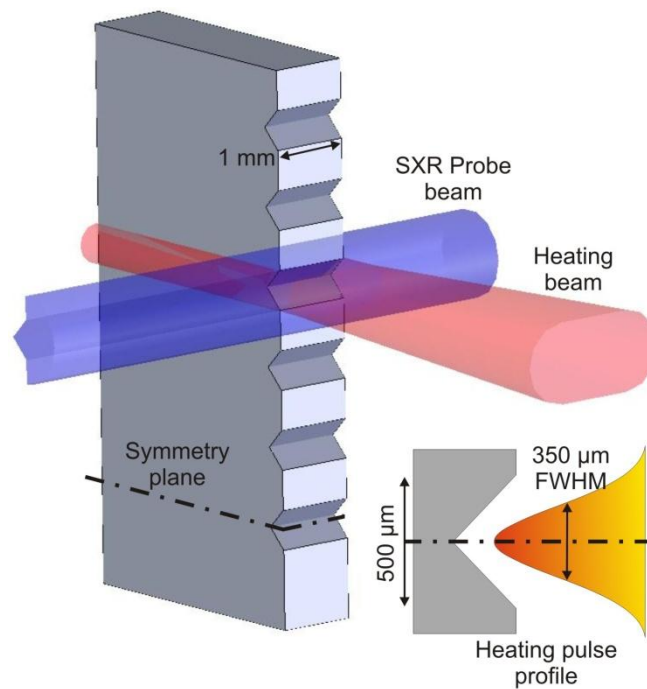


Figure 3.7. Schematic view of the V-groove targets. A 90 degree angle slot was machined into the 1 mm long target. Each groove is separated by 1 mm.

3.4.3. Conical targets

For the last experiment presented herein (Chapter 5), conical holes were drilled into slabs of copper 1 mm wide. The cones have an angle of ~ 90 degree and a typical depth of $\sim 250 \mu\text{m}$, with a $500 \mu\text{m}$ opening. Particular care was paid to the shape of the target bottom, so as to have a rounded or flat bottom no larger than $150 \mu\text{m}$, since the bottom of the cavity was found to play an important role in the dynamics of the resulting plasmas. The conical cavities, separated by 1 mm, are shown in Figure 3.8. Up to 40 cones can be machined onto a single slab target.

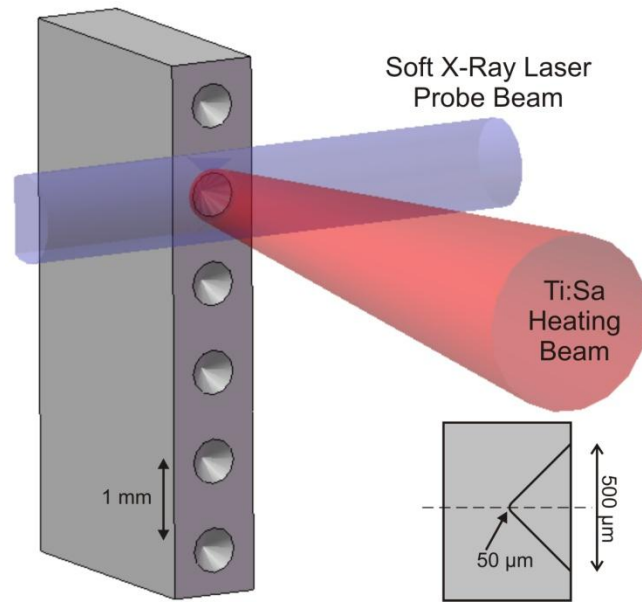


Figure 3.8. Schematic view of the conical target. Each cone is $500 \mu\text{m}$ in diameter and $250 \mu\text{m}$ deep. The tip of the cone was specified to be less than $50 \mu\text{m}$. The cones are separated by 1 mm.

3.5. Irradiating laser

The irradiating laser pulses used to create the various plasmas studied herein were produced by a Titanium Sapphire (Ti:Sa) laser operating at a center wavelength of 800 nm [12]. The Ti:Sa laser consists of a mode-locked oscillator and three stages of chirped-pulse amplification (CPA) (see Figure 3.9). The nanojoule pulses produced by the laser oscillator are stretched and subsequently amplified in a chain of three Ti:Sa amplifiers. Eight passes through the first stage amplifier increase the pulse energy to about 2 mJ with a pulse duration of ~ 180 ps. Further amplification in the five-pass second stage bow-tie amplifier increases the pulse energy to about 200 mJ. The output of the second stage is spatially filtered and injected into a final three-pass amplifier that is pumped by a 5 J frequency doubled Nd:YAG laser. This final amplification stage increases the 800 nm pulse energy up to a maximum of 2 J. A selected part of the output laser pulse is then redirected towards the target to create the colliding plasmas. The pulse is first filtered through a spatial vacuum filter to obtain a smoother beam. Depending on the experiment, a line focus or spot focus was used. To create the line focus irradiating the half-cylindrical and v-shaped grooves, a 350 μm (FWHM) spot focus is subsequently formed onto the target plane using a 7 m focal length spherical lens and stretch into a line with a combination of positive and negative 1 m focal length cylindrical lenses equivalent to a $f = 22$ m cylindrical lens. Adjustment of the separation between the two cylindrical lenses allows the length of the line to be modified, while the rotation of both cylindrical lenses controls the tilt of the line. The line is typically 1.5 mm long in order to uniformly irradiate the 1 mm c-grooves and v-grooves target. To create the spot focus used in the conical target experiment, the output of the Ti:Sa laser was focused into a ~ 250 μm (FWHM) spot using a single 5 m focal length spherical lens.

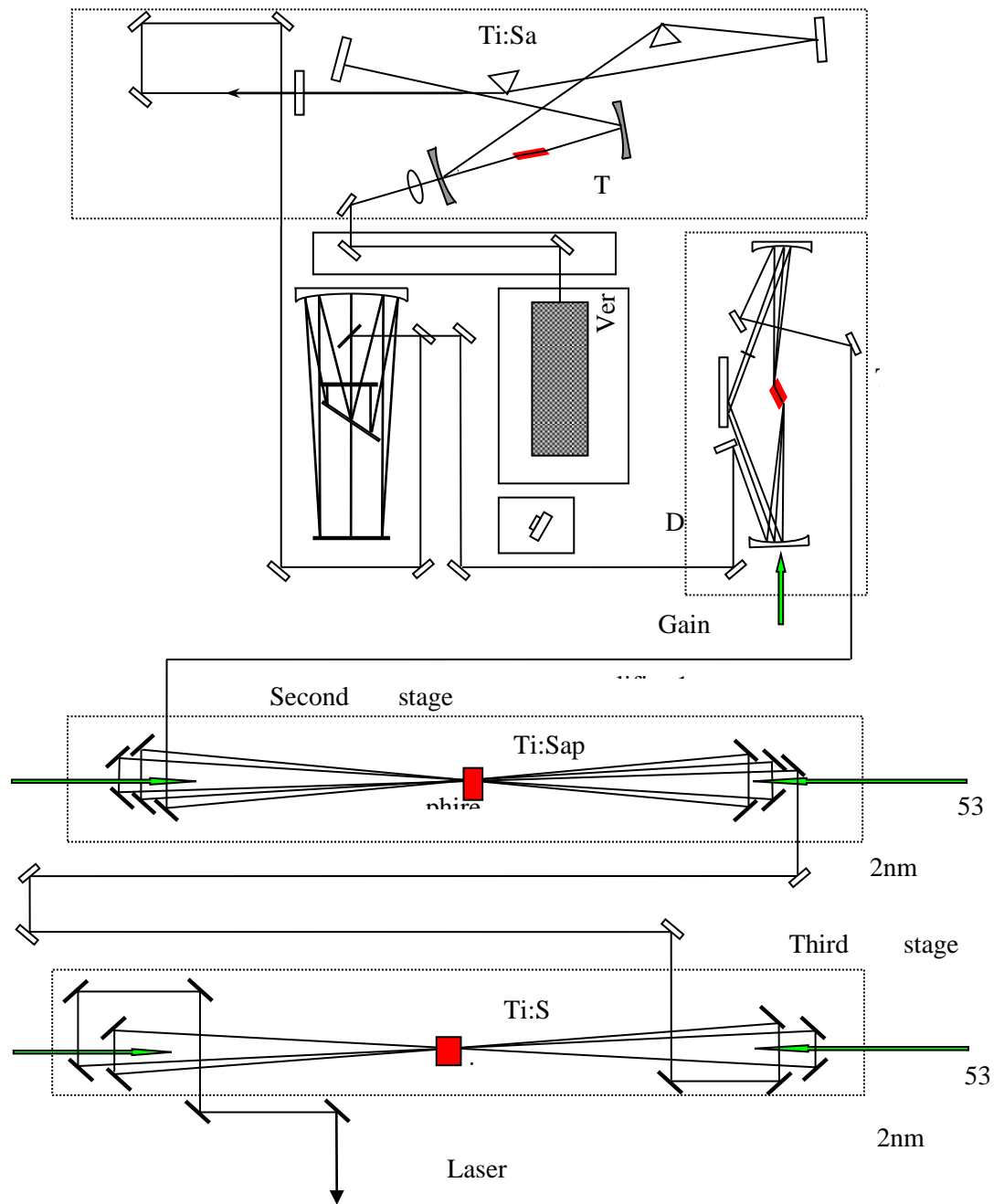


Figure 3.9. Schematic of the Titanium Sapphire (Ti:Sa) table top laser. The initial pulse (generated from the oscillator) is subsequently amplified by three stages of CPA amplifications

In all experiments, the beam shape, quality and positioning was monitored and recorded on every shot. A beam splitter (with 4% reflectivity) was placed into the path of the beam, after

the focusing lens, and redirected part of the beam onto an offline CCD detector. By taking a series of reference shots, it was possible to correlate the intensity of the beam recorded onto the CCD with the actual energy of the laser beam hitting on the target.

3.6. Data analysis

Using the experimental setup described above, high contrasts interferograms of the various dense plasmas were obtained. The raw data, as acquired from the detection system, is a two dimensional image representing the phase shift of the probe beam, with the fringes shifting away from the target. In order to convert this data into corresponding two dimensional electron density maps, several steps of analysis are necessary.

The first step is to convert the raw data into a map showing how much the fringes at each point have shifted from a reference interferogram, taken without the presence of plasma. Starting from the reference interferogram, the initial position of the maximum of each fringe is outlined, as shown in Figure 3.10.a. The number of points used to sample the fringe determines the resolution of the analysis: a larger number of samples results in better confidence in the data analysis, but significantly increases computing time. Once this *skeleton* of the reference interferogram is obtained, the process is repeated for the data interferogram (Figure 3.10.b). By comparing how much each point on a particular fringe has shifted, the two dimensional fringe shift map is constructed (shown in Figure 3.10.c).

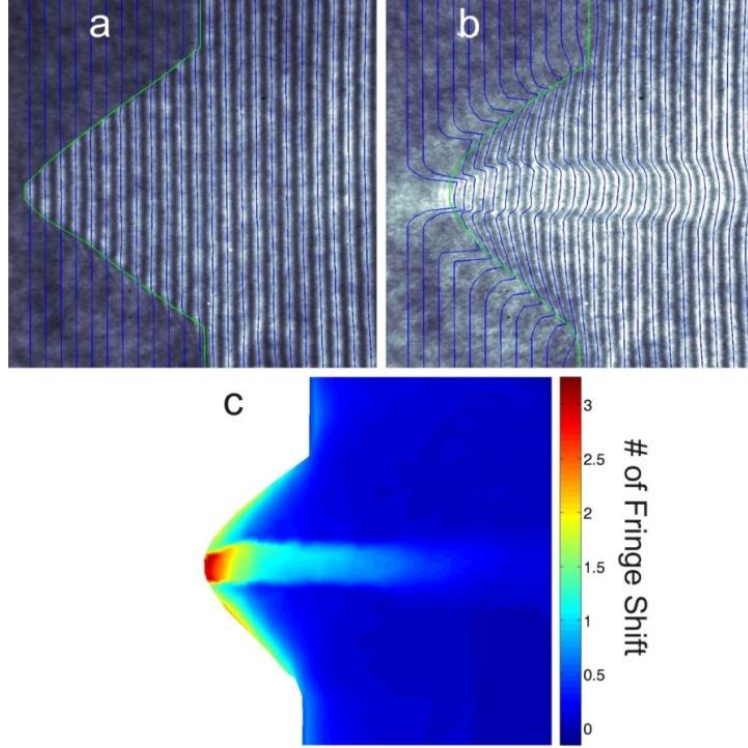


Figure 3.10. First step of the data analysis of an Al plasma jet from a v-grooved target configuration. A skeleton of the reference interferogram (a, blue lines) and data interferogram (b, blue lines) are created by following the maximum of each fringe. The difference in the position between the two skeletons results in the fringe shift map (c). This analysis is only valid in the region where fringe shifts could be identified (i.e. to the right of the green line in the interferograms).

Once the fringe shift map is obtained, the index of refraction map can be calculated from the following relationship:

$$N_{fringe} = \frac{1}{\lambda} \int_0^L (1 - \eta) dl \quad (\text{eq.3.1})$$

where L is the plasma length, $\eta = \sqrt{1 - n_e/n_c}$ (eq.3.2), and n_c is the critical density

$$n_c = \frac{\epsilon_0 \omega^2 m}{e^2} \approx \frac{1.1 \times 10^{21}}{\lambda^2(\text{cm})} \quad (\text{i.e. the maximum density for which light can penetrate the plasma at this wavelength}).$$

Equation (eq.3.1) must be applied at each point of the fringe shift map.

3.6.1. Fringe shift map to electron densities: 2D approximation

In both the half-cylindrical and v-grooves experiments, the plasmas created are 1 mm in length along the direction of propagation of the probe beam (see Figure 3.11). Assuming that there are no edge effects in the plasma (i.e. there is no significant lateral expansion in the z direction), as the probe beam travels through the plasma it sees a constant index of refraction. In this case, equation (eq.3.1) can be simply rewritten as:

$$N_{fringe} = \frac{1}{\lambda} \int_0^L (1 - \eta) dl \cong \frac{1}{\lambda} (1 - \eta)L$$

Since $n_e \ll n_c$, this equation can be further simplified as:

$$N_{fringe} = \frac{n_e L}{2n_c \lambda}$$

This equation is then easily inverted, and the electron density n_e obtained for each point from the fringe shift map.

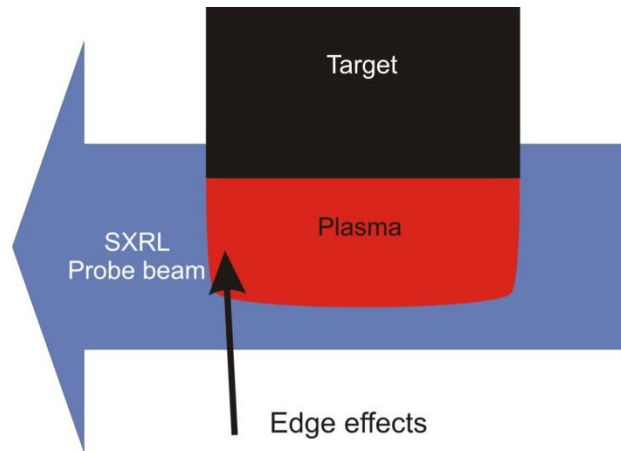


Figure 3.11. Top view of the target, with soft x-ray travelling along the z axis, through the laser-created plasma. Non uniform densities exist at the edges of the plasma and might introduce errors in the analysis.

In certain cases and for particular wavelengths, fringes were observed to anomalously shift towards the target (i.e. negative fringe shift as opposed to the usual shift away from the target). According to equation eq.3.1, the number of fringe shift is negative for an index of refraction η greater than one. As the contribution of free electrons to the index of refraction is always less than one (from eq.3.2), this indicates that the contribution of bound electrons to η is significant in the region where negative fringe shift is observed. It was demonstrated [13] that negative values of the index of refraction of bound ions can significantly alter the index of refraction of a plasma, for example for C plasmas at soft x-ray wavelengths. The plasmas described in this dissertation are aluminum and copper plasmas probed with a soft x-ray laser operating at 46.9 nm. At this wavelength and for these materials, calculations indicate that only the free electrons should contribute to the index of refraction of the plasma.

3.6.2. Fringe shift map to electron densities in 3D plasmas: Analytical Spline Abel Inversion (ASAI) technique

In the case of the conical plasma jets of the experiment presented in Chapter 5, the laser probe beam travels through different plasma lengths, and therefore sees different indices of refraction along its path. This case is considerably more complex to analyze than that of the planar jet analysis. If the plasma is assumed to be *cylindrically symmetric* (as shown in Figure 3.12), the observed intensity recorded on the detector $I(y)$ can be transformed into the radial distribution profile of the plasma $\varepsilon(r)$ by using the Abel transform [14]:

$$I(y) = 2 \int_{y_0}^1 \frac{\varepsilon(r)r}{r^2 - y^2} dr \quad (\text{eq.3.2})$$

where y_0 is the y coordinate of the plasma edge at each x value. Therefore, the inverse of the Abel transform, also called the Abel inversion, provides the phase information $\varepsilon(r)$ from the experimentally measured values of intensities on the detector $I(y)$ in the form:

$$\varepsilon(r) = -\frac{1}{\pi} \int_r^R \frac{I'(y)}{\sqrt{y^2 - r^2}} dy \quad (\text{eq.3.3})$$

where $I'(y)$ is the first derivative of $I(y)$ with respect to y and R is the plasma radius. The Abel-inverted data obtained this way contains the phase information, and can be translated into the electron density by:

$$n_e(r) = 2n_c \lambda \varepsilon(r)$$

where n_c is the critical density ($5 \times 10^{23} \text{ cm}^{-3}$ at the probe wavelength) and $\lambda = 46.9 \text{ nm}$. There are several ways to solve this equation. Analytical methods fit experimental data to an analytical function whose direct Abel inversion is known. While this method is simple, very accurate and avoids most issues associated with discretization, experimental data may have distribution profiles that cannot be fitted with such functions. Numerical methods are usually preferred: the Abel inversion equation is transformed into a summation, easily computed but operating on a discrete (and thus less accurate) set of data. These numerical methods have high calculation speeds, and can be combined with some type of data fitting/smoothing for higher accuracy.

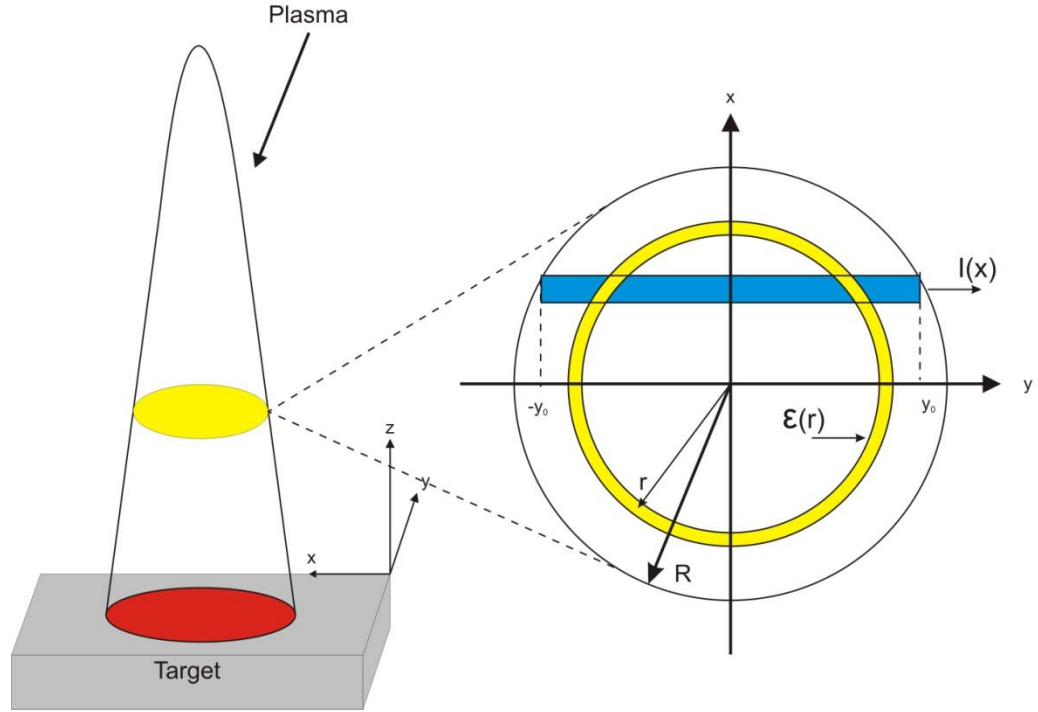


Figure 3.12. Abel inversion parameters on a transversal slice of cylindrically symmetric plasma jet.

There are many Abel inversion algorithms available for solving equation (eq.3.3). They range from any type of discretization method, to changing the integration variable. An analytic spline Abel inversion (ASAI) algorithm developed by Beniaminy and Deutsch [15] was chosen to analyze the experimental data obtained in this experiment. This technique was found to be reliable and stable with both noisy and noise-free inputs. A derivative-free inversion of equation (eq.3.2), derived by Beniaminy and Deutsch, was used as the base for the ASAI algorithm:

$$\varepsilon(r) = -\frac{1}{\pi} \left([I(1) - I(r)](1 - r^2)^{-\frac{1}{2}} + \int_r^1 [I(y) - I(r)] y (r^2 - y^2)^{-3/2} dy \right) \quad (\text{eq.3.4})$$

In practice, $I(y)$ is given as a set of discrete data points $I_j = I(y_j)$, where $j=1 \dots m$ (for example, the readout of a CCD camera), and a first smoothing step must be applied before evaluating the Abel inversion numerically to reduce input and processing noise.

An efficient and frequently used smoothing technique is to represent I_j by a piece-wise cubic spline function fitted to the data. This important step helps reduce noise amplification throughout the inversion process. $I(y)$ can then be defined by:

$$I(y) = \sum_{k=1}^{p-1} I_k(y) \quad (\text{eq.3.5})$$

where

$$I_k(y) = \begin{cases} 0, & y < \alpha_k \\ a_k y^3 + b_k y^2 + c_k y + d_k, & \alpha_k \leq y \leq \alpha_{k+1} \\ 0, & y > \alpha_{k+1} \end{cases}$$

and $\alpha_1, \alpha_2 \dots \alpha_k$ are the spline knots. The number of knots (p) and their positions (α_i) depend on the input data and are chosen by the fitting routine to satisfy the least-square condition.

The ASAI algorithm used in this analysis employs an analytic integration of the fitted spline, using the derivative-free formula from equation (eq.3.3). The following analytical expression of the Abel inversion, obtained by substituting (eq.3.5) into (eq.3.3), is then numerically evaluated:

$$\begin{aligned} \varepsilon(r) = & -\frac{1}{\pi} \left\{ \sum_{k=1}^{p-1} [a_k K_4(\alpha_k, \alpha_{k+1}) + b_k K_3(\alpha_k, \alpha_{k+1}) + c_k K_2(\alpha_k, \alpha_{k+1}) + d_k K_1(\alpha_k, \alpha_{k+1})] \right. \\ & \left. + a_{i-1} K_4(\alpha_i) + b_{i-1} K_3(\alpha_i) + c_{i-1} K_2(\alpha_i) + d_{i-1} K_1(\alpha_i) \right\} \\ & + \frac{1}{\pi} [3a_{i-1} r^2 \ln(r/2) + c_{i-1} \ln(r)] \end{aligned}$$

where i is the index of the smallest knot larger than the argument r , and

$$K_l(a, b) = K_l(b) - K_l(a) = \int_a^b y^l (y^2 - r^2)^{-3/2} dy$$

K_l can be found explicitly for $l=1\dots 4$ (see [15]). Defining $s = (r^2 - y^2)^{-1/2}$, one obtains:

$$K_1 = -\frac{1}{s}, \quad K_2 = -\frac{y}{s} + \ln(y + s)$$

$$K_3 = s - r^2s, \quad K_4 = \frac{ys}{2} - \frac{r^2y}{s} + 3r^2 \ln\left(\frac{y + s}{2}\right)$$

The ASAI algorithm was implemented in MATLAB. The program can be found in Appendix B. This method removes any sensitivity to noise distortion because of the derivative-free form of the Abel inversion, and reduces error propagation from discretization thanks to the spline-based interpolation of the input data. However, most Abel inversion algorithms rely on the assumption that the input data is symmetric. Non symmetric distribution can introduce major errors, and in the particular case of plasmas significantly change its width and densities. Therefore, particular care was taken to experimentally produce symmetrical jets.

Several steps were taken to ensure that the plasma jets were created with as close to cylindrical symmetry as possible. First, the tool used to punch the conical cavities was machined as precisely as possible in order to obtain high quality cones. During the punching process, aligning the tool perpendicular to the target surface was critical. When irradiating the target, the position of the laser heating beam was recorded and correlated to the position of the cone to ensure that the shot was centered on target. Experimental observations show that symmetrical plasmas can be obtained when the laser heating beam irradiates the center of the conical cavity within $\sim 50 \mu\text{m}$. If the laser hits the conical cavity outside of this area, a non-symmetrical plasma is created and the ASAI algorithm will return unrealistic values of the electron density.

Once the fringe shift map of a particular interferogram is obtained, another step is performed to ensure the input data for the ASAI algorithm is symmetrical. The axis of symmetry of the data is first obtained from the map (as depicted in Figure 3.13) by extracting the points of maximum shift along the y-direction and fitting a line to it. Then, the top and bottom part of the map are subsequently inverted. The resulting data was found to differ by less than 10%, within

the error of our measurements. Typically, a smoothed averaged dataset between the top and bottom halves of the fringe shift map was used with similar results.

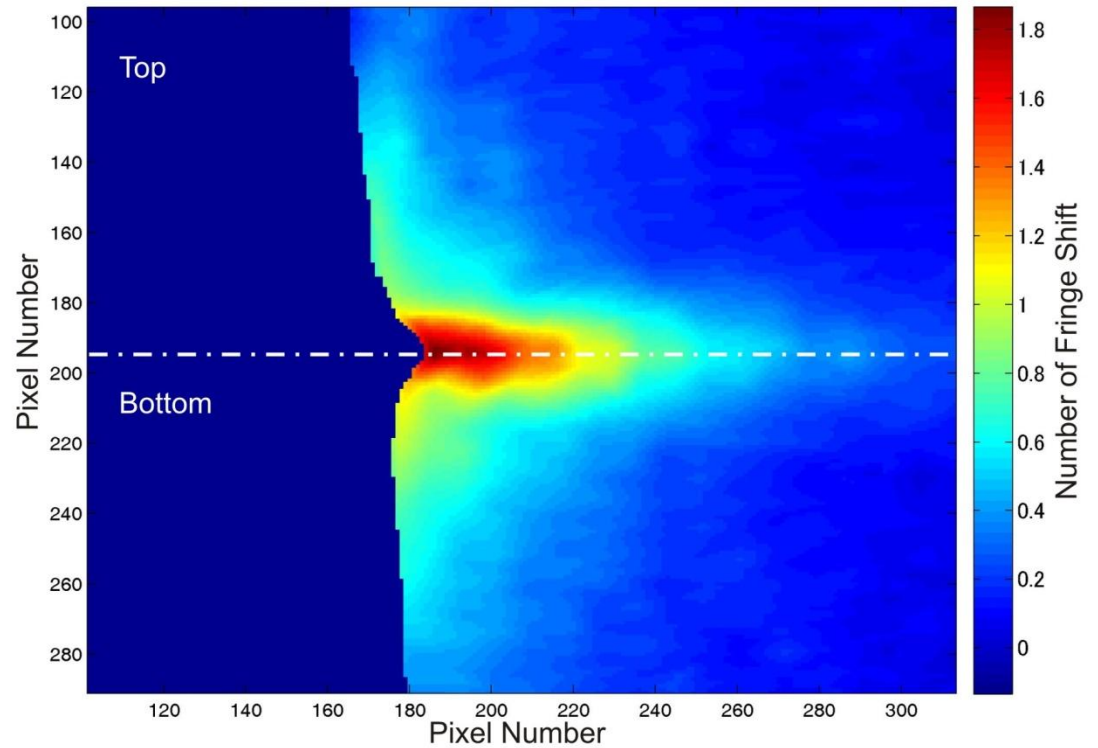


Figure 3.13. Fringe shift map of a Cu plasma jet at 5.5 ns, before Abel inversion. The dashed line represents the axis of symmetry of the plasma jet.

3.7. References

- [1] J. Filevich, K. Kanizay, M.C. Marconi, J.L.A. Chilla and J.J. Rocca, “Dense plasma diagnostics with an amplitude-division soft x-ray interferometer based on diffraction gratings,” *Optics Lett.*, vol. 25, no. 5, pp. 356-358, 2000.

- [2] Yu A. Uspenskii, V. E. Levashov, A. V. Vinogradov *et al.*, “High-reflectivity multilayer mirrors for a vacuum-ultraviolet interval of 35-50nm,” *Opt. Lett.*, vol. 23, no. 10, pp. 771-773, 1998.
- [3] J.J. Rocca, D.P. Clark, J.A. Chilla and V.N. Shlyaptsev, “Energy extraction and achievement of the saturation limit in a discharge-pumped table-top soft x-ray amplifier,” *Phys. Rev. Lett.*, vol. 77, no. 8, pp. 1476-1479, 1996.
- [4] J. J. Rocca, V. Shlyaptsev, F. G. Tomasel, O. D. Cortazar, D. Hartshorn, J. L. A. Chilla, “Demonstration of a discharge pumped table-top soft-x-ray laser,” *Physical Review Letters*, vol. 73 no. 16, pp. 2192-2195, 1994.
- [5] B. R. Benware, C. D. Macchietto, C. H. Moreno, J. J. Rocca, “Demonstration of a high average power tabletop soft x-ray laser,” *Physical Review Letters*, vol. 81 no. 26, pp. 5904-5807, 1998.
- [6] J. J. Rocca, D. P. Clark, J. L. A. Chilla, V. N. Shlyaptsev, “Energy extraction and achievement of the saturation limit in a discharge-pumped table top soft x-ray amplifier,” *Physical Review Letters*, vol. 77 no. 8, pp. 1476-1479, 1996.
- [7] Y. Liu, M. Seminario, F. G. Tomasel, C. Chang, J. J. Rocca, D. T. Attwood, “Achievement of essentially full spatial coherence in a high-average-power soft x-ray laser,” *Physical Review A*, vol. 63 no. 033802, 2001.
- [8] N.A. Bobrova, S.V. Bulanov, T.L. Razinkova *et al.*, “Dynamics of a pinch discharge in capillaries,” *Plasma Physics Reports*, vol. 22, no. 5, pp. 349-362, 1996.
- [9] Y. Liu, M. Seminario, F.G. Tomasel *et al.*, “Achievement of essentially full spatial coherence in a high-average-power soft-x-ray laser,” *Physical Review A*, vol. 63, no. 033802, 2001.
- Copyright (C) 2010 The American Physical Society, pp. 033802, 2001.

- [10] B.M. Luther, L. Furfaro, A. Klix *et al.*, “Femtosecond laser triggering of a sub-100 picosecond jitter high-voltage spark gap,” *Appl. Phys. Lett.*, vol. 79, no. 20, pp. 3248-3250, 2001.
- [11] T. Kita, T. Harada, N. Nakano, and H. Kuroda, “Mechanically ruled aberration-corrected concave gratings for a flat-field grazing-incidence spectrograph,” *Applied Optics*, vol. 22, no. 4, pp. 512-513, 1983.
- [12] B. M. Luther, Y. Wang, M. A. Larotonda *et al.*, “Saturated high-repetition-rate 18.9-nm tabletop laser in nickel molybdenum,” *Opt. Lett.*, vol. 30, no. 2, pp. 165-167, 2005.
- [13] J. Filevich, J. J. Rocca, M. C. Marconi *et al.*, “Observation of a Multiply Ionized Plasma with Index of Refraction Greater than One,” *Physical Review Letters*, vol. 94, no. 13, pp. 135005, 2005. Copyright (C) 2010 The American Physical Society, pp. 035005, 2005.
- [14] R. Alvarez, A. Rodero, M. C. Quintero, “An Abel inversion method for radially resolved measurements in the axial injection torch,” *Spectrochimica Acta Part B*, vol. 57, 2002.
- [15] M. Deutsch, and I. Beniaminy, *J. Appl. Phys.*, vol. 54, no. 137, 1983.

Chapter 4. Dynamics of colliding dense plasmas in semi-cylindrical cavities studied using soft x-ray and optical interferometry

4.1. Introduction

The study of the dynamics of dense plasmas created by laser irradiation of cylindrical cavities is of interest for both fundamental plasma physics understanding and applications. The latter includes the hohlraums used in the implementation of indirect drive inertial confinement fusion (ICF). Laser heating of cylindrical hohlraums [1-2] creates pressure gradients near the walls that radially accelerate the plasma distributed along the surface towards the axis of the cavity, where it collides. This interaction of converging plasmas depends on their degree of collisionality and can range from stagnation to extended interpenetration, as determined by the geometry and irradiation conditions [3]. Comparison of direct measurements of the electron density evolution with code simulations can contribute to a better understanding of the plasma dynamics and is important to benchmark these complex codes and determine their regimes of validity. In this chapter, the study of dense plasmas created by irradiation of a semi-cylindrical cavity is presented. Aluminum and copper targets were irradiated with pulses of 120 ps duration at intensities of 1 - 1.5×10^{12} W.cm⁻². The high contrast interferograms obtained depict the evolution of the colliding dense plasmas.

During the study of these plasmas we also observed extreme ultraviolet plasma self-emission from a long and narrow arc outside the cavity, indicative of the presence of a bowshock. Bow shocks are of interests in astrophysics [4-5] and have been studied in the laboratory [6]. In this chapter we also present the study of these shocks using interferometry and two-dimensional radiation hydrodynamic code simulations. Optical interferometry was used to complement soft x-ray laser interferometry in mapping the lower density regions where the shorter wavelength probe is insensitive. The combination of both interferometry techniques provides the ability to measure, for these particular plasmas, electron densities within the range from $5 \times 10^{17} \text{ cm}^{-3}$ to $1 \times 10^{20} \text{ cm}^{-3}$, with the highest value limited by probe beam refraction.

4.2. Soft x-ray interferometry of dense Al colliding plasmas

This section discusses the evolution of dense colliding laser-created aluminum and copper plasmas. The plasmas were created by irradiating semi-cylindrical aluminum targets at an intensity of $1.1 \times 10^{12} \text{ W.cm}^{-2}$ with 650 mJ laser pulses from a Ti:Sa laser shaped into a 300 μm FWHM wide by 1.5 mm long line focus. The target was made of 99.9% pure aluminum [7]. The setup and targets used in this experiment is described in Chapter 3.

4.2.1. Experimental results

A series of interferograms which describe the evolution of the laser-created aluminum plasmas is presented in Figure 4.1. The irradiating laser impinges from the right of the figure, perpendicular to the target. The time delays are measured with respect to the peak of the

irradiating pulse. The solid black line represents the target position. Each frame was taken under similar conditions (line focus width, length, energy and position respect to the groove) and the target was moved to a new groove after every other shot.

Early on in the plasma evolution (0.8 and 1.3 ns frames), slight fringe shifts are observed in the region close to the target. This shows that the irradiating pulse ablates the material at the bottom of the half-cylinder cavity, creating a plasma that rapidly expands away from the wall and towards the central region of the cavity. At later times, the interferograms show a region near the axis of the cavity where a high number of fringe shifts is observed. This high density region forms rapidly as a result of the fast expansion of the plasma: this density increase is observed as early as 2.6 ns. The subsequent plasma expansion and relaxation of this high density region can be seen in the 4.3 ns and 6.5 ns frames. At later times in the evolution (e.g. 10.7 ns interferogram) the plasma undergoes significant recombination and cooling. The probe beam is strongly absorbed at that time.

Six electron density maps derived from the interferograms in Figure 4.1 are shown in Figure 4.2. The assumption was made that the plasma is uniform in the direction of propagation of the soft x-ray probe beam. This is justified by the use of the long smooth line focus that created the plasma, overfilling the cavity. Another assumption used in the analysis is that only the free electrons contribute to the index of refraction of the plasma. This can be verified to be the case through computations showing that at this particular wavelength the contribution of bound electrons to the index of refraction can be neglected in an aluminum plasma.

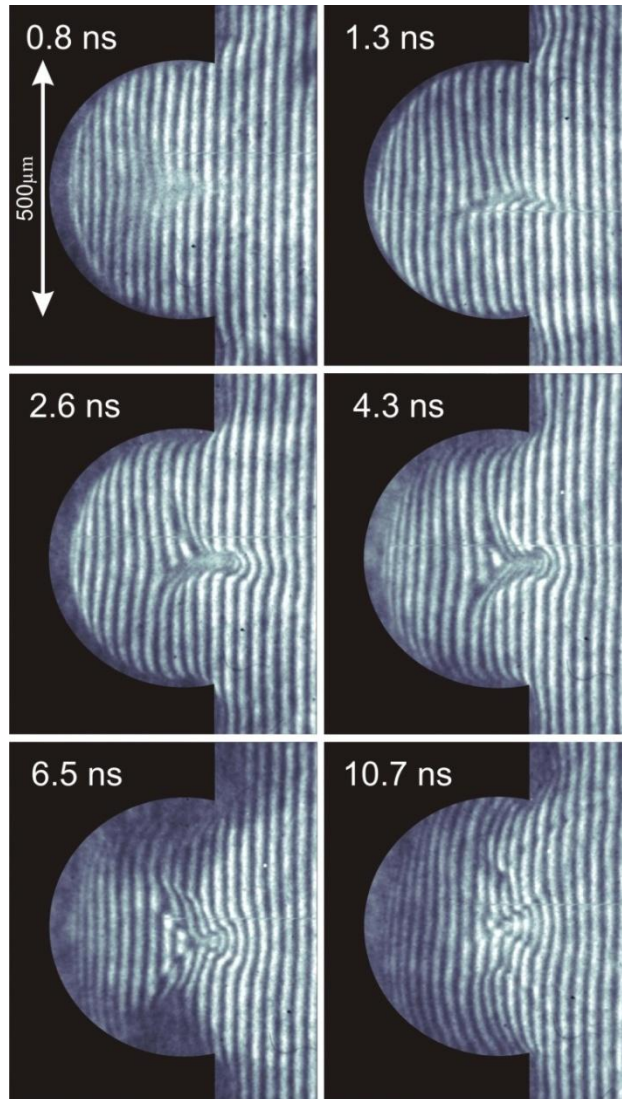


Figure 4.1. Sequence of soft x-ray laser interferograms describing the evolution of plasmas created by irradiating a semi-cylindrical Al cavity with a 120 ps pulse at an intensity of $1.1 \times 10^{12} \text{ Wcm}^{-2}$. Time delays are measured with respect to the peak of the irradiation laser beam incident from the right. The large number of fringe shifts close to the axis of the groove is indicative of a high density region created by the converging plasma.

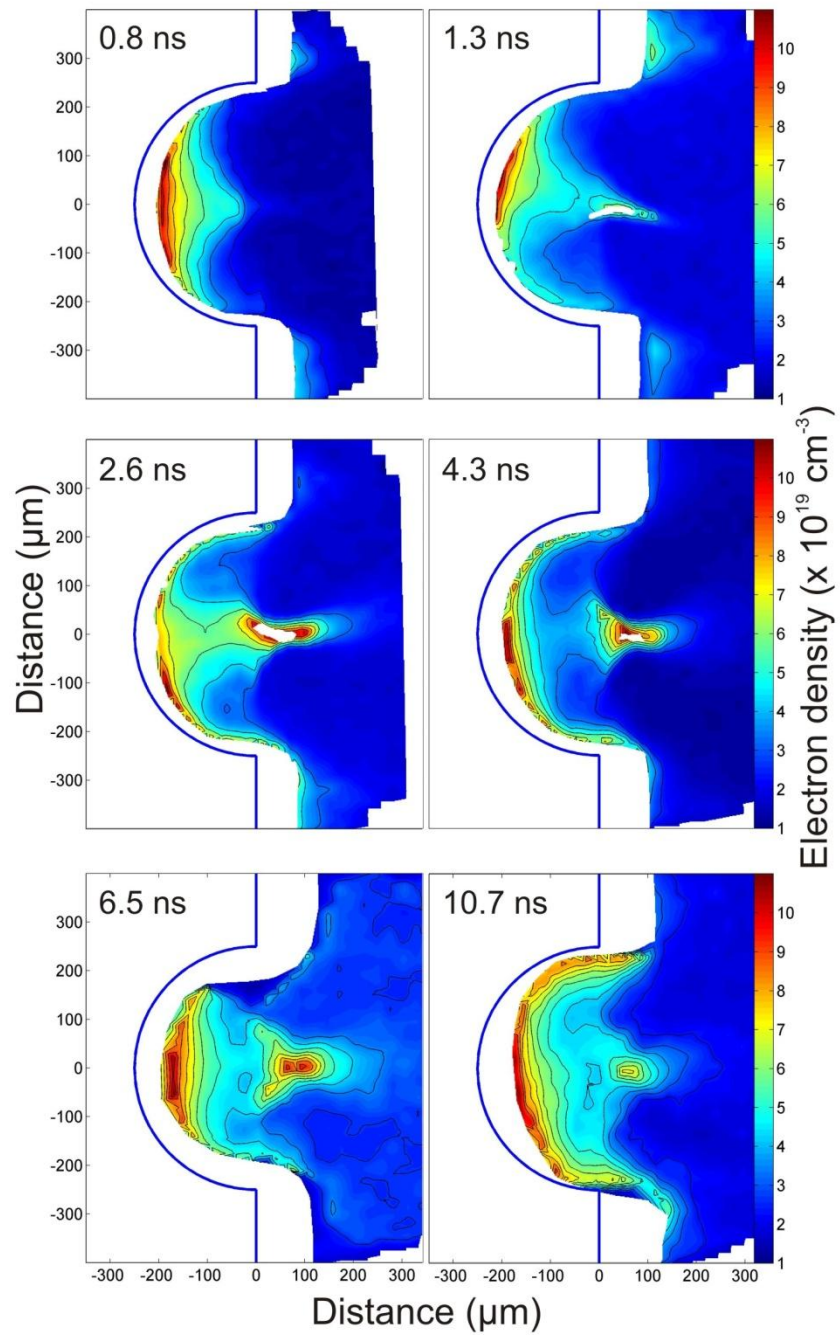


Figure 4.2. Measured electron density maps of the aluminum plasma corresponding to the interferograms of Figure 4.1.

The early stages of the plasma evolution corresponds to frames at 0.8 ns and 1.3 ns, after the end of the laser irradiation, when the plasma can be seen expanding from the walls. As early as 1.3 ns, the plasma is clearly observed to expand perpendicular to the walls and towards the center of the half-cylinder. Electron densities up to $9 \times 10^{19} \text{ cm}^{-3}$ are measured at 40 μm away from the walls at this time. The subsequent frames at 2.6 ns and 4.3 ns show the creation of a high density region on axis, with electron densities peaking above $1 \times 10^{20} \text{ cm}^{-3}$. Blurring of the fringes is observed in a small region on axis at 4.3 ns, caused by either plasma motion or very high density gradients. This complicates the analysis of the density. Therefore it is possible that the peak electron density during the plasma collision might be higher than the maximum observed for all the surrounding regions where the density measurements were possible. At late times (10.7 ns) after the plasma has recombined and cooled, the densest plasma region is located near the target walls. Density reaches values of $8\text{-}10 \times 10^{19} \text{ cm}^{-3}$ close to the walls of the half-cylindrical cavity, and the density on axis decreases to $\sim 6 \times 10^{19} \text{ cm}^{-3}$. At this time the plasma has cooled significantly and Al II and Al III ions are expected to be found. The bound electrons of these species contribute significantly to the index of refraction at the 46.9 nm wavelength of the probe [8]. Therefore, the analysis of the interferograms performed under the assumption that the index of refraction determined solely by free electrons is likely to overestimate the electron densities [8]. However, at earlier times when the plasma is highly ionized, the contribution of bound electrons should be negligible, and the electron density values quoted above should be accurate.

4.2.2. Discussion

Several simple calculations can help give insights on the physics of these plasmas. First, the degree of collision of the aluminum plasma can be computed using the Braginskii expression

for the ion-ion collision frequency [9]. However, the simple expression for collision is only valid for a single species in a Maxwellian plasma and do not take into account for relative drift. Analysis of the fluid transport equations derived from the Boltzmann equation for two species α and β [3, 10] yields an expression for the collision frequency that takes into account dynamic friction inside the plasma $\nu_{\alpha\beta} = \frac{8\sqrt{\pi}Z_{\alpha}^2Z_{\beta}^2n_{\beta}\Lambda}{m_{\alpha\beta}^2(\Delta v)^3} \left[\frac{\sqrt{\pi}}{2} \operatorname{erf}\left(\frac{\Delta v}{v_{th}}\right) - \left(\frac{\Delta v}{v_{th}}\right) \exp\left(-\frac{\Delta v^2}{v_{th}^2}\right) \right]$. In this expression, Z is the charge, $m_{\alpha\beta}$ the reduced mass, Λ the Coulomb logarithm, $v_{th} = 2k_B \left(\frac{T_{\alpha}}{m_{\alpha}} + \frac{T_{\beta}}{m_{\beta}} \right)$ is the thermal velocity and $\Delta v = |v_{\alpha} - v_{\beta}|$ the relative drift between the two species. The ion mean free path is then given by $\lambda_{ii} = \frac{v_{th}}{\nu_{\alpha\beta}}$. Considering the mean free path for a single species of ions (Al) at a mean ionization of $Z = 9$, with an assumed ion temperature of 50 eV and the measured electron density on axis of $5 \times 10^{19} \text{ cm}^{-3}$, the ion-ion collision rate can be derived as a function of the relative drift velocity. Figure 4.3a presents the results of those calculations. Large angles between the two converging parts of the plasma correspond to larger drift velocities. For an angle of $\frac{\pi}{2}$ as defined in Figure 4.3 (i.e. counter steaming plasma), the computed ion mean free path is less than 2.5 μm . This indicates that interpenetration can be neglected for all angles, and a large amount of collisions can be expected to take place in this plasma. The dynamics of the plasma is also affected by the uneven irradiation of the target by the heating. The 300 μm FWHM of the beam irradiates the central portion of the target surface included within a 74° angle area, as seen in Figure 4.3.b.

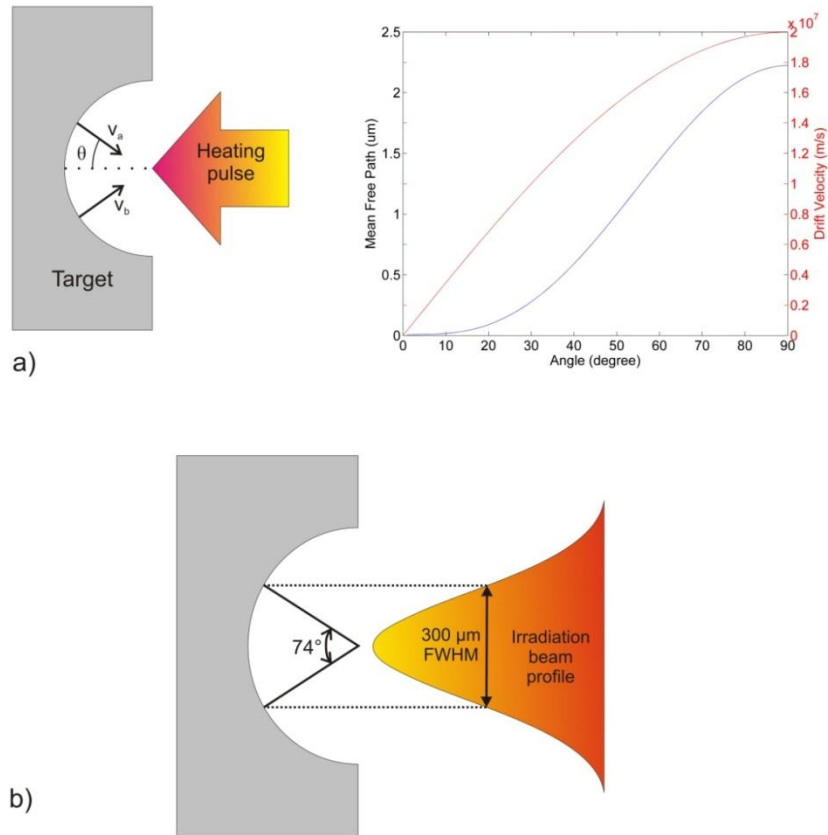


Figure 4.3. Calculations of the relative drift velocity (in red) and ion mean free path (in blue) as a function of the angle between two parts of the plasma (a). For high angles, the mean free path is small (less than 40 nm), thus many collisions are expected in the region where the plasma converges. The bottom diagram (b) illustrates the angle on the target that is being irradiated by the full width half maximum of the heating beam. 76% of the total laser beam energy is deposited in this area.

Assuming the beam is Gaussian, 76% of the total beam energy is deposited on this area. Note that 95% of the energy is deposited inside the 500 μm groove, leaving 5% of the energy irradiating the outside of the target, creating smaller secondary plasmas on the front side of the target. This uneven heating causes the mass that originates from the bottom of the target, where the irradiation and the plasma pressure are maximum, to be more strongly accelerated, causing it to arrive first on axis. Since the particles originating from the bottom of the groove have small

relative drift velocities, their ion mean free path is smaller than 1 μm . This again indicates that this plasma is highly collisional. Note that this discussion is also valid for the copper plasma, the only difference being the velocities of the particles will be lower as the atoms are more massive.

4.3. Soft x-ray interferometry of dense copper plasmas

This section describes and discusses the results of interferometry measurements conducted in copper plasmas created by irradiation of similar semi-cylindrical cavities. The line focus used in this experiment was 350 μm wide, 1.5 mm long and irradiated the target with an intensity of $1.5 \times 10^{12} \text{ W.cm}^{-2}$. The target was made of 99.9% pure copper [7].

A sequence of interferograms for the copper plasma is presented in Figure 4.4. Early on the plasma evolution (up to 2 ns) the fringes are observed to bend in the region close to the target. This shows the creation of an expanding plasma at the target surface. At later times (4.6 ns, 6.2 ns and 7.6 ns) the interferograms show the formation, expansion and relaxation respectively of a dense region near the axis of the half-cylindrical cavity where a large number of fringe shifts can be seen. This region is formed by the convergence of the plasma that expanded away from the wall. In those frames, absorption can be seen close to the wall of the target. The last frame of the sequence (12 ns) shows the late stage of the plasma evolution, where a small fringe shift can still be observed. However, at this time absorption of the probe beam is very significant due to photoionization of low charge ions.

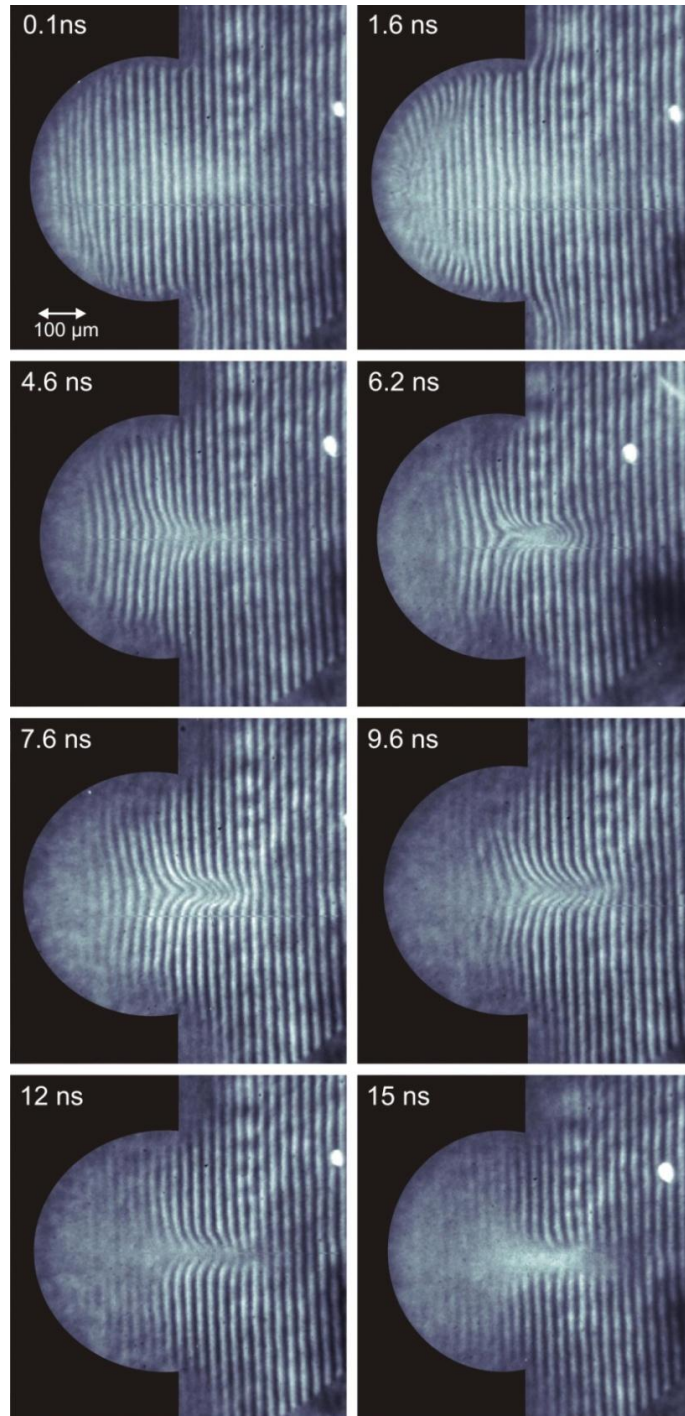


Figure 4.4. Sequence of soft x-ray interferograms describing the evolution of Cu plasma created by irradiation of a semi-cylindrical cavity. Time delays are measured with respect to the peak of the irradiation laser beam (incident from the right). The large number of fringe shift near the centre of the cavity in the 6.2 ns frame represents the formation of a dense converging plasma.

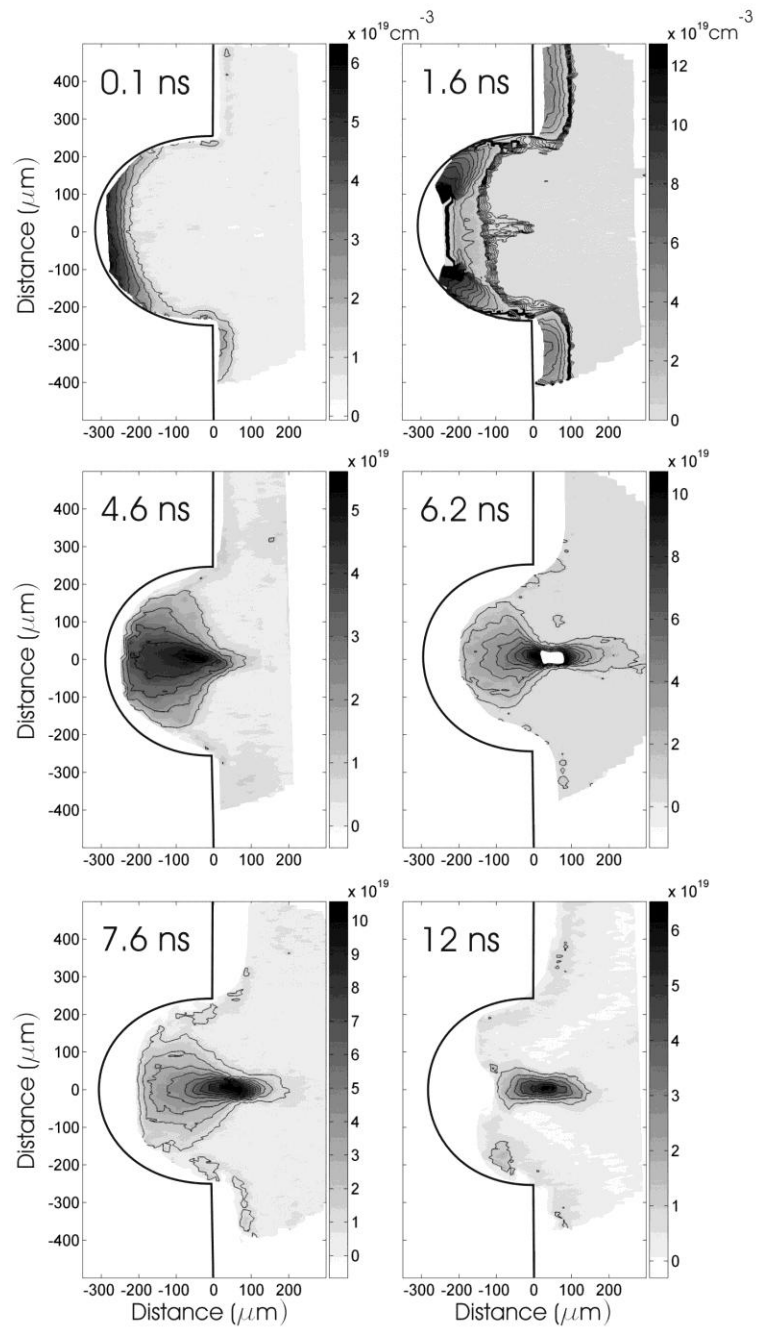


Figure 4.5. Electron density maps of Cu plasmas corresponding to the interferograms of Figure 4.4. The electron density of the central region on axis exceeds $1 \times 10^{20} \text{cm}^{-3}$. In the small region (in white) in the 6.2 ns frame, the density might be high, but blurring of the fringes complicates the analysis. The black solid line outlines the target position.

The six corresponding electron density maps derived from the interferograms in Figure 4.4 are shown in Figure 4.5. The previously stated assumption of plasma uniformity is still valid. The early interferograms (up to 2 ns after the arrival of the irradiating pulse on target) show the formation and expansion of the laser-created plasma, with electron densities of 6×10^{19} to $9 \times 10^{19} \text{ cm}^{-3}$ at distances between 40 and 100 μm from the walls of the cavity. As the plasma converges at the center of the semi-cylindrical target, the electron density dramatically increases to reach values higher than $1 \times 10^{20} \text{ cm}^{-3}$. At later times, the electron density in the plasma focus decreases to values as low as $6 \times 10^{19} \text{ cm}^{-3}$. Absorption close to the target prevents measurements in this region.

During the study of the colliding copper plasmas, an interesting feature was observed. Time integrated self-emission images of the plasma in the extreme ultra violet region of the spectrum were recorded and showed the presence of a long and narrow arc emitting light outside the cavity, as shown in Figure 4.6. This indicates the presence of a bow shock, most likely forming at late times. However, no fringe shifts were detected when probing the copper plasma using the soft x-ray laser interferometer. This means that the SXRL interferometer was not sensitive to the low densities of the bow shock. Therefore, a visible interferometer operating at a wavelength of 532 nm was used to probe the bow shock. The resulting interferograms and inferred plasma densities are discussed next.

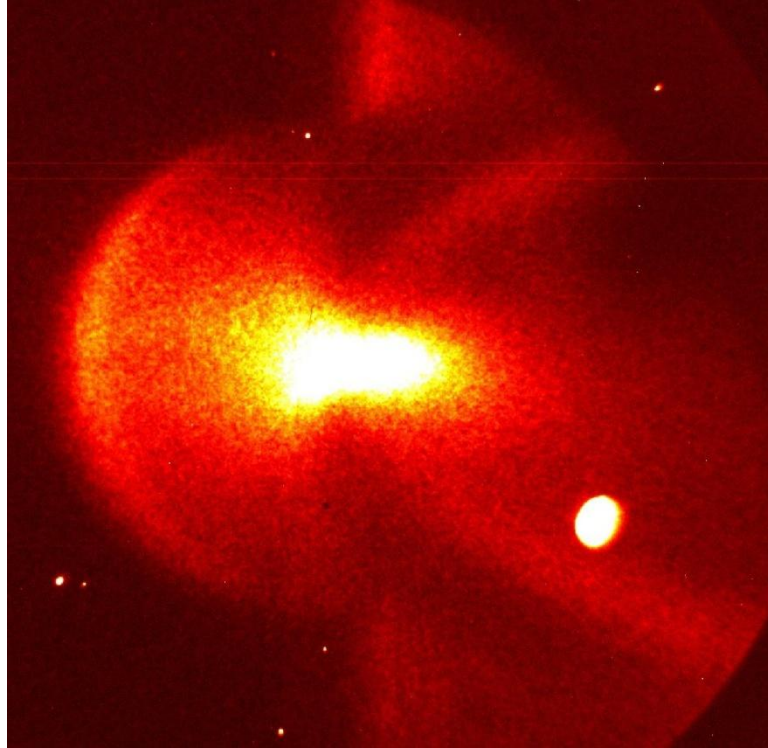


Figure 4.6. Time integrated self-emission of a Cu plasma focus. A bow shock like structure can be seen extending outside of the cavity.

4.4. Study of bow shock formation and evolution in laser-created copper colliding plasmas

4.4.1. Experimental results

Using the visible interferometer described in Chapter 3, a series of interferograms mapping the evolution of the bow shock was obtained. Figure 4.7 shows a sequence of selected 532 nm interferograms that describe the evolution of the lower density regions of the Cu plasma. The interferograms clearly show the development of a quasi-stationary bow shock structure

outside the cavity. This plasma structure starts as two narrow arcs close to the axis of the semi-cylinder. As the plasma evolves, the arcs are stretched in length and the distance and angle between them widens slowly. Simultaneously, the width of the shock is observed to increase with time. This continues until the shock fades after about 70 ns. Figure 4.8 shows the electron density maps obtained from the interferograms under the assumption that the plasma is uniform along the axial direction. The density maps show that the shock reaches a peak electron density of $\sim 6 \times 10^{18} \text{ cm}^{-3}$ at 20 ns. The first three frames of Figure 4.8, that illustrate the early stages of the evolution, show plasma expanding from the flat frontal surface of the target. Similar bow shock structures were observed following the irradiation of carbon, aluminum and silver targets, corresponding to plasmas with atomic numbers ranging from 6 to 47. As expected, the speed at which the shocks evolve was observed to be progressively slower as the atomic mass of the material increases. For all materials the shocks are observed to evolve from a curved to a straight shock front. The speed at which this transition occurs depends on the atomic mass.

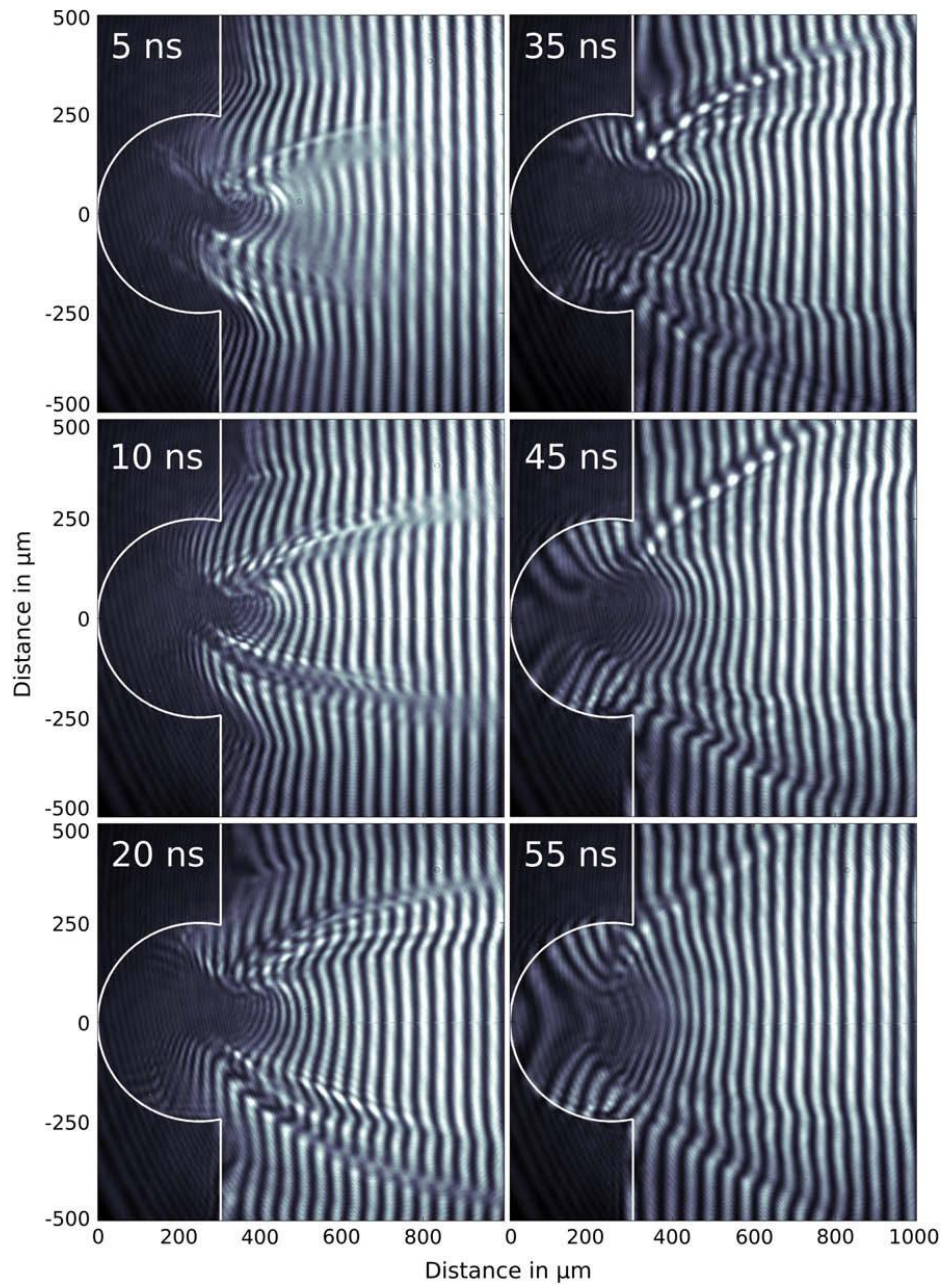


Figure 4.7. Sequence of interferograms depicting the evolution of the Cu bow shock. The probe beam wavelength used was 532 nm.

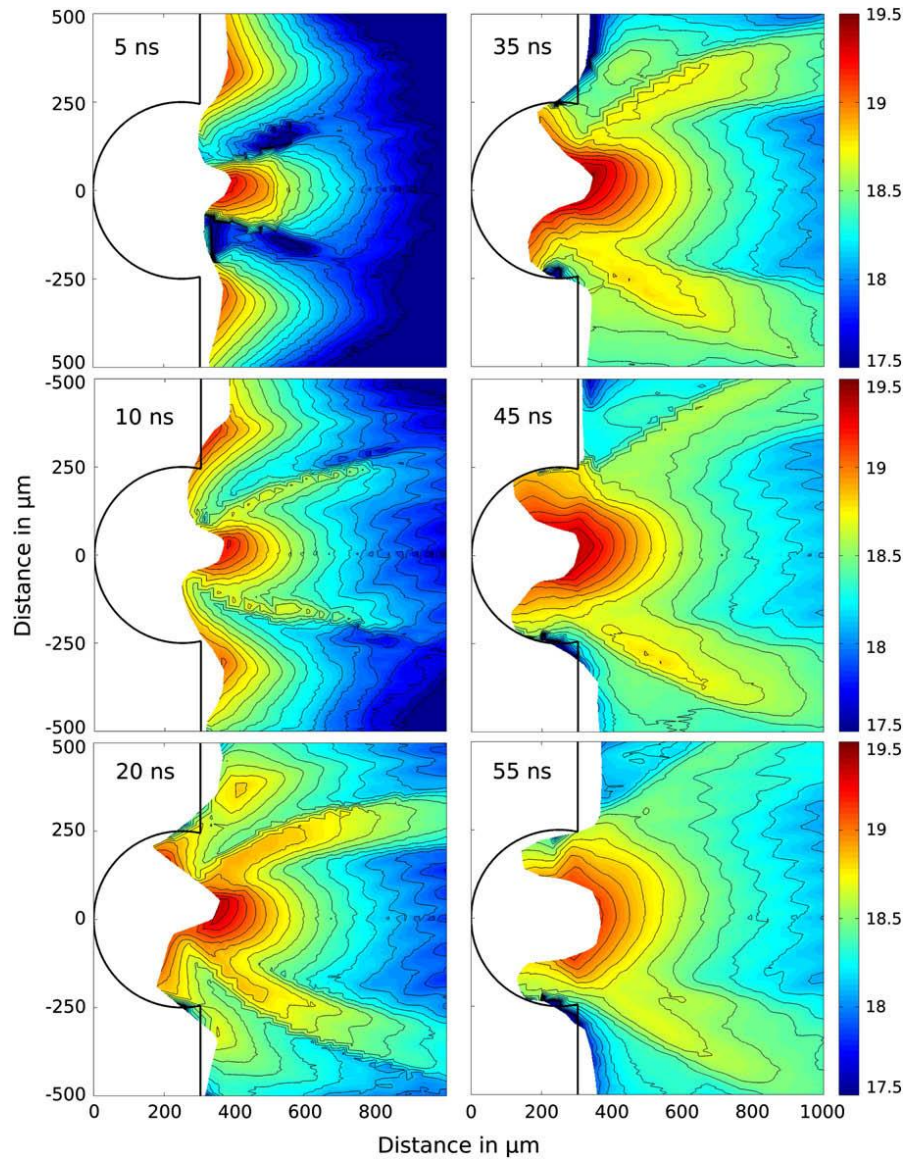


Figure 4.8. Electron density maps obtained from the interferograms of Figure 4.6. The density scale is logarithmic.

Figure 4.9 shows interferograms and electron density maps of C plasmas, the lightest material probed. A significantly faster plasma evolution is observed in which the shock fronts are already straight in the 5 ns frame. For the heavier materials, Al, Cu and Ag, the shock fronts are

first observed to be straight at 35, 50 and 75 ns, respectively. The absence of significant radiation cooling contributes to the disproportionately faster evolution of the C plasma.

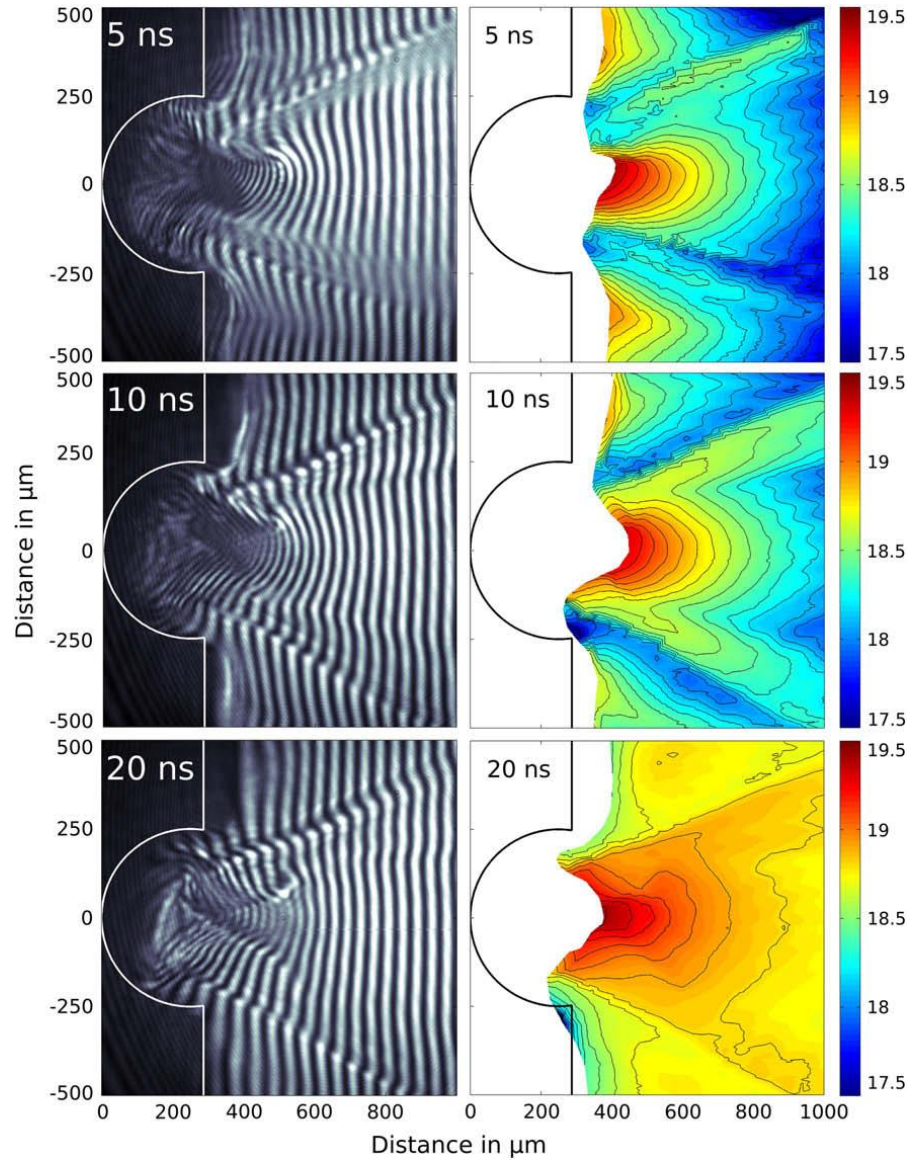


Figure 4.9. Sequence of interferograms and electron density maps for C plasmas. The main difference with the copper plasmas is the faster evolution of the lighter carbon atoms.

4.4.2. Simulations and discussion

The plasmas were modeled in two dimensions using the three dimensional single fluid radiation hydrodynamics code HYDRA [11]. HYDRA is an Arbitrarily Lagrangian Eulerian code capable of running in an assortment of hydrodynamic mesh strategies to avoid the mesh tangling that commonly occurs when modeling a converging plasma. Inverse Bremsstrahlung absorption was assumed to be the dominant laser deposition mechanism at our irradiation conditions. The equation of state was modeled using the Lawrence Livermore National Laboratory's LEOS library [12]. Radiation transport within the plasma was treated using multi-group diffusion techniques with 100 bins spanning photon energies between 1 and 3 KeV. Heat conduction was simulated using the conductivities of Lee and More [13]. The electron flux limiter was set to a value of 0.05 though, at our relatively small laser fluxes, this parameter is not critical.

Simulated electron density maps of the copper plasma are shown in Figure 4.10. The density distribution in the focal region is in very good agreement with the density build up seen in the soft x-ray interferometer maps. However, the opacities used in HYDRA are not accurate for the plasma conditions in the shock. Best agreement with the experiment is observed when radiation is turned off at 1 ns. In this case, the simulations reproduce well the plasma evolution including the density within the shock region ($\sim 6 \times 10^{18} \text{ cm}^{-3}$ for Cu at 20 ns after the laser irradiation).

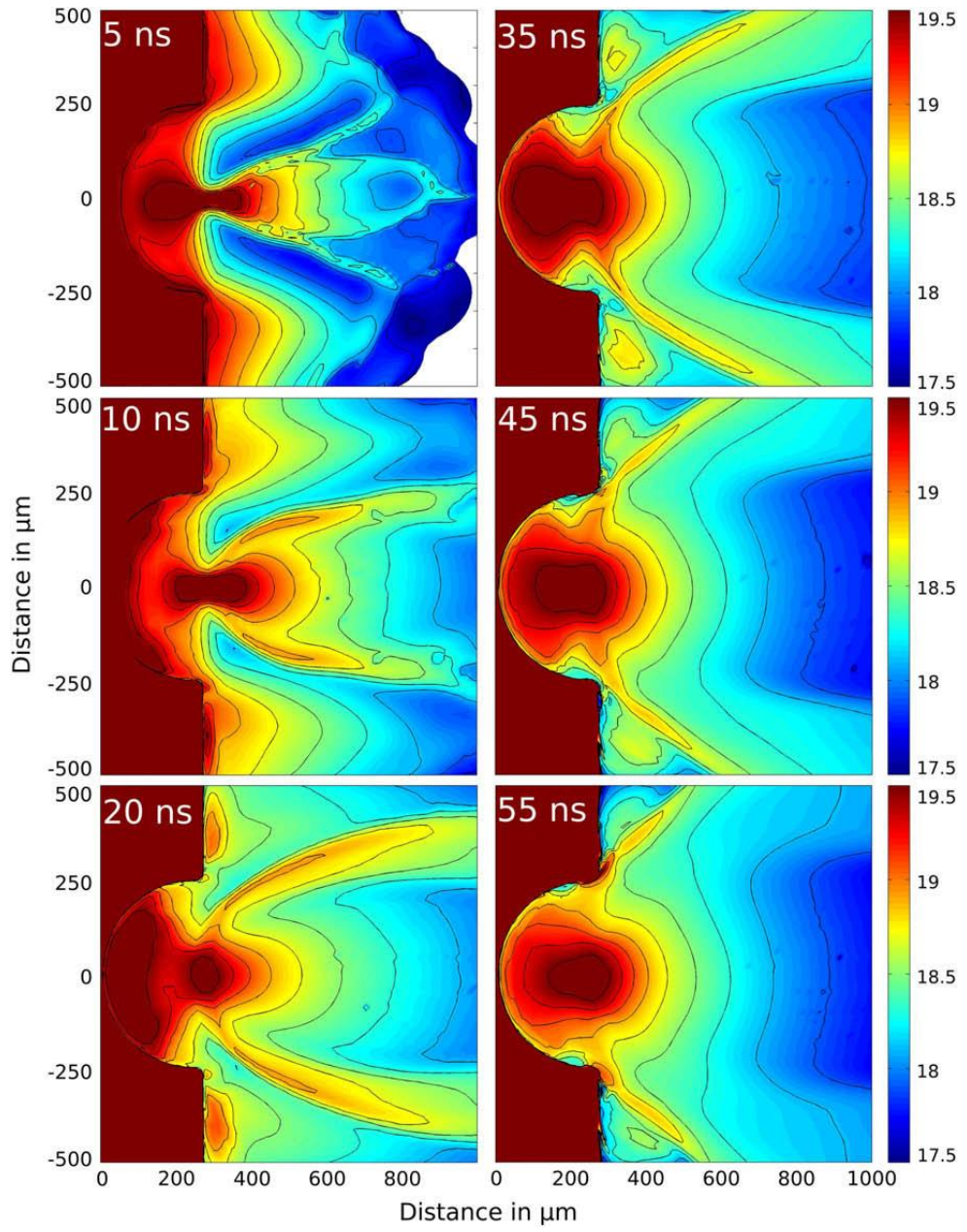


Figure 4.10. Simulated electron density maps from the code HYDRA.

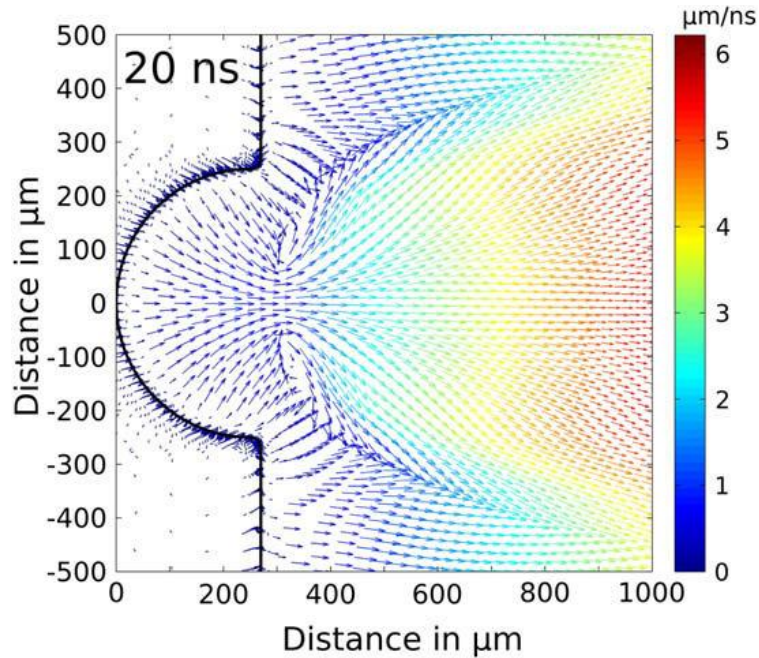


Figure 4.11. Velocity vector field map at 20 ns in the evolution of the copper plasma. The arrow colors assist in visualizing the magnitude of the velocity.

The origin of the shock formation is well illustrated by the computed map of plasma velocity vectors shown in Figure 4.11. The shock arises when the plasma that originated from the groove, after having converged on axis, expands and collides with the plasma that originated from ablation of the flat target wall surrounding the groove. The collision redirects the velocity of the side plasma to follow the contour of the central expanding plasma producing a localized increase in plasma density, temperature and degree of ionization. The continuous arrival of material creates a quasi-stationary shock wave [14]. Temperature and mean degree of ionization distribution maps of the Cu plasma at 20 ns in its evolution were also computed. The maps show that in the shocked region the electron temperature increases by about 50 percent (~ 4 eV) and that the degree of ionization also increases. Computation of the ion-ion collision mean-free path following Braginskii [15] gives a value always less than 1 mm, significantly smaller than the width of the shock, an indication that this is a collisional shock.

Simulations for the Cu plasma show that when the flat wall surrounding the semi-cylindrical groove is not directly irradiated by the laser or by the plasma self-emission the arc-shaped shock does not develop. The shock is strongest when both types of irradiation are present. Simulations show that in the case of the heavier targets plasma radiation plays a role in ablating the front wall material, which contributes to the shock formation. In contrast, simulations performed for lower element targets (such as C plasmas) reveal that radiation does not contribute to the ablation of the front wall. In any case, it is the continued ablation of the wall by either radiation or heat conduction that sustains the shocks for several tens of nanoseconds.

Comparison of the evolution of plasmas from the different materials shows that the main difference between them is the slower dynamics of the heavier element plasmas, resulting from their larger mass. Simulations for C and Cu plasmas show that close to the target wall the initial temperatures and pressures are similar, but the difference in mass causes the C plasma to evolve more rapidly. For C the shock is first seen to form a few ns after laser irradiation and to reach its peak electron density at 10 ns. The computed temperatures at 5 ns and 10 ns are 14 eV and 5 eV and the degrees of ionization are $\langle Z \rangle \sim 4$ and $\langle Z \rangle \sim 2.5$, respectively. In contrast, the Cu shock is observed to develop later, and to reach its peak density at ~ 35 ns where the electron temperature is 6 eV and the degree of ionization is $\langle Z \rangle \sim 4$. The peak temperature, 15 eV, occurs at 8 ns when the degree of ionization is $\langle Z \rangle \sim 8$. The slower evolution of the plasma corresponding to the heavier target materials was observed to result in increased shock lifetimes: ~ 40 ns for C, ~ 50 ns for Al, ~ 70 ns for Cu and ~ 90 ns for Ag.

4.5. Conclusions

The dynamics of plasma collisions and shock generation created by short pulse (120 ps) laser irradiation ($I \sim 1 \times 10^{12} \text{ Wcm}^{-2}$) of semi-cylindrical cavities machined into flat Al and Cu targets were studied combining visible and soft x-ray interferometry coupled with hydrodynamic simulations. Measured and computed electron density maps agree well in describing the evolution of the plasma. The convergence of material ablated from the walls near the axis results in a plasma collision that creates a dense collisional plasma focus reaching an electron density of $\sim 1 \times 10^{20} \text{ cm}^{-3}$. Later in time, a quasi-stationary bow shock is observed to develop as a result of the collision between the expanding central plasma focus and plasma generated by ablation of the flat walls surrounding the semi-cylindrical cavity. This collisional shock in the copper plasmas reaches a peak measured electron density of $\sim 6 \times 10^{18} \text{ cm}^{-3}$ with an electron temperature of 6 eV and mean degree of ionization of $\langle Z \rangle \sim 4$. The bow shock is sustained for several tens of nanoseconds by the continuous arrival of plasma ablated from the target walls. The slower dynamics of the plasma corresponding to the heavier materials results in an increased lifetime of the shock.

4.6. References

[1] J. Lindl, "Development of the indirect-drive approach to inertial confinement fusion and the target physics basis for ignition and gain," *Physics of Plasmas*, vol. 2, no. 11, pp. 3933-4024, 1995.

[2] T. R. Dittrich, S. W. Haan, M. M. Marinak *et al.*, "Review of indirect-drive ignition design options for the National Ignition Facility." pp. 2164-2170.

- [3] M.E. Jones, D. Winske, S. R. Goldman *et al.*, "Modeling ion interpenetration, stagnation, and thermalization in colliding plasmas," *Physics of Plasmas*, vol. 3, no. 3, pp. 1096-1108, 1996.
- [4] D. Vignes, C. Mazelle, H. Rme *et al.*, "The solar wind interaction with Mars: Locations and shapes of the Bow Shock and the magnetic pile-up boundary from the observations of the MAG/ER experiment onboard Mars Global Surveyor," *Geophysics Research Letters*, vol. 27, no. 1, pp. 49-52, 2000.
- [5] P. Hartigan, J. Raymond, and L. Hartmann, "Radiative bow shock models of Herbig-Haro objects," *Journal Name: Astrophys. J.; (United States); Journal Volume: 316*, pp. Medium: X; Size: Pages: 323-348, 1987.
- [6] A. R. Bell, P. Choi, A. E. Dangor *et al.*, "Collisionless shock in a laser-produced ablating plasma," *Physical Review A*, vol. 38, no. Copyright (C) 2009 The American Physical Society, pp. 1363, 1988.
- [7] Goodfellow. "material specification (online at www.goodfellow.com)."
- [8] J. Filevich, J. J. Rocca, M. C. Marconi *et al.*, "Observation of a multiply ionized plasma with index of refraction greater than one," *Phys. Rev. Lett.*, vol. 94, no. 035005, 2005.
- [9] S. I. Braginskii, "Transport Processes in a Plasma," *Reviews of Plasma Physics*, vol. 1, pp. 205, 1965.
- [10] P.W. Rambo, and R.J. Procassini, "A comparison of kinetic and multifluid simulations of laser-produced colliding plasmas," *Phys. Plasmas*, vol. 2, no. 8, pp. 3130-3145, 1995.
- [11] M. M. Marinak, G. D. Kerbel, N. A. Gentile *et al.*, "Three-dimensional HYDRA simulations of National Ignition Facility targets." pp. 2275-2280.
- [12] D. Young, E. Corey, "Release of new LEOS equation of state library," *Lawrence Livermore National Laboratory unpublished memo*, 1998.

- [13] Y.T. Lee, and R. M. More, *Phys. Fluids*, vol. 27, pp. 1273, 1984.
- [14] V. A. Gribkov, Oleg N Krokhin,, V. Ya Nikulin,, O. G. Semenov,, G. V. Sklizkov, “Experimental investigation of nonspherical cumulative laser plasma configurations,” *Soviet Journal of Quantum Electronics*, vol. 5, no. 5, pp. 530-537, 1975.
- [15] S. I. Braginskii, *Transport processes in a plasma*, 1965.

Chapter 5. Dynamics of a dense laboratory plasma jets investigated using soft x-ray laser interferometry

5.1. Plasma jets generated from v-shaped cavities

5.1.1. Introduction

Understanding the formation and evolution of plasma jets is of significant interest in various fields. In the astrophysical context, highly collimated jets are observed to originate from active nuclei galaxies [1] and young stellar objects [2], with parameters that cover many orders of magnitude in velocity and spatial extent. Numerous observations have been reported [3-4] and their dynamics have been modeled with numerical simulations [5-6]. Laboratory experiments can produce small scale plasma jets and shocks [7-13], some of which are relevant to astrophysics [14-17]. These experiments also give insight on jets and shock physics. For example, unwanted shock waves through inertial confinement fusion capsule defects can produce jets of material that mix ablator with fuel, resulting in a reduced yield [7, 10-11].

Numerical models of plasma jets are complex codes that take into account hydrodynamic and atomic processes, including the transport of radiation. In order to validate the models, experiments can be designed to create plasma jets with different characteristics, including scaled versions of astrophysical jets [18]. High Mach number jets were experimentally produced and studied using Z-pinch arrays [14]. Highly radiative jets have also been created using high energy ($\sim 0.1 - 1$ kJ) laser pulses from large lasers such as the Nova [15], Gekko XII [16], Omega [7],

and PALS Asterix [12-13] to irradiate conical and flat targets. Plasma jets have also been produced by irradiation of different target geometries using smaller lasers ($\sim 10 - 15$ J) [9, 19]. While imaging, spectroscopy and other techniques have been used to study the behavior of plasma jets [7, 9, 16], accurate two-dimensional maps of the electron density can only be directly obtained with interferometry. Interferometry with visible and ultraviolet light has been extensively used to study a wide variety of plasmas [20]. However, the use of optical interferometry is limited by the strong refraction caused by large density gradients. Also limiting is the increased number of fringe shifts resulting from large plasma densities and size, which cannot be resolved. It is possible to overcome these limitations with the use of short wavelength laser probes. Soft x-ray light can propagate through plasmas that have steeper density gradients and larger size, with significantly reduced refraction and with a smaller number of fringe shifts, permitting the measurement of higher densities. This has motivated the development of soft x-ray laser interferometry as a tool to probe dense plasmas [21-31]. In particular, Wan *et al.* used a 15.5 nm wavelength soft x-ray laser probe to obtain interferograms of plasmas created by focusing the fusion-class laser NOVA at an intensity of 3×10^{14} W.cm⁻² onto two Au slab targets placed at 45 degree with respect to the symmetry plane [22]. Plasma density profiles were measured to reach an electron density of 6×10^{20} cm⁻³ on axis. Hydrodynamic simulations using the code LASNEX predicted a stagnation width similar to that observed in the experiment. However, the code predicted the appearance of an off-axis electron density peak as soon as the plasma started to collide, a feature that was not observed experimentally. In this chapter we present the study of a dense hydrodynamic plasma jet created by irradiation of a triangular V-shaped cavity with low energy laser pulses (< 1 J). The formation and evolution of the jet was studied combining soft x-ray laser interferometry and emission spectroscopy with 2D hydrodynamic simulations. The target geometry differs from that investigated by Wan *et al.* in that the wall of the cavity wall is continuous, without an opening at the vertex. The plasma originating from the vertex was found

to initiate the formation of a thin and long plasma sheet that is augmented by the convergence of wall plasma on the symmetry plane of the target, where it is redirected outward.

The experimental setup and target configuration used for this experiment is discussed in Chapter 3. The next section presents the experimental results. They are compared to hydrodynamic simulations in section 5.3.

5.1.2. Experimental results

A time integrated image of the plasma self-emission at wavelengths $\lambda < 1000 \text{ \AA}$ is shown in Figure 5.1. The irradiating laser beam is incident on the target from the right. Most of the emission originates from a thin ($50 \text{ }\mu\text{m}$ wide) elongated plasma sheet (1 mm long) localized along the symmetry plane of the groove. Weaker emission is also observed from plasma near the wall.

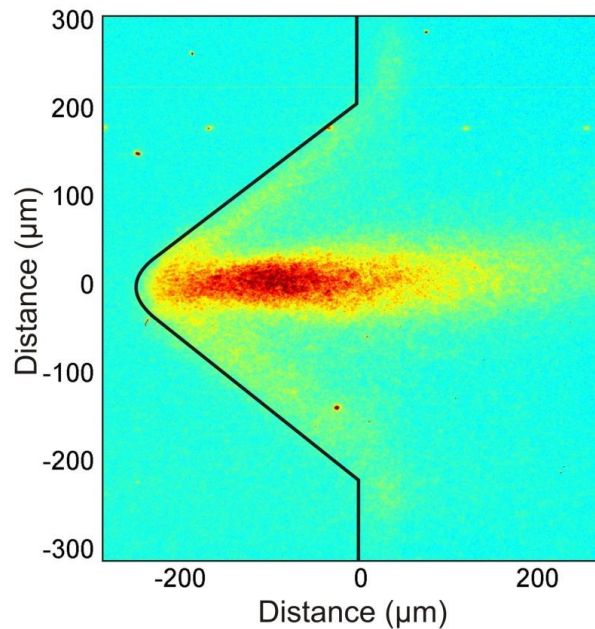


Figure 5.1. Time integrated emission of the laser-created aluminum plasma jet.

A sequence of interferograms that maps the evolution of these aluminum plasmas is shown in Figure 5.2. The timing of each image is measured with respect to the arrival of the 120 ps heating pulse. The white lines outline the original position of the target, obtained for each shot from a preceding reference interferogram without the plasma present. Electron density maps were calculated from the interferograms by assuming that the 1 mm plasma is uniform along the propagation direction of the probe beam. The plasma is initially uniform in this direction because the 1.5 mm FWHM plasma heating beam overfills the 1 mm long target. When analyzing the resulting interferograms, the number of fringe shifts is directly proportional to the electron density, with $N_{fringe} = \frac{L n_e}{\lambda 2n_c}$ for $n_e \ll n_c$, where n_c is the critical density ($5 \times 10^{23} \text{ cm}^{-3}$ at 46.9 nm) and L is the length of the plasma (1 mm). One fringe shift at this probe wavelength corresponds to a density of $5 \times 10^{19} \text{ cm}^{-3}$. Therefore a map of the electron density can be constructed by measuring the number of fringe shifts with respect to a reference interferogram obtained without plasma present. The error in determining the number of fringe shifts is estimated to be $\sim 1/10^{\text{th}}$ of a fringe shift, which amounts to an uncertainty of $5 \times 10^{18} \text{ cm}^{-3}$ in the density values. Additional uncertainty of similar magnitude results from shot-to-shot variations. The aforementioned analysis of the interferograms also assumes that the plasma index of refraction is dominated by the contribution from free electrons. This is not always the case at soft x-ray wavelengths, as bound electrons can significantly contribute to the index of refraction [32]. However, calculations showed that in the case of aluminum plasmas the contribution of bound electrons to the index of refraction can be neglected at the 46.9 nm probe wavelength.

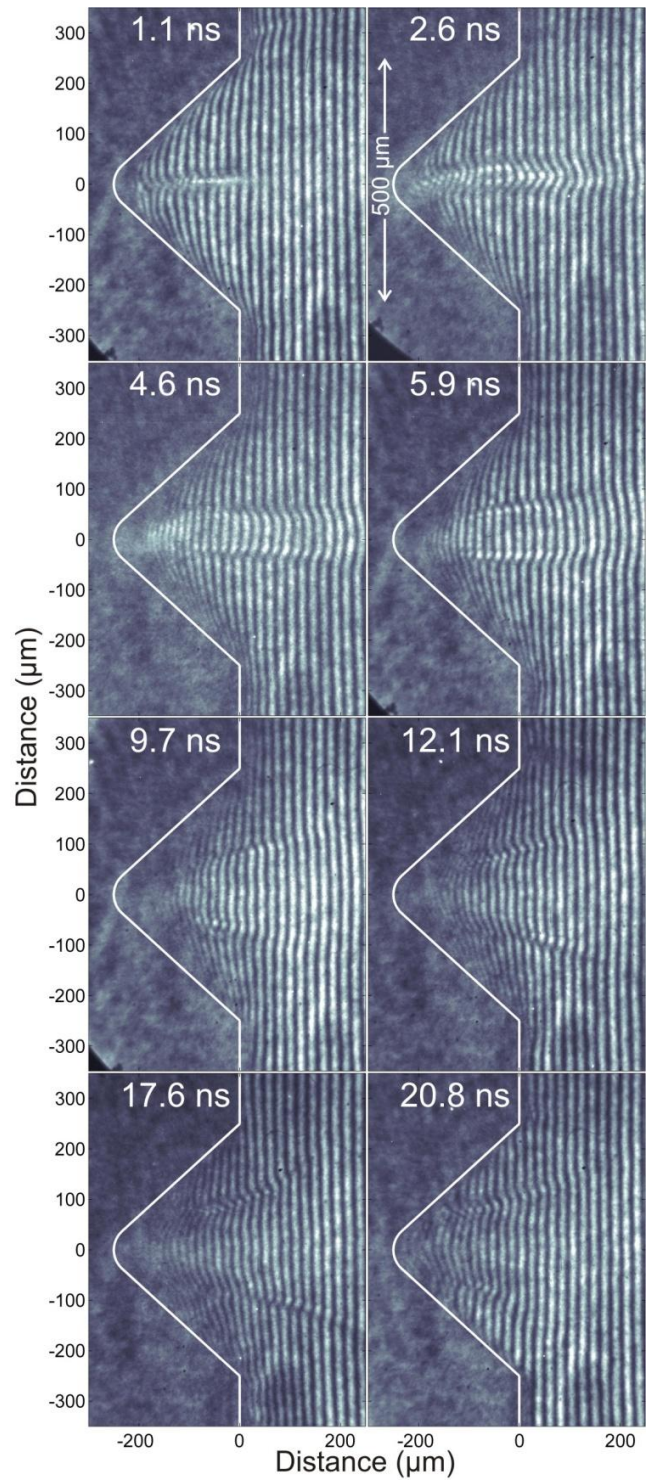


Figure 5.2. Sequence of soft x-ray interferograms mapping the evolution of laser-created aluminum plasma. The white solid line represents the original position of the V-shaped groove. The timing is measured with respect to the peak of the heating pulse.

Fig. 5.3 shows the electron density maps corresponding to the interferograms of Fig. 5.2. The 1.1 ns frame shows the formation of a narrow ($\sim 30 \mu\text{m}$ wide) plasma jet with a large length to width ratio, $\sim 10:1$ along the symmetry plane of the groove. The jet was measured to initially expand at a velocity of $\sim (3\pm 1) \times 10^7 \text{ cm s}^{-1}$ along the symmetry plane. At this time the interference fringes within the region of the jet are not completely resolved due to a combination of refraction of the probe beam by steep density gradients and motion blurring. The subsequent frame at 2.6 ns shows that the plasma continues to expand rapidly along the symmetry plane, reaching a length of $\sim 530 \mu\text{m}$ while simultaneously broadening to a plume $\sim 80 \mu\text{m}$ wide. At this time the highest electron density measured along the symmetry plane reaches $1.2 \times 10^{20} \text{ cm}^{-3}$ at $\sim 100 \mu\text{m}$ away from the bottom of the cavity. At later times, the central plasma continues to expand along the symmetry plane, while simultaneously widening to reach a width of $\sim 200 \mu\text{m}$, 9.7 ns after the irradiation pulse. The 9.7 ns density map and the subsequent frames show the formation of two dense side lobes that evolve moving slowly away from the symmetry plane of the groove toward the target walls. At these late times the regions close to the target surface present strong absorption, caused by the presence of a large density of low charge ions which can be photoionized by the 26.5 eV photons of the probe beam. In summary, during the first nanosecond of the evolution, a dense thin elongated jet-like plasma sheet is observed on axis. This jet extends quickly along the symmetry plane. Later in time, the jet widens into a plume that then splits into two distinct side lobes, progressively evolving towards the target walls.

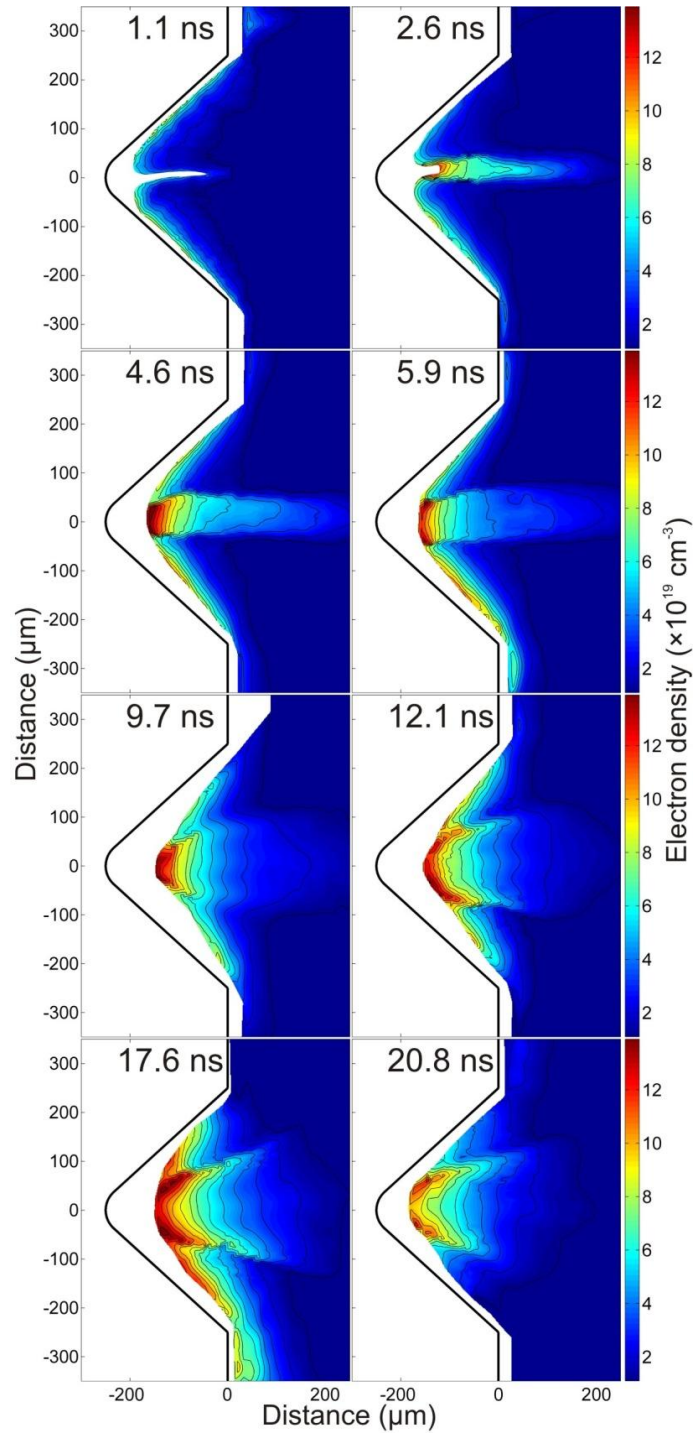


Figure 5.3. Electron density maps corresponding to the interferograms of Figure 5.2. The black solid line outlines the position of the groove. The white regions are locations where the plasma density could not be determined either due to fast plasma motion resulting in blurred fringes (near the symmetry axis), or due to strong absorption of the soft x-ray probe beam by cold plasma (near the walls).

5.1.3. Simulations and discussion

In order to help understand the jet formation and subsequent plasma evolution as well as test the ability to accurately simulate the plasma, 2D computations were performed using the single fluid radiation hydrodynamics code HYDRA [33-34]. HYDRA was set to use an Arbitrary Lagrangian Eulerian mesh that allows for mass advection, the Quotidian Equation Of State (QEOS) [35] and conductivity from Lee and More [36]. The laser energy deposition mechanism at the relatively low irradiation intensities used in this experiment is assumed to be inverse Bremsstrahlung absorption. Radiation transport was treated with multi-group radiation diffusion techniques and tabulated opacities. The temporal profile of the laser pulse was approximated by a 120 ps FWHM Gaussian function that closely mimics the experimental pulse.

Figure 5.4 shows simulated electron density maps for the times corresponding to the measured electron density distributions in Figure 5.3. The simulations reproduce well the evolution of the plasma jet. The electron density at 2.6 ns is computed to reach $1.4 \times 10^{20} \text{ cm}^{-3}$ near the bottom of the target, in agreement with the measurements. As in the experiment, side lobes are observed to form and separate later in the plasma evolution, with peak electron density values similar to those measured ($1-1.3 \times 10^{20} \text{ cm}^{-3}$). The jet expansion velocity simulated by HYDRA is well matched with the experimental measurement, and the code predicts a maximum Mach number of ~ 5 . This good agreement between the HYDRA simulations and the experimental data was only achieved when taking into account radiation cooling of the plasma, as discussed later.

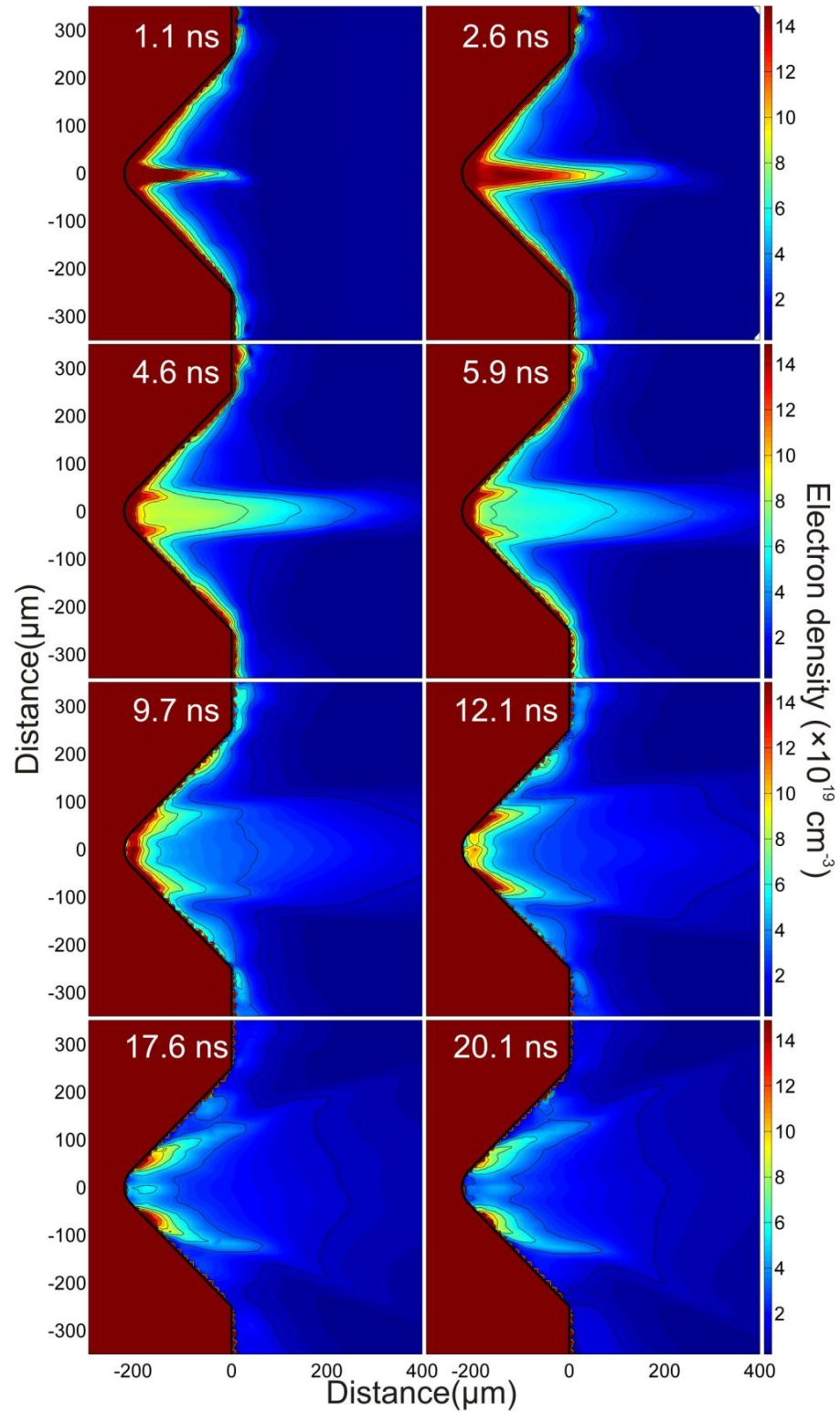


Figure 5.4. Simulated electron density maps obtained with HYDRA. The code shows good agreement with the measurements in the general behavior of the plasma and maximum electron densities.

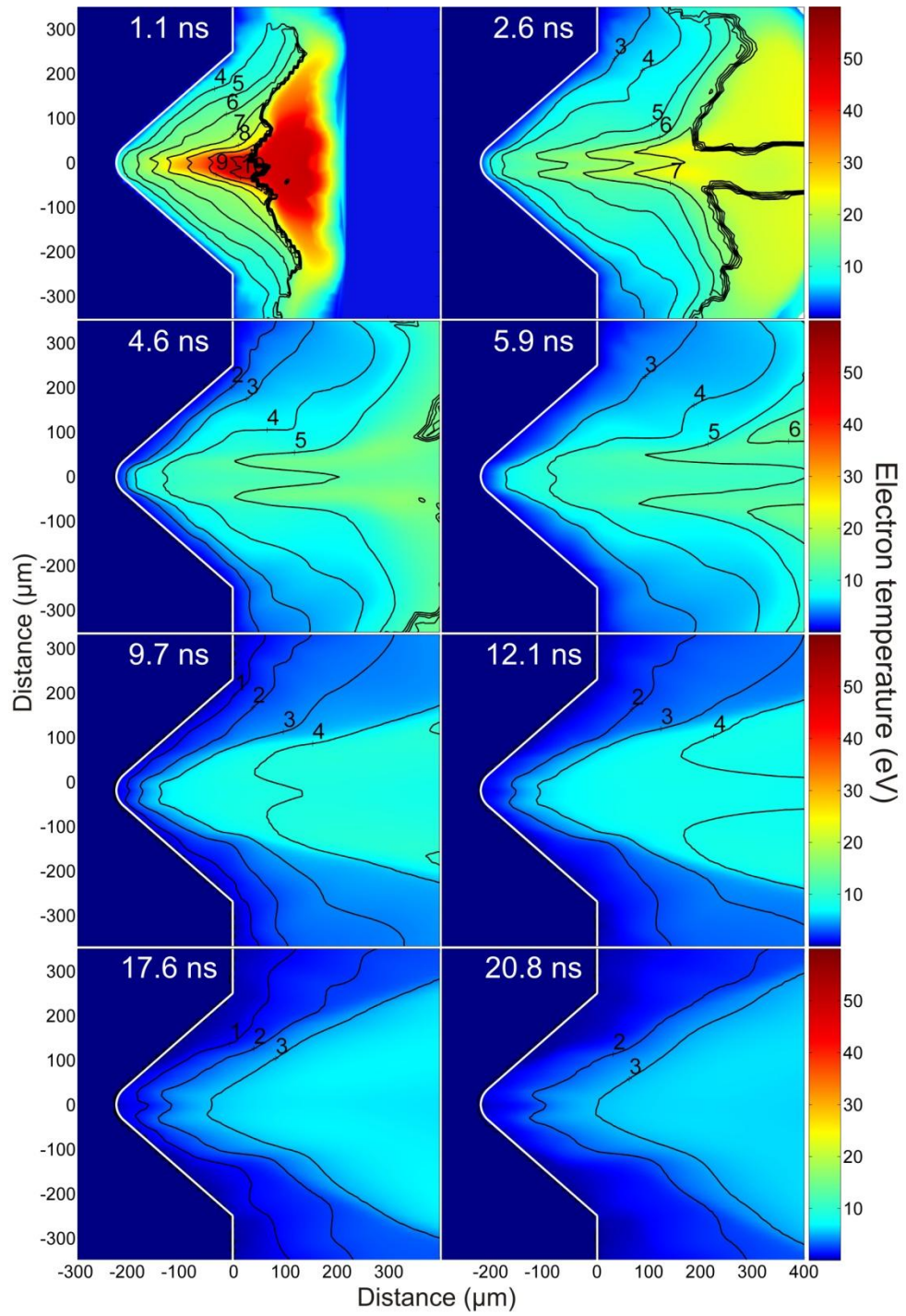


Figure 5.5. HYDRA simulated maps of the electron temperature T_e of the laser-created aluminum plasma. The black contour lines delimit regions of mean ionization Z_{mean} inside the plasma.

Figure 5.5 shows color maps of the computed electron temperature (T_e) with contours displaying the plasma mean degree of ionization (Z_{mean}). The simulations show that early in the evolution (~ 1 ns) the jet has a temperature of $T_e \sim 55$ eV and a high degree of ionization, $Z_{\text{mean}} = 7\text{--}10$. The presence of $Z = 10$ ions is confirmed by the time integrated soft x-ray spectrum presented in Figure 5.6, that spans wavelengths from 3.5 to 6.5 nm. Several lines in Al X and Al XI, which can be efficiently excited with an electron distribution defined by an electron temperature of ~ 50 eV, can be identified. Al XII transitions, whose excitation requires a significantly higher electron temperature, are not observed. These observations are consistent with the temperatures predicted by the code. The electron temperature maps also show that at times corresponding to more than 1 ns after the termination of the irradiation pulse the plasma distributed along the walls of the target is cold ($T_e < 15$ eV). At 2.6 ns the peak temperature drops to ~ 25 eV, and is associated with plasma that has moved to a location outside the cavity. The plasma side lobes that appear later in time have low temperatures of less than 10 eV and low degree of ionization, $Z_{\text{mean}} < 4$.

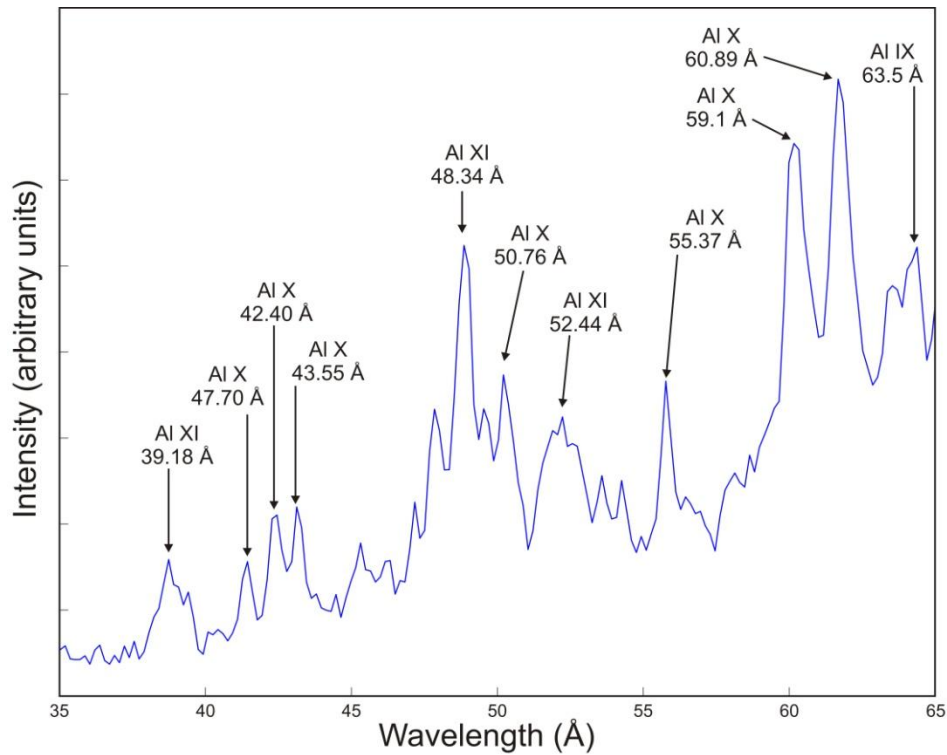


Figure 5.6. Time integrated aluminum spectra in the region between 3.5 and 7.5 nm.

The computed pressure maps of Figure 5.7 show that a high pressure region forms at the bottom of the groove, resulting from the rapid convergence of plasma from the walls (see 500 ps frame). This localized high pressure gradient accelerates the ablated material outward at a Mach number of ~ 5 . The interferograms show that at 1 ns this ablated material breaches the opening of the cavity as a plasma jet. At this time the highest pressures are located along the symmetry plane. These pressure gradients contribute to the progressive widening of the plasma plume.

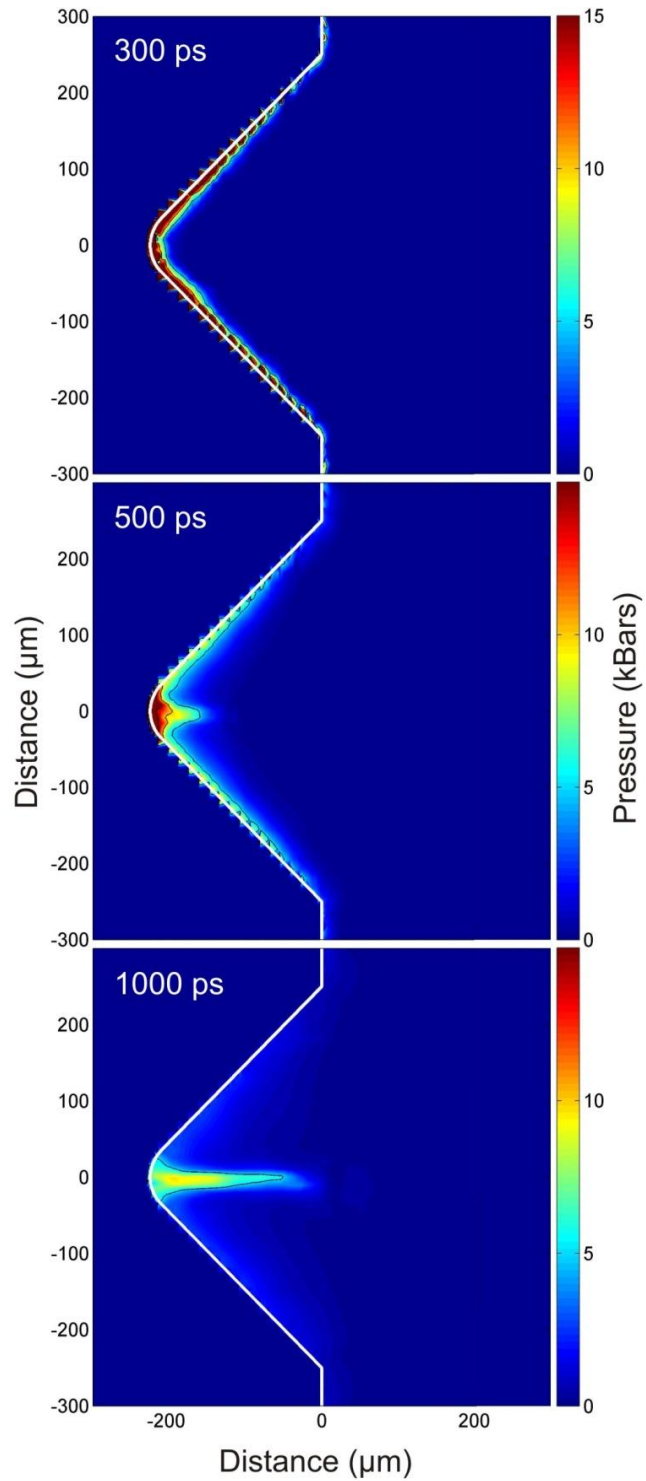


Figure 5.7. Computed plasma pressure distribution for different times measured respect to the onset of the irradiation pulse. The large pressure gradients that develop at the bottom of the groove during the irradiation accelerate the plasma that initially forms the plasma jet.

Radiation cooling has been previously identified as an important mechanism in the collimation of plasma jets [15-16]. Figure 5.8 illustrates the effect of radiation cooling in our plasma jet by comparing the simulated electron density with and without (optically thick) plasma radiation to the experimentally measured electron density maps. In the former case the radiation transport was computed using tabulated opacities generated using an average atom model at LLNL. The comparison shows that radiation plays a significant role in the experimentally observed jet collimation. For the plasma conditions of our experiment, line radiation dominates radiation loss rates. Dielectric recombination and photo recombination are weaker by about two orders of magnitude and bremsstrahlung radiation is even less intense. In the simulated optically thick case, the plasma is computed to be significantly hotter (80 eV at 1.1 ns) than in the radiatively cooled plasma (55 eV at 1.1 ns), that translate into a higher plasma pressure on axis. The higher pressure in the optically thick case results in a broader, less collimated jet, and in the premature formation of the plasma side lobes, in disagreement with the experiment. The relative importance of radiation in aiding jet collimation is usually evaluated through the cooling parameter χ defined as the ratio of the radiation cooling time to the characteristic hydrodynamic time $\chi = \tau_{RAD} / \tau_{HYDRO}$ [18]. The characteristic radiative cooling time is given by the total kinetic

plasma energy content divided by the radiative flux q_{RAD} : $\tau_{RAD} = \frac{3k(T_E n_E + T_I n_I)}{2 \cdot q_{RAD}}$, and the

characteristic hydrodynamic time $\tau_{HYDRO} = \frac{R_{jet}}{v_{jet}}$ is the ratio of the jet width to the jet lateral

expansion velocity. When $\chi < 1$, the jet is strongly radiative and is classified as a radiatively cooled jet.

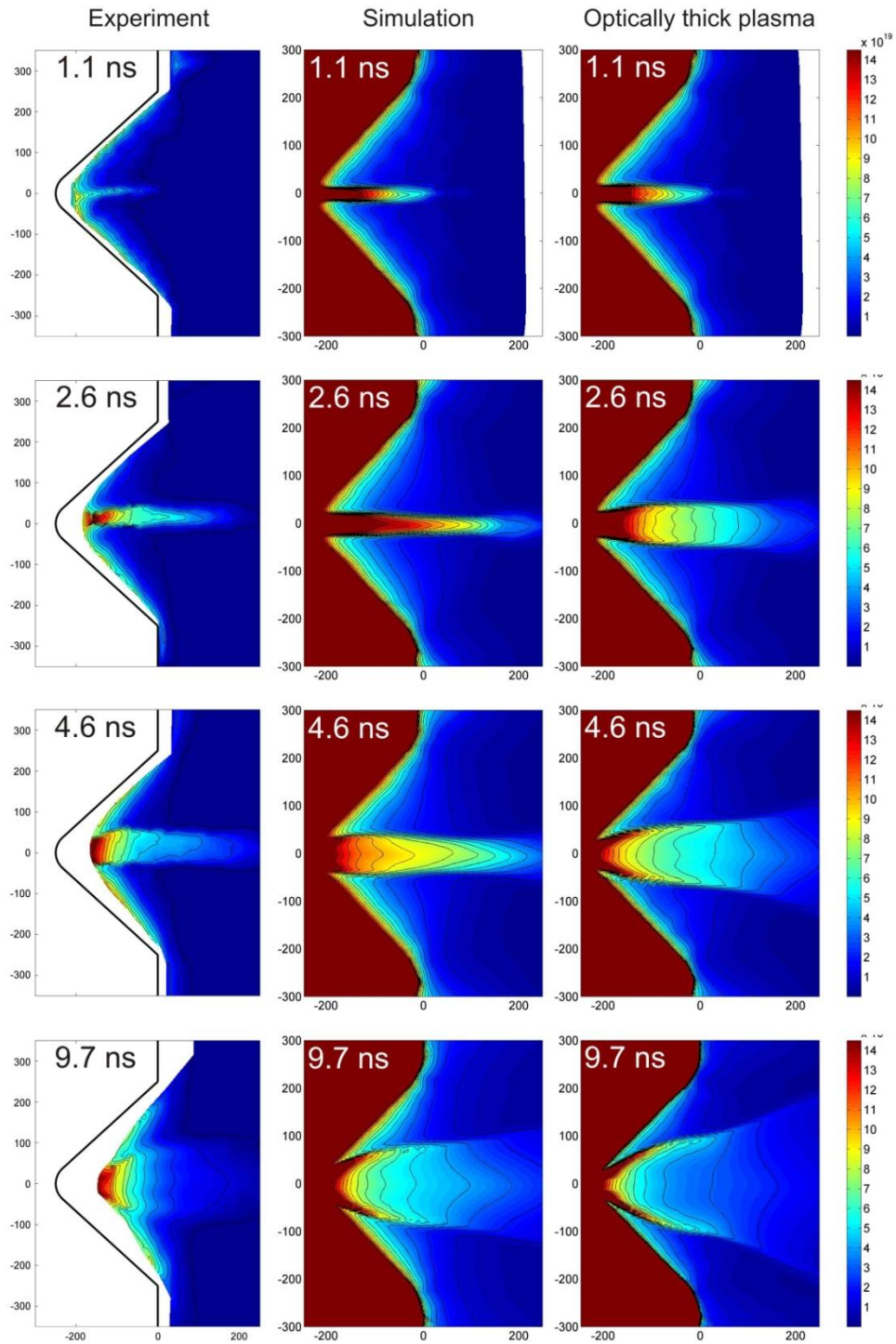


Figure 5.8. Comparison of Al plasma jet experimental data (left column) to HYDRA simulations with radiation transport (center column) and for an optically thick plasma (right column).

For the Al laboratory jet studied in our experiments, HYDRA simulation predicts $\tau_{RAD} \sim \tau_{HYDRO}$ during the first 2.5 ns of the evolution, corresponding to a radiative cooling parameter of $\chi \sim 1$. This classifies our jet as being in the coupled regime, where radiation cooling is comparable to adiabatic cooling. Simulations reveal that the role of radiation in cooling the jet decreases after the first 2.5 ns, when χ becomes increasingly larger than one and the jet is observed to undergo significant lateral expansion.

To better visualize the formation of the plasma jet and the subsequent development of the plasma side-lobes, tracer particle trajectory plots were generated from the velocity vector fields computed by HYDRA at 10 ps intervals. Figure 5.9 shows the trajectory of initially equally spaced particles ablated at times of 30, 140, and 250 ps with respect to the beginning of the 120 ps FWHM laser heating pulse. Each frame follows the tracer particles from the time they leave the surface up to 5 ns in the evolution. Each alternating color shade indicates an elapsed time of 500 ps. Figure 5.9 shows that mass ablated at different times during the laser heating pulse contributes differently to the formation of the jet. The frame corresponding to material ablated 30 ps after the initiation of the laser irradiation pulse reveals the successive arrival of plasma originating from the side walls to the symmetry plane. The trajectories are initially observed to be perpendicular to the target surface, as can be expected from the pressure gradients normal to the walls. The tracer particles with the highest velocities are those corresponding to the most intensely irradiated $\sim 150 \mu\text{m}$ wide central region of the target surface at the beginning of the laser pulse. These are the only tracer particles that reach the symmetry plane one nanosecond after the irradiation pulse. This is evidence that within the first nanosecond the plasma jet only contains material ablated from the $150 \mu\text{m}$ wide central region of the target. The 140 ps frame in Figure 5.9 shows that the material ablated later during the irradiation pulse has a reduced velocity. This is in particular the case of plasma emanating from the central region of the groove, which is

significantly slowed down by its encounter with downstream plasma created by mass ablated earlier during the irradiation pulse. This effect is even more evident in the 250 ps frame, corresponding to material ablated after the heating laser has deposited its energy, in which the mass ablated from the bottom of the groove is seen to expand only 70 μm along the symmetry plane within the first 5 ns.

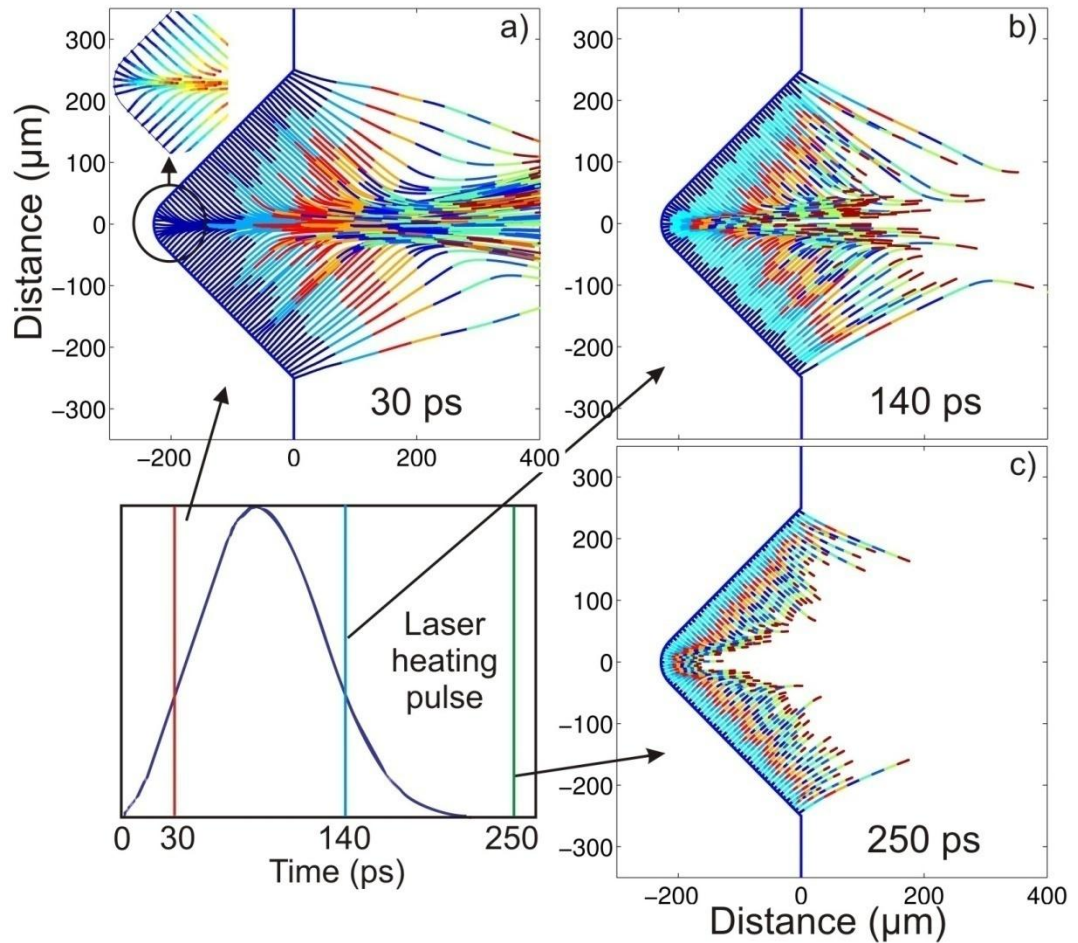


Figure 5.9. HYDRA simulations of particles trajectories leaving the target at different times during the laser heating pulse. The alternating colors represent 500 ps time steps and the complete trajectory spans 5ns.

The role of the target tip in the formation of the plasma jet was investigated by comparing the results with simulations of a target with a 150 μm wide opening at the bottom of the groove. It was found that without the vertex a jet-like plasma structure still forms as a result of the collision of plasma arriving from the walls at the symmetry plane, but this jet has a reduced density and velocity. Just like in the case including the tip, the sequential arrival on axis of plasma generated at the target walls contributes to increase the mass of the jet. Later in the evolution the dominant pressure in the jet, that is not counterbalanced by the momentum of plasma ablated from the side walls, causes it to widen. The collision of the expanding plasma jet with the plasma generated at the walls forms the observed plasma side-lobes.

Aside from the Mach number ($M \sim 5$) and cooling parameter ($\chi \sim 1$), the measurements and simulations allow the computation of other dimensionless parameters for comparison with other jets [18]. The ratio of jet density to ambient medium (the latter taken here as the density of the plasma surrounding the jet) is $\eta = \rho_{jet} / \rho_{amb} > 10^2$. The Reynolds number $R_e = R_{jet} v_{jet} / \nu \sim 4 \times 10^5$ and Peclet number $P_e = R_{jet} v_{jet} / \kappa \sim 10$ at 1.1 ns were computed using Spitzer's kinematic viscosity ν and kinematic thermal diffusivity κ . This means that both viscous drag and thermal conduction can be neglected compared with inertial forces and the advection of kinetic energy. The ion-ion collision mean free path is computed to be $\lambda_{mfp} < 1 \mu\text{m}$, significantly shorter than the plasma lateral dimension, R_{jet} , resulting in a localization parameter $\delta = \lambda_{mfp} / R_{jet} < 10^{-2}$ corresponding to a highly collisional plasma. This high degree of collisionality allows the plasma to be simulated with a hydrodynamic code.

5.2. Generation of dense plasma jets from irradiation of conical cavities

In this section, the generation of dense plasma jets by irradiating conical copper targets with low energy (1 J) short duration (220 ps FWHM) pulses from a table-top Titanium Sapphire laser system at an intensity of $6 \times 10^{12} \text{ W cm}^{-2}$ is presented. The jet evolution was recorded using soft x-ray laser interferometry. The measured electron density reached values as high as $1.5 \times 10^{21} \text{ cm}^{-3}$, an order of magnitude larger than our previously measured planar plasma jets. The results show that very dense plasma jets can be generated and studied using relatively low laser energy pulses. Two dimensional simulations performed with the hydrodynamic code HYDRA confirm that such high densities can be obtained, and agree in describing the overall jets evolution. Radiation cooling of the plasma at early times was found to play an important role in the formation of the collimated and highly collisional dense plasma plumes.

5.2.1. Experimental setup

The experimental setup used is described in Chapter 3. The plasma jets were created by laser irradiation of conically shaped copper targets. The target cones were punched on a 99.9% copper slab 1 mm wide and 50 mm in height (see Chapter 3). The angle of the cones was ~ 90 degrees and the diameter of the opening at the target surface was $600 \pm 20 \text{ }\mu\text{m}$. The tip of the cone was measured to have a radius of curvature smaller than $150 \text{ }\mu\text{m}$. The features on the inside surface of the cone were estimated to be less than $10 \text{ }\mu\text{m}$ by inspection under an optical microscope.

Interferograms of the plasma were recorded at different times during the jet evolution using the setup described in Chapter 3. Two dimensional electron density maps were generated

from the interferograms using the Analytical Spline Abel Inversion (ASAI) numerical technique [37] (see Chapter 3).

5.2.2. Experimental results and discussion

A sequence of soft x-ray interferograms describing the plasma jet evolution is presented in Figure 5.10. The time corresponding to each frame is defined as the time interval between the peak of the heating laser pulse and the peak of the probe pulse. The white line represents the initial position of the front surface of the target, obtained from a reference interferogram with no plasma present. The heating laser pulse is incident from the right onto the target, concentric with the symmetry axis of the cone. Significant fringe shifts are observed outside the conical cavity, indicating the presence of a dense plasma. Absorption of the $\lambda=46.9$ nm probe beam by the presence of a dense cold plasma prevented measurements in the ~ 100 μm region closest to the target at practically all times. Two dimensional electron density maps extracted from the interferograms are presented in Figure 5.11. Isodensity contour lines are plotted on the maps for densities of 1×10^{20} , 3×10^{20} and 1×10^{21} cm^{-3} . The uncertainty in measuring the fringe shift was determined to be less than 5% of a fringe shift. A narrow dense plasma jet of 50 – 80 μm length is observed to exit the cone along the symmetry axis at about 3 ns after laser irradiation. Subsequently this plasma jet continues its axial expansion at a velocity of ~ 10 $\text{cm } \mu\text{s}^{-1}$, while retaining a small radius and high density, as seen in the 4 ns frame. At 5.5 ns after the arrival of the laser heating pulse, the plasma plume extends ~ 700 μm away from the bottom of the conical cavity. At this time the jet has a density of $n_e > 1.5 \times 10^{21}$ cm^{-3} on axis, and is relatively narrow with a width of ~ 100 μm measured 200 μm away from the target surface at the 10^{20} cm^{-3} isodensity contour. At later times the plasma evolves into a broader plume, which width

increases from $\sim 120 \mu\text{m}$ at 7 ns to $\sim 220 \mu\text{m}$ at 10 ns. The measured electron densities at that time remain high ($n_e > 1 \times 10^{20} \text{ cm}^{-3}$).

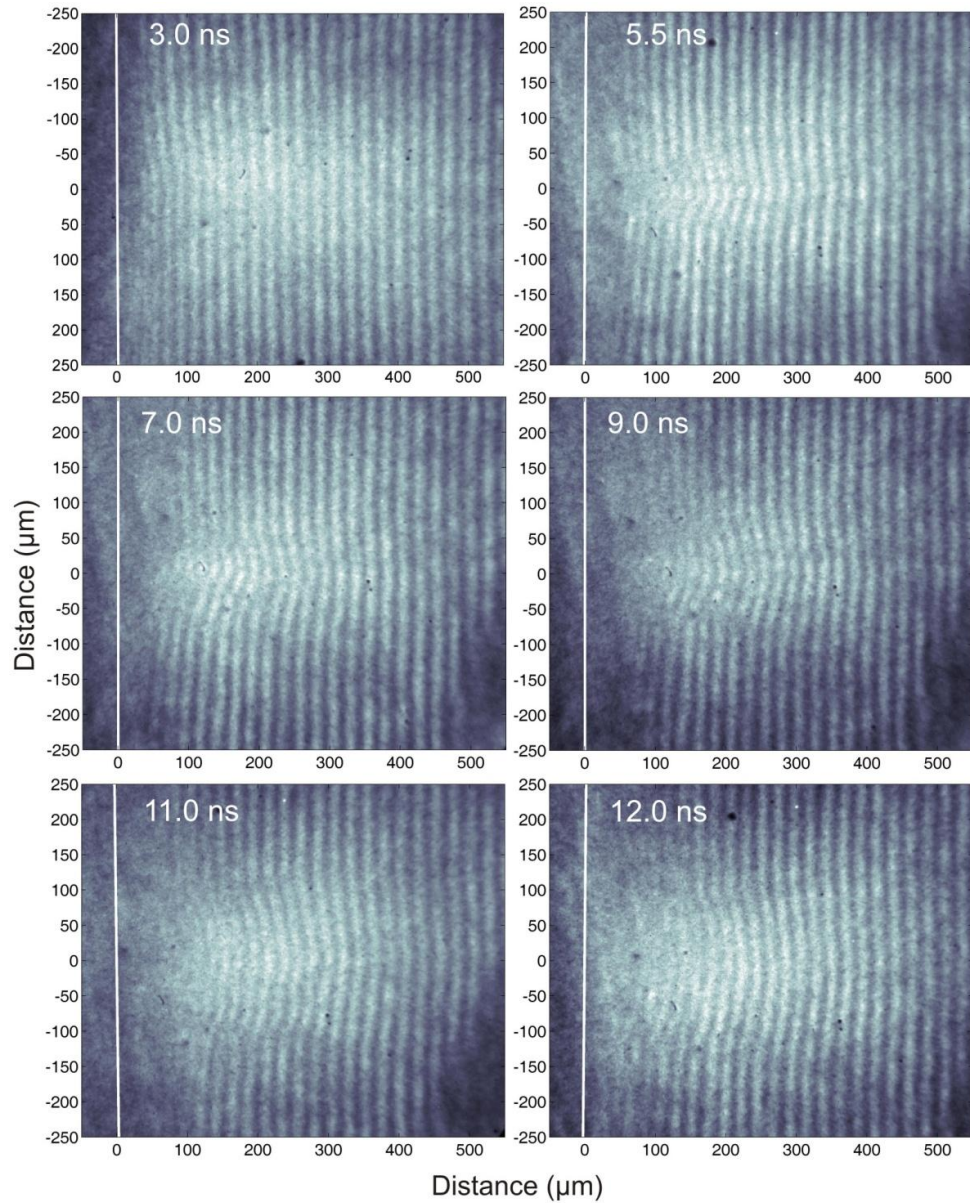


Figure 5.10. Sequence of interferograms describing the evolution of the laser-created plasma jet. The white line represents the position of the target surface. The time is measured respect to the peak of the laser irradiation pulse.

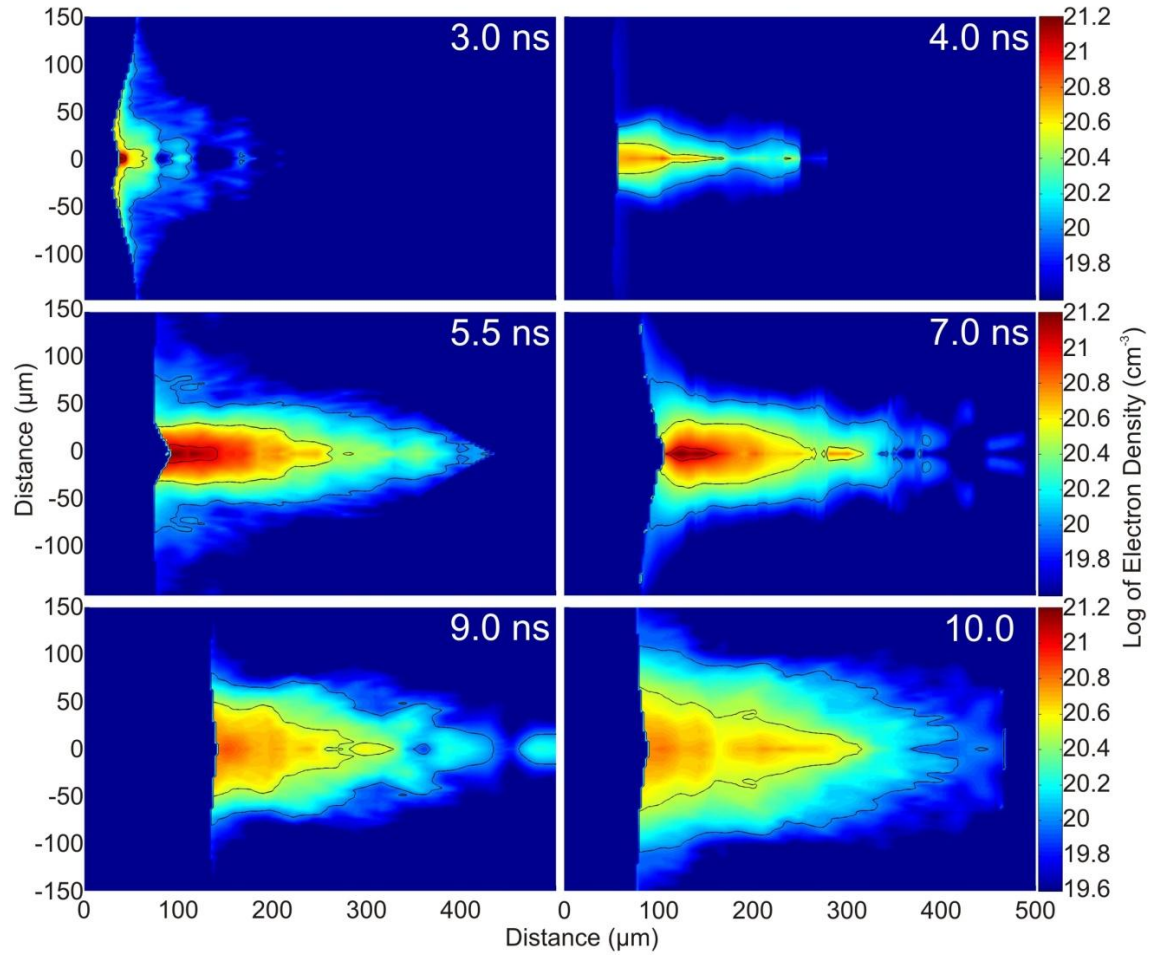


Figure 5.11. Two dimensional electron density maps of the laser-created plasma jets obtained from the interferograms using numerical Abel inversion. Black isodensity lines follow density contours at 1×10^{20} , 3×10^{20} and 1×10^{21} cm^{-3} .

Two dimensional simulations were performed using the single fluid radiation hydrodynamic code HYDRA [34]. Simulations were conducted using the Livermore Equation of State (LEOS) [38], and conductivities from Lee and More [36]. Laser energy is deposited through Bremsstrahlung absorption. The temporal profile of the heating laser pulse was measured experimentally and used in the simulation. Radiation transport was treated with multi-group radiation diffusion techniques utilizing opacities computed assuming local thermodynamic

equilibrium. To perform two-dimensional simulation an Arbitrary Lagrangian Eulerian mesh was used to simulate a 2 degree wedge from the conical target and resulting plasma. Thus the model results correspond to the ideal case of perfect cylindrical symmetry. Efforts were made experimentally to justify this approximation. However, the simulation did not include irregular features of the less than ideal target surface that can be expected to produce plasma at the cone walls which reach the axis at different times resulting in a weaker jet. Figure 5.12 shows simulated electron densities maps corresponding to the experimental conditions used to obtain the experimental data shown in Fig. 5.11. The simulation reproduces the general shape and behavior of the plasma jet and confirms that very high density plasma jets can be generated by relatively low energy laser irradiation of conical targets. Both simulation and experiment reveal jets with densities greater than $1 \times 10^{21} \text{ cm}^{-3}$ outside the cavity. The density is even higher in the simulations, probably a result of ideal irradiation and target conditions difficult to achieve in the experiment.

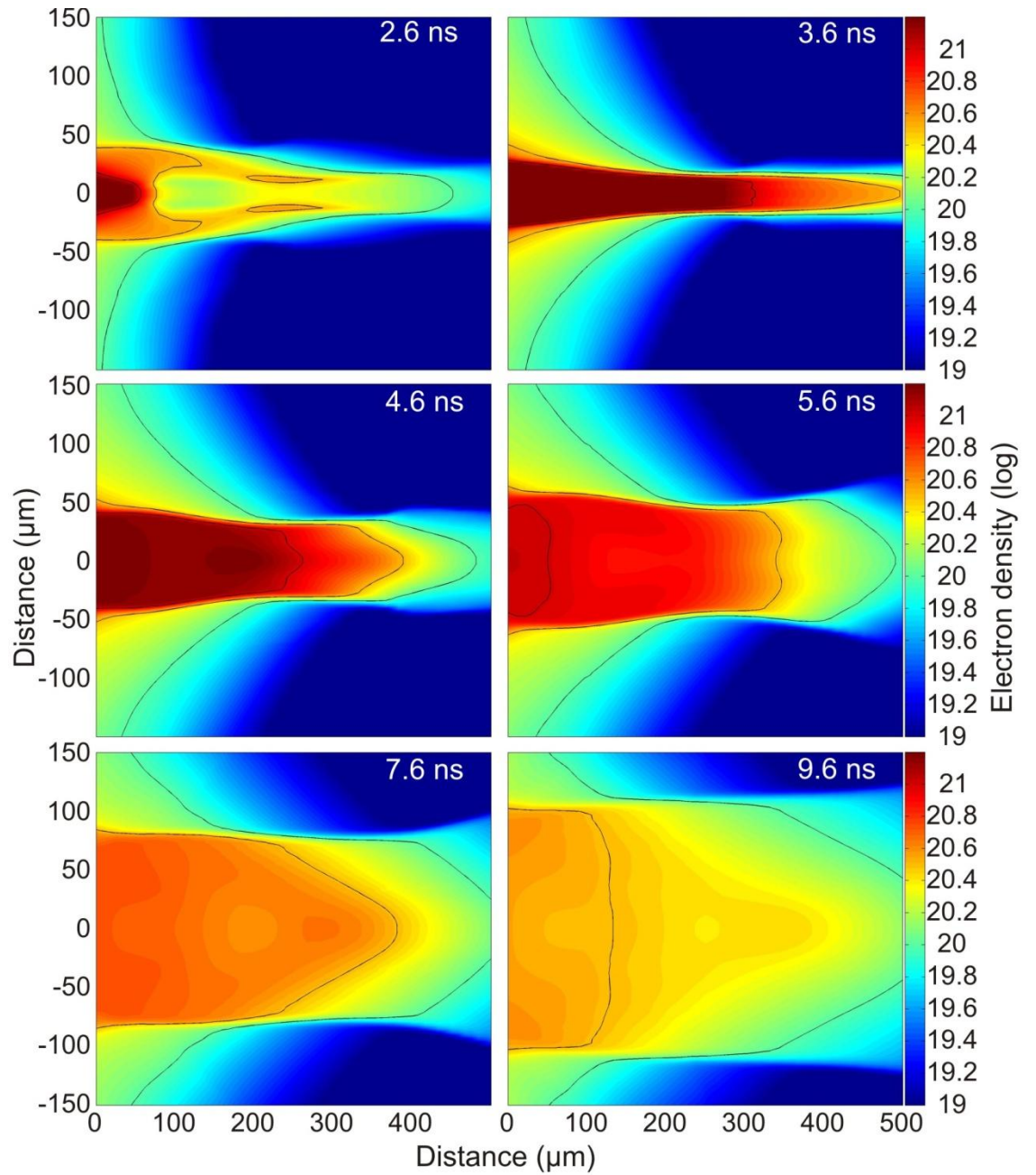


Figure 5.12. Simulated electron density maps from the hydrodynamic code HYDRA.

The plasma expansion follows a similar description of radiatively cooled jets found in a previous publication [39]. Plasma generated at the walls expands towards the axis of the conical target where it collides and is redirected outward along the length of the jet. When compared to

the V-groove targets used in our previous work the conical geometry generates denser plasma jets. This can be expected from the two dimensional nature of the radial plasma flow towards the axis of the cone, where it collides augmenting the jet. Initial electron temperatures near the target surface are computed to ~ 500 eV within $50 \mu\text{m}$ of the target tip at the peak of the laser pulse.

The emission of plasma radiation is computed to play a very significant role in the generation of a dense collimated plasma plume, by rapidly cooling the plasma jet and reducing the pressure. At 1.5 ns after target irradiation, the plasma is computed to have cooled to an electron temperature of less than 30 eV everywhere within the conical cavity. Simulations performed assuming an optically thick plasma show that the jet does not form in the absence of radiation cooling. In this case, the initial electron temperatures near the target surface reach similar values (~ 500 eV). The temperatures inside the cavity at 1.5 ns are as high as 120 eV, resulting in higher plasma pressures and a loss of collimation.

5.3. Conclusions

The evolution of a dense ($n_e \sim 10^{20} \text{ cm}^{-3}$) collisional plasma jet created by laser irradiation of triangular aluminum grooves at intensities of $\sim 1 \times 10^{12} \text{ W cm}^{-2}$ with 120 ps duration laser pulses was studied using soft x-ray laser interferometry. The highly collisional nature of this jet allows it to be modeled with a hydrodynamic code. The jet initially expands at a velocity of $\sim 3 \times 10^7 \text{ cm s}^{-1}$ with a Mach number of ~ 5 and reaches the edge of the $250 \mu\text{m}$ deep groove within the first nanosecond after laser irradiation. The jet is initiated by ablated material accelerated by a large pressure gradient at the target tip, and is augmented by the continual sequential arrival of wall material along the symmetry plane, where it collides and is re-directed outward. Early in the evolution, the jet has an electron temperature of ~ 55 eV and is highly ionized, radiating strongly

from Al X and Al XI ion lines. Simulations reveal that radiation cooling plays a significant role in reducing the pressure and maintaining the collimation of the jet. During the first few nanoseconds, when the jet possesses a high length-to-width ratio of ~ 10 , the jet is in the radiatively coupled regime ($\chi \sim 1$). Radiation cooling then decreases as time evolves. Later in the evolution the collision of the widening plasma jet with the counter-propagating plasma generated at the walls forms plasma side-lobes.

We have also generated dense plasma jets by laser irradiation of conical cavities with a relatively low irradiance of $6 \times 10^{12} \text{ W cm}^{-2}$ obtained by focusing 1 J laser pulses of 220 ps duration. The resulting collisional plasmas were studied using soft x-ray laser interferometry and multi-dimensional hydrodynamic simulations. A plasma jet with measured electron densities on axis $> 1.5 \times 10^{21} \text{ cm}^{-3}$ was observed 5.5 ns after target irradiation. The simulations corroborate that high dense plasma can be generated with relatively low energy laser pulses, and describe well the general dynamics of the plasma. The jet dynamics is similarly to that of planar plasma jets we previously studied by irradiation of V- shaped grooves: plasma created by the laser pulse irradiation of the bottom of the cavity forms an initial jet and plasma created by irradiation of the side walls of the cavity converges subsequently on axis where is re-directed along the axial direction, adding mass to the jet. Radiation cooling is found to play an important role in the jet formation.

5.4. References

- [1] A.H. Bride, and R.A. Perley, "Extragalactic radio jets," *Annu. Rev. Astron. Astrophys.*, vol. 22, pp. 319, 1984.

- [2] H. Zinnecker, M.J. McCaughrean, and J.T. Rayner, "A symmetrically pulsed jet of gas from an invisible protostar in Orion," *Nature*, vol. 394, pp. 862, 1998.
- [3] P.M. Bellan, "Miniconference on astrophysical jets," *Phys. Plasmas*, vol. 12, no. 058301, 2005.
- [4] K.J. Borkowski, J.M. Blondin, and J.P. Harrington, "Collimation of astrophysical jets: the proto-planetary nebula HE 3-4175," *Astrophys. J.*, vol. 482, pp. L97, 1997.
- [5] J.M. Blondin, B.A. Fryxell, and A. Konigl, "The structure and evolution of radiatively cooling jets," *Astrophys. J.*, vol. 360, pp. 370-386, 1990.
- [6] M.L. Norman, L. Smarr, K.-H. A. Winkler *et al.*, "Structure and Dynamics of supersonic jets," *Astron. Astrophys.*, vol. 113, pp. 285-302, 1982.
- [7] J. M. Foster, B. H. Wilde, P. A. Rosen *et al.*, "Supersonic jet and shock interactions," *Phys. Plasmas*, vol. 9, no. 5, pp. 2251-2263, 2002.
- [8] P. Nicolai, V. T. Tikhonchuk, A. Kasperczuk *et al.*, "Plasma jets produced in a single laser beam interaction with a planar target," *Phys. Plasmas*, vol. 13, no. 062701, 2006.
- [9] S. S. Harilal, C. V. Bindhu, and H.-J. Kunze, "Time evolution of colliding laser produced magnesium plasmas investigated using a pinhole camera," *J. Appl. Phys.*, vol. 89, no. 9, pp. 4737-4740, 2001.
- [10] S.R. Goldman, S.E. Caldwell, M.D. Wilke *et al.*, "Shock structuring due to fabrication joints in targets," *Phys. Plasmas*, vol. 6, no. 8, pp. 3327-3336, 1999.
- [11] S.R. Goldman, C.W. Barnes, S.E. Caldwell *et al.*, "Production of enhanced pressure regions due to inhomogeneities in inertial confinement fusion targets," *Phys. Plasmas*, vol. 7, no. 5, pp. 2007-2013, 2000.
- [12] A. Kasperczuk, T. Pisarczyk, S. Borodziuk *et al.*, "Stable dense plasma jets produced at laser power densities around 10^{14} W/cm²," *Phys. Plasmas*, vol. 13, no. 062704, 2006.

- [13] A. Kasperczuk, T. Pisarczyk, S. Borodziuk *et al.*, “The influence of target irradiation conditions on the parameters of laser-produced plasma jets,” *Phys. Plasmas*, vol. 14, no. 032701, 2007.
- [14] S. V. Lebedev, J. P. Chittenden, F. N. Beg *et al.*, “Laboratory astrophysics and collimated stellar outflows: the production of radiatively cooled hypersonic plasma jets,” *Astrophys. J.*, vol. 564, pp. 113-119, 2002.
- [15] D. R. Farley, K. G. Estabrook, S. G. Glendinning *et al.*, “Radiative jet experiments of astrophysical interest using intense lasers,” *Phys. Rev. Lett.*, vol. 83, no. 10, pp. 1982-1985, 1999.
- [16] K. Shigemori, R. Kodama, D. R. Farley *et al.*, “Experiments on radiative collapse in laser-produced plasmas relevant to astrophysical jets,” *Phys. Rev. E*, vol. 62, no. 6, pp. 8838-8841, 2000.
- [17] K. Shigemori, T. Dittmire, B. A. Remington *et al.*, “Developing a radiative shock experiment relevant to astrophysics,” *Astrophys. J.*, vol. 533, pp. L159-L162, 2000.
- [18] D. Ryutov, R.P. Drake, J. Kane *et al.*, “Similarity criteria for the laboratory simulation of supernova hydrodynamics,” *Astrophys. J.*, vol. 518, pp. 821-832, 1999.
- [19] V. A. Gribkov, Oleg N Krokhin, V. Ya Nikulin *et al.*, “Experimental investigation of nonspherical cumulative laser plasma configurations,” *Soviet Journal of Quantum Electronics*, vol. 5, no. 5, pp. 530-537, 1975.
- [20] D.T. Attwood, D.W. Sweeney, J.M. Auerbach *et al.*, “Interferometric confirmation of radiation-pressure effects in laser-plasma interactions,” *Phys. Rev. Lett.*, vol. 40, no. 3, pp. 184-187, 1978.
- [21] L.B. Da Silva, T.W. Barbee Jr., R. Cauble *et al.*, “Electron density measurements of high density plasmas using soft x-ray laser interferometry,” *Phys. Rev. Lett.*, vol. 74, no. 20, pp. 3991-3994, 1995.

- [22] A.S. Wan, J. T.W. Barbee, R. Cauble *et al.*, "Electron density measurement of a colliding plasma using soft x-ray interferometry," *Phys. Rev. E*, vol. 55, no. 5, pp. 6293-6296, 1997.
- [23] A.S. Wan, J. T.W. Barbee, R. Cauble *et al.*, "A soft x-ray laser interferogram of a high-density colliding plasma," *IEEE Transaction on Plasma Science*, vol. 27, no. 1, pp. 120-121, 1999.
- [24] H. Tang, O. Guilbaud, G. Jamelot *et al.*, "Diagnostics of laser-induced plasma with soft X-ray (13.9 nm) bi-mirror interference microscopy," *Appl. Phys. B*, vol. 78, pp. 975-977, 2004.
- [25] J. Filevich, K. Kanizay, M. C. Marconi *et al.*, "Dense plasma diagnostics with an amplitude-division soft x-ray interferometer based on diffraction gratings," *Optics Lett.*, vol. 25, no. 5, pp. 356-358, 2000.
- [26] J. Filevich, J.J. Rocca, M.C. Marconi *et al.*, "Picosecond-resolution soft x-ray laser plasma interferometry," *Applied Optics*, vol. 43, no. 19, pp. 3938-3946, 2004.
- [27] J.J. Rocca, C.H. Moreno, M.C. Marconi *et al.*, "Soft x-ray laser interferometry of a plasma with a tabletop laser and a Lloyd's mirror," *Optics Lett.*, vol. 24, no. 6, pp. 420-422, 1999.
- [28] J.J. Rocca, E.C. Hammarsten, E. Jankowska *et al.*, "Application of extremely compact capillary discharge soft x-ray lasers to dense plasma diagnostics," *Phys. Plasmas*, vol. 10, no. 5, pp. 2031-2038, 2003.
- [29] M. Purvis, J. Grava, J. Filevich *et al.*, "Dynamics of converging laser-created plasmas in semicylindrical cavities studied using soft x-ray laser interferometry," *Phys. Rev. E*, vol. 76, no. 046402, 2007.

- [30] R. Kodama, K.A. Tanaka, Y. Sentoku *et al.*, “Long-scale jet formation with specularly reflected light in ultraintense laser-plasma interactions,” *Phys. Rev. Lett.*, vol. 84, no. 4, pp. 674-677, 2000.
- [31] R.F. Smith, J. Dunn, J. Nilsen *et al.*, “Picosecond x-ray laser interferometry of dense plasmas,” *Phys. Rev. Lett.*, vol. 89, no. 6, pp. 065004(4), 2002.
- [32] J. Filevich, J. J. Rocca, M. C. Marconi *et al.*, “Observation of a multiply ionized plasma with index of refraction greater than one,” *Phys. Rev. Lett.*, vol. 94, no. 035005, 2005.
- [33] M. M. Marinak, S. W. Hann, T. R. Dittrich *et al.*, “A comparison of three-dimensional multimode hydrodynamic instability growth on various National Ignition Facility capsules designs with HYDRA simulations,” *Phys. Plasmas*, vol. 5, no. 4, pp. 1125, 1998.
- [34] M. M. Marinak, G. D. Kerbel, N. A. Gentile *et al.*, “Three-dimensional HYDRA simulations of National Ignition Facility targets.” pp. 2275-2280.
- [35] R. M. More, K. H. Warren, D. A. Young, and G. B. Zimmerman, “A new quotidian equation of state (QEOS) for hot dense matter,” *Phys. Fluids*, vol. 31, no. 10, pp. 3059, 1988.
- [36] Y.T. Lee, and R. M. More, *Phys. Fluids*, vol. 27, pp. 1273, 1984.
- [37] Shay Gueron, and Moshe Deutsch, “A fast Abel inversion algorithm,” *J. Appl. Phys.*, vol. 75, no. 9, 1994.
- [38] R.M. More, K.H. Warren, D.A. Young *et al.*, “A new quotidian equation of state (QEOS) for hot dense matter,” *Physics of Fluids*, vol. 31, no. 10, pp. 3059-3078, 1988.
- [39] M. A. Purvis, J. Grava, J. Filevich *et al.*, “Collimation of dense plasma jets created by low-energy laser pulses and studied with soft x-ray laser interferometry,” *Phys. Rev. E*, vol. 81, no. 3, pp. 036408, 2010.

Chapter 6. Conclusions

The dynamics of various laser-created dense were studied. The main diagnostic instrument used was a powerful short wavelength optical interferometry technique that combined a compact table-top soft x-ray laser source and a robust diffraction grating interferometer, both developed at Colorado State University. The plasmas studied were created by irradiating different target materials and geometries with high energy short optical laser pulses. Depending on the shape of those targets, dense colliding plasmas or plasma jets were created. The relatively short duration of the probe beam pulse allowed taking “snapshots” of the plasmas, providing series of high contrast interferograms that depict the plasma evolution. Two dimensional electron density maps were obtained from the analysis of these interferograms.

In a first set of experiments, the dense colliding plasmas were created by the irradiation of semi-cylindrical grooved targets with an intensity of $1 \times 10^{12} \text{ W.cm}^{-2}$. The initial phase of the plasma evolution is characterized by its rapid expansion away from the wall. Subsequently, the plasma converges near the axis of the half-cylindrical groove, where it interacts with negligible interpenetration, forming a concentrated collisional high electron density region. At late times, recombination and cooling of the plasma results in lower densities and strong absorption of the soft x-ray probe close to the target walls. Experiments performed on aluminum and copper targets showed a similar behavior, with measured electron densities on axis near the center of the half-cylindrical cavity reaching values as high as $1 \times 10^{20} \text{ cm}^{-3}$. The uneven heating of the target caused

by the heating beam profile creates hotter denser plasmas at the bottom of the groove. These hotter plasmas expand faster, reaching the axis of the groove first, where it converges and forms the dense plasma focus. Factors that have a strong effect on the behavior of these dense colliding plasmas are the width of the line focus, the energy deposited on target, and the target material.

During the study of the colliding copper plasmas, time integrated self-emission images from the plasma in the EUV region showed late in the evolution the presence of a long narrow arc emitting light outside the cavity indicative of the presence of a shock. In order to study the dynamics of this bow shock, a visible optical interferometer was built to probe the copper plasmas. A quasi-stationary bow shock was observed to develop at late times as a result of the collision between the expanding central plasma focus and plasma generated by ablation of the flat target walls surrounding the semi-cylindrical cavity. This collisional shock reaches a measured electron densities of $\sim 6 \times 10^{18} \text{ cm}^{-3}$. The bow shock is sustained for several tens of nanoseconds by the continuous arrival of plasma ablated from the target walls. The experimental results were supported by numerical simulations performed using the hydrodynamic code HYDRA. The simulations and experiments agreed well in describing the behavior of these plasmas, including similar peak electron densities of the dense plasma focus and the shape and densities of the late bow shock.

In the experiments presented in Chapter 5, dense collisional planar plasma jets were created by laser irradiation of triangular grooves with an intensity of $1 \times 10^{12} \text{ W.cm}^{-2}$ from short (120 ps) duration laser pulses, and studied with the soft x-ray laser interferometry technique. The jet was measured to initially expand at a velocity of $\sim 3 \times 10^7 \text{ cm.s}^{-1}$ with a Mach number of ~ 5 . The jet is initiated by ablated material accelerated by a large pressure gradient at the target tip, and is augmented by the continual sequential arrival of wall material along the symmetry plane, where it collides and is re-directed outward. The evolution of these collisional jets was also modeled with the hydrodynamic code HYDRA. Early in the evolution, the jet is highly ionized

and has an electron temperature of ~ 55 eV. Simulations reveal that radiation cooling plays a significant role in reducing the pressure and maintaining the collimation of the jet. During the first few nanoseconds, when the jet possesses a high length-to-width ratio of ~ 10 , the jet is in the radiatively coupled regime ($\chi \sim 1$). Radiation cooling decreases as time evolves. Later in the evolution the collision of the widening plasma jet with the counter-propagating plasma generated at the walls forms distinct plasma side-lobes.

In the last set of experiments, high density ($>10^{21}$ cm $^{-3}$) plasma jets were created by irradiation of conical grooves at a low intensity of 7×10^{12} W.cm $^{-2}$. A narrow collisional plasma jet is seen to exit the cavity at 5.5 ns with measured electron densities on axis higher than 1.5×10^{21} cm $^{-3}$. Early simulation agrees well with the general behavior of the jet but tend to overestimate the electron density. This jet behaves similarly to the planar plasma jets previously studied: plasma created by the laser pulse irradiation of the bottom of the cavity form the initial jet. Material created by irradiation of the side walls from plasma radiation contributes to the mass of the jet and enhances its collimation. Radiation cooling of the plasma was found to play an important role in the early stages of the jet formation. This is the first time such dense plasmas ($>10^{21}$ cm $^{-3}$) are created with low intensities ($<10^{12}$ W.cm $^{-3}$).

All these experiments demonstrate that a variety of dense plasmas with different dynamics could be created with low energy laser pulses and studied with soft x-ray laser interferometry coupled with numerical simulations. Many of these plasma configurations, including plasma jets and bow shocks, are of interest to the astrophysical community, as these high energy density laboratory experiments can bridge the gap between observational data, theory and numerical simulations.

Appendix A. Numerical Hydrodynamic simulations

A plasma is a collection of charged particles with a complex behavior that depends not only on the local conditions but also on the state of the plasma in other regions. Modeling the evolution of a plasma can be a very difficult problem. For low density plasmas ($<10^6$ atoms/cm³), codes can track the individual trajectories of the particles and their interaction within the plasma [1-3]. These particle-in-cell (PIC) codes have the advantage of being fairly straightforward, but as the number of particles to track increases, the computational power needed to solve the system becomes unreasonably large. Therefore, for higher density plasma, a macroscopic compressible fluid-like approach is generally preferred [4-5]. These hydrodynamic codes treat the plasma motion as a fluid, outputting quantities such as density, averaged velocities, temperature and mean ionization. To accurately represent other non-fluid aspects of the plasma, additional parameters can be computed and included in the simulation, to take into account heat conductivity, radiation transport or collisions between particles.

Hydrodynamic simulations have inherent limitations due to the discrete nature of computer programs. Therefore, to input the problem in a numerical code, it is necessary to approximate the continuous plasma by breaking it down into distinct parts. This process is called discretization. The discretization is typically done by dividing the spatial coordinates into a grid composed of smaller, finite elements called cells. These cells map the plasma to a logical system used for computer calculations. Each cell contains local values of the plasma parameters, located either at its center (cell centered scheme) or at the intersection of the grid lines (node centered scheme). Any external or internal forces applied to the mesh are considered, and the values of the plasma inside the cells are changed accordingly. Conservation equations are then applied to each

cell of the mesh, and at each time step the plasma parameters within the cells are updated. The process then continues until the code converges to a solution. A complete picture of the plasma evolution can be put together from the solution of each of these cells.

Different meshing methods can be used to keep track of the plasma parameters within each grid cell, each with their own advantages and limitations. They are presented in section A.1. The equations describing the motion of the plasma will be discussed in section A.2, along with the equation of state and conductivity models. Section A.3 discusses radiation modeling and transport within the plasma.

A.1. Discretization and meshing techniques

A.1.1. Meshing: Eulerian method

This is the simplest form of meshing. In this scheme, the spatial grid is initially defined, and remains unchanged during the simulation. Conservation equations are solved for each cell at each time step. Using the resulting plasma parameters, the fluxes from and to each cells are computed, and mass can move from cell to cell accordingly, providing the new plasma parameters input for the next calculation step. This method is quite simple and allows for sophisticated numerical solutions of the conservation equations. However, mass advection is usually hard to represent accurately as uncertainties can arise when moving mass from one cell to another.

A.1.2. Meshing: Lagrangian method

Initially, a spatial mesh is associated with the material composing the plasma. This mesh is then dragged along with the material as it moves: this is the Lagrangian picture. The hydrodynamic code allows for the mesh to deform, as the mass density in each cell remains constant. Using this scheme, there is no need for mass advection from one cell to another, and the mass is accurately followed. However, the mesh can progressively get more entangled as the calculations proceed, with cells stretching, shrinking or becoming unrealistically distorted to the point where the code cannot resolve the grid anymore.

A.1.3. Meshing: Arbitrary Lagrangian Eulerian (ALE) method

This technique is actually a combination of both the Eulerian and Lagrangian pictures: the mesh is allowed to follow the mass, with mass advection steps applied when necessary. This method is very powerful, as it can help prevent any distortions of the Lagrangian mesh without relying too often on the Eulerian mass advection steps. While it is powerful, this method is also the most complicated to implement. In the simulations of plasmas described herein, the hydrodynamic code HYDRA uses a mesh with an ALE technique to spatially keep track of the parameters.

A.2. Fluid hydrodynamics: a basic description for plasmas

A plasma can be modeled as an ideal compressible fluid, whose movement can be described by a set of fluid equations. These equations are the continuity equation, conservation of momentum and energy conservation. A numerical code typically solves these equations for some initial values, boundary conditions and any external perturbations applied on the system. In the case of a plasma, properties such as the thermal conductivity, viscosity and absorption can have significant effects on the evolution of the plasma, and need to be added to the fluid equations for proper treatment of the problem.

Hydrodynamic codes can model the fluid-like behavior of plasma with various schemes. In the most general case, a single fluid model is accurate enough to track the motion of the whole plasma as a single fluid. In certain particular cases, it is more advantageous to track each species in the plasma (i.e. electrons and ions) as two (or more) separate fluids interacting with each other through electrostatic forces. Depending on the electron-ion equilibration time, it can be more accurate to simulate the plasma as a single temperature plasma (when electrons and ions are in equilibrium), two temperatures plasma (one for electrons and ions), or multi temperatures plasma, for example if a radiation temperature is also considered.

For the simulations of the experimental plasma presented herein, the hydrodynamic code runs a single fluid two temperature model for electrons and ions. In addition, a set of radiation temperatures is used to describe the plasma radiation. This is motivated by the fact the plasmas considered in those experiments are composed of mostly the same atoms, and that the collision time between same species particles (ion-ion and electron-electron) is larger than the collision equilibration time between ions and electron. However, both species may not necessarily be in

equilibrium with each other. Therefore, it is more accurate to compute the temperature of the electrons and ions separately.

For a single fluid two temperature model, the conservation equations used are based on the Euler equations. The code must solve a single conservation of mass equation, one conservation of momentum equation with a modified pressure term to account for both electrons and ions pressure. Two equations for conservation of energy must be used, one for each species. The next section will describe those equations in more details for an ALE representation.

A.2.1. Equation for the motion of fluid

As discussed previously, a dense plasma can be described as behaving like a hydrodynamic fluid. This means that its evolution is described by the Euler equations. This fluid-like representation is typically valid for dense, collisional plasmas. In this case, the Euler equations of motion can be written as:

$$\frac{\partial \rho}{\partial t} + \nabla \cdot (\rho \mathbf{v}) = 0 \quad \text{for continuity,}$$

$$\rho \left(\frac{\partial \mathbf{v}}{\partial t} + \mathbf{v} \cdot \nabla \mathbf{v} \right) + \nabla p = 0 \quad \text{for the conservation of momentum, and}$$

$$\frac{\partial p}{\partial t} - \gamma \frac{p}{\rho} \frac{\partial \rho}{\partial t} + \mathbf{v} \cdot \nabla p - \gamma \frac{p}{\rho} \mathbf{v} \cdot \nabla \rho = 0 \quad \text{for energy conservation.}$$

where ρ is the mass, p the pressure, \mathbf{v} is the fluid velocity and γ is the adiabatic constant.

These equations must take into account any sources/losses caused by plasma expansion, thermal conductivity, atomic losses, emission/absorption of radiation. Since the hydrodynamic code that simulates the experiments presented herein uses an ALE technique for the mesh movement, the conservation equations in ALE form are presented next.

The Arbitrary Lagrangian Eulerian conservation equations can be derived from a simple idea. The computational mesh moves with respect to fixed space with a velocity v_g , a function of space and time defined by the code. If v_g were zero, the mesh would be fix and the simulation Eulerian. If v_g were the fluid velocity v , the mesh would follow the mass and the simulation would be Lagrangian. The code can decide to use any value of v_g between those two limits. A derivation of the ALE conservation equations is given in [6] by replacing the Eulerian time derivative $\frac{\partial}{\partial t}$ with $\left(\frac{\partial}{\partial t}\right)_g - v_g \Delta$, where $\left(\frac{\partial}{\partial t}\right)_g$ is the time derivative at a fixed point g in the mesh. The conservation equations can then be written as:

$$\frac{1}{J} \left(\frac{\partial \rho J}{\partial t} \right)_g + \nabla \cdot (\rho(v - v_g)) = 0$$

$$\frac{1}{J} \left(\frac{\partial \rho J}{\partial t} \right)_g + \nabla \cdot (\rho(v - v_g)v) + \nabla p - F = 0$$

$$\frac{1}{J} \left(\frac{\partial}{\partial t} \right)_g \left[\rho J \left(e + \frac{1}{2} v^2 \right) \right] + \nabla \cdot \left[\rho(v - v_g) \left(e + \frac{1}{2} v^2 \right) + pv \right] - \rho q - v \cdot F = 0$$

where $J = \frac{\partial(x, y, z)}{\partial(\xi, \eta, \zeta)}$, is the Jacobian of the mapping from ALE coordinates to Cartesian

coordinates. The first equation is the conservation of mass, and ensures that the rate of change of mass density is balanced by changes in mass flux $\nabla \cdot (\rho(v - v_g))$ in and out of a cell. The second equation is the conservation of momentum. The rate of change in momentum should be balanced by the flux of momentum $\nabla \cdot (\rho(v - v_g)v)$, the momentum flux due to pressure ∇p and any momentum due to external forces F . The last equation is the conservation of energy, taking into account both the internal energy ρe and the kinetic energy $\frac{1}{2} \rho v^2$. In addition to these three

equations, an equation relating pressure to temperature and density must be added. This equation of state (EOS) is required to obtain a complete solvable set of equations.

A.2.2. Equation of state (EOS)

The equation of state is a thermodynamic relation describing the state of matter under certain conditions. It is typically used to relate pressure, internal energy, density and temperature. One of the simplest equations of state is the ideal gas law $pV = nRT$, relating the pressure p and volume V to the density n and temperature T . This EOS is accurate for gases at low pressures and moderate temperatures, but breaks down for higher values of p and T . Another equation of state is based on the Thomas-Fermi-Dirac model of the atom [7-8]. This method uses a statistical model to approximate the distribution of electrons in an atom and obtain the pressure as a function of temperature and density. However, this model quickly becomes inaccurate at densities lower than 10^{20} atoms/cm³. Note that no EOS can accurately predict the properties of all matter under any states and conditions, but rather there exists accurate EOS for certain specific sets of conditions. Since hydrodynamic codes rely heavily on the equation of state, it is important to choose the correct EOS closely matching the conditions of the problem to simulate. In the case of laser-created dense plasmas of our interest, this means the EOS must describe correctly the transition from solid, liquid or gas to the high energy density (HED) plasma regime. Most EOS have tabulated values that can be easily used by the numerical model and extrapolated for particular values. In any case, equations of state can give results that are typically accurate within a factor two. In the computations with the code HYDRA performed to simulate the plasmas described in this dissertation, the Livermore Equation of State (LEOS) and Quotidian Equation of State (QEOS) [8] were used.

A.2.3. Thermal conductivity

The thermal conductivity is an important property that describes how quickly heat is transported within the plasma. For ideal non magnetized plasmas, the thermal conductivity can be written as [9]:

$$\kappa_e = 8 \left(\frac{2}{\pi} \right)^{3/2} \frac{(kT_e)^{5/2}}{\sqrt{m} Z e^4 \ln \Lambda}$$

Where $\ln \Lambda$ is the Coulomb logarithm, Z is the mean ionization, e is the charge of the electron, m is the mass of the ions and kT_e is the electron temperature. The thermal conductivity strongly varies with the temperature (scales as $T_e^{5/2}$).

A widely used model for the conductivity of dense plasmas has been derived by Lee and More [10]. When temperature gradients become very large, the thermal conductivity can become unphysical: as the temperature gradient approaches infinity, so does the heat transported, $q_c = -\kappa \Delta T$. To prevent this issue, all codes use a heat flux limiter to control the degree of heat flow in the model. Typical values of flux limiter vary from 0.05 to 0.3.

A.3. Radiation transport within the plasma

A.3.1. Overview of radiation

Hot dense plasmas are very efficient at radiating energy. Therefore, the accurate treatment of radiation and its transport within the plasma is critical in any simulations. The energy that leaves the plasma through radiation can escape the problem or be reabsorbed in another part of the plasma. Radiation can play an important role in the dynamics of the plasma, when radiative flux and pressure become comparable to material flux and pressure [11].

There are several ways to take into account radiation and its transport within a plasma. One method consists in using an accurate atomic model that solves for the population of all excited states and the emission of radiation from all the lines in the atoms. In this case, the total computed radiation translates into absorption and emission coefficients used to solve the transport equation. Another method uses approximations to get the emission and absorption coefficients based on opacities. The next section describes a collisional-radiative model and explains how to compute the radiation emitted and absorbed within the plasma. Section 3.3 then presents the radiation transport equation, along with what is considered by far the most important approximate treatment of radiation transport: the diffusion approximation. The last section will review a particular case in the diffusion approximation to get the opacities without the need to solve a full atomic model, using the Plank and Rosseland mean opacities, and describes the multi-group technique used to further simplify calculations.

A.3.2. Collisional-radiative model

A collisional-radiative model uses the atomic properties of the plasma to compute its total radiation. Using an atomic model, the energy levels and ionization potentials of all the relevant ions are solved for. Recombination and ionization processes can change the overall charge of the ions, affecting the electron and ion densities. Within the ions, a number of excited states can also change through excitation and de-excitation, emitting or absorbing photons in the process. This can lead to radiative transport within the plasma, changing its local temperature.

Figure A.1 shows an energy level diagram with some of the most important atomic processes inside the plasma. It is important to note that for every process there is an inverse process. Using this principle of detailed balance, once the rate of a process has been computed, it is easy to calculate the rate of its inverse.

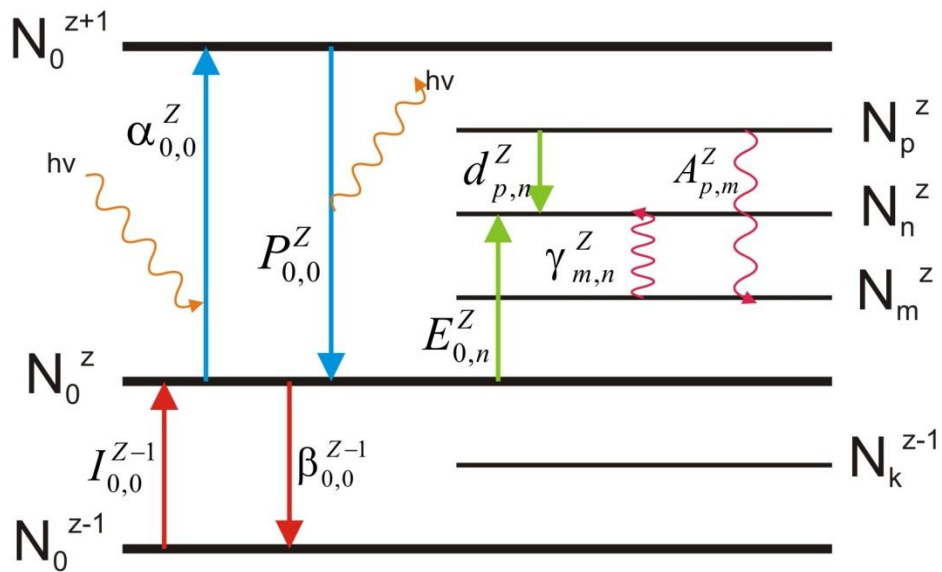


Figure A.1. An energy level diagram depicting some of the atomic processes occurring between levels in an atom.

Collisional ionization ($I_{0,0}^{Z-1}$, also called electron impact ionization) is the process in which a free electron collides with an ion and transfers some of its energy to it. This results in another electron being knocked off the ion, leaving it in an ionized state. The electrons resulting from this process will have lower energy. Also this process can occur only when the energy of the incoming electron is higher than the ionization potential of the ion, requiring more energetic electrons to ionize higher states. This means that the electron impact ionization rate drops significantly for lower temperature plasmas.

Electron impact recombination (or 3-body recombination $\beta_{0,0}^{Z-1}$), is the inverse process of collisional ionization. Two slow moving electrons collide with the atom. One of the electrons will recombine with the atom to obtain an ion in a lower state, while the other electron will carry away the excess energy. Since two electrons need to participate in this process, the rate equation has a dependency on n_e^2 .

The photo ionization process $P_{0,0}^Z$ is important as it absorbs a photon and can influence the cooling mechanism of the plasma. In the photo ionization process, a photon of sufficient energy is absorbed by the atom to increase its ionization level, releasing an electron in the process. The photon energy needs to be equal or higher than the energy difference between the two excited levels of the ion.

The inverse process of photo ionization, radiative recombination $\alpha_{0,0}^Z$ is also an important cooling mechanism for the plasma. A free electron is captured by an ion, which then emits a photon to conserve energy and momentum. The photon released by this process can escape the plasma, lowering its temperature, or be reabsorbed by another process after traveling through the plasma.

Electron impact excitation, also called collisional excitation $E_{0,n}^Z$, is the process where a free electron collides with an ion, transferring some of its energy to the ion and leaving it in an

excited state. This process can occur between any two states of an ion (ground state or excited states). Like collisional ionization, the electron must have sufficient energy to excite the atom through collision, therefore the rate of this process drop rapidly for electrons of lower temperature.

Collisional de-excitation $d_{p,n}^Z$ is the inverse process of electron impact excitation. A free electron collides with an ion in an excited state: energy is transferred to the electron, leaving the ion in a lower state (excited or ground state).

Radiative decay $A_{p,m}^Z$, also called spontaneous emission, is an important cooling mechanism in plasmas. An electron in an excited state can spontaneously decay to a lower state, emitting a photon in the process. The rate of photon emission is given by Einstein's A coefficient. Radiative decay accounts for all the line radiation in the atom, and plays an important role in radiation transport. The inverse process of radiative decay is photo excitation $\gamma_{m,n}^Z$, where a bound electron is transferred to an upper excited state while absorbing a photon.

When all relevant processes have been put in equation, the next step is to solve this model. This is done by evaluating the rate of change of the population of individual states (ground and excited). For each level, an equation can be written taking into account all processes leaving the level as sink terms and all processes ending on this level as source terms. For example, in the picture described in Figure A.1 the equation of the ground state N_0^Z will be:

$$\frac{dN_0^Z}{dt} = P_{0,0}^Z + I_{0,0}^{Z-1} - \alpha_{0,0}^Z - \beta_{0,0}^{Z-1}$$

When all equations are obtained, several approximations in the collisional-radiative model can be taken to simplify the analysis. In the steady state approximation, the changes in the populations of ground and excited states are slow compared to the change in temperature. In this particular case, $\frac{dN_n^Z}{dt}$ (excited states) and $\frac{dN_g^Z}{dt}$ (ground states) can be equated to zero, greatly simplifying the problem. This approximation can be taken, for example, in Tokamak plasmas or

slow evolving plasmas. In the quasi-steady state approximation, moderately fast changes take place in the plasma, and only the rate of change of ground states can be equated to zero. When changes in the population rates are faster than changes in the electron temperatures, as is the case in transient plasmas created by femtosecond lasers, no approximations can be taken and the complete set of equation has to be solved.

By solving this collisional-radiative model, an accurate description of the plasma can be obtained, and the radiation emitted and absorbed by the plasma can be computed. Three types of radiation can be found inside a plasma: bound-bound, free-bound and free-free radiation. Each one needs to be accurately model to properly account for radiative gain and loss in a numerical model.

Bound-bound radiation, often the dominant component in hot plasmas, consists of all the line radiation occurring within the plasma, when an electron in an excited state spontaneously decays to a lower state (radiative decay). There can be many lines emitting within a plasma, each with a different central frequency and line width. Accurately computing the total radiation emitted from those lines is actually very difficult. Any radiation modeling must take into account the atomic line width as well as processes that can broaden them such as natural, Doppler or Stark broadening.

Free-bound radiation occurs when an ion recombines with an electron and emits a photon. While important in plasmas, bound-free radiation is still orders of magnitude lower than bound-bound radiation.

The last type of radiation that can occur in a plasma is free-free radiation, also called Bremsstrahlung radiation. When a free electron is deflected by the electric field of a nearby atom, a photon is emitted. Bremsstrahlung radiation is usually also orders of magnitude smaller than bound-free radiations.

When summing all the processes that lead to emission of radiation from the plasma, an emissivity coefficient J_ν can be computed. On the other hand, by adding all the processes that absorb radiation within the plasma, an absorption coefficient κ_ν can be defined. These two coefficients are then used to solve the radiation transport equation as will be described next.

A.3.2. Radiation transport equation and the diffusion approximation

Consider a ray of light with an intensity I_ν traveling through a volume V of cross sectional area dA and thickness ds , as shown in Figure A.2.

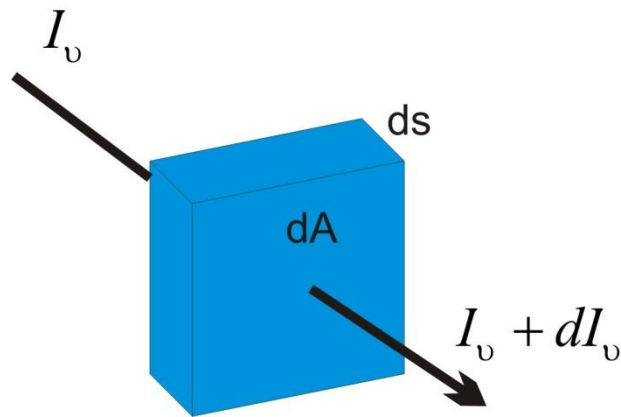


Figure A.2. Light can have its intensity I_ν modified when traveling through a volume V of cross section dA and thickness ds

The intensity at the output of the volume is $I_\nu + dI_\nu$. Absorption of the ray within the volume can decrease the output intensity: this is represented by the absorption coefficient of the volume κ_ν . Any light emitted from the volume along the direction of propagation of the ray could also contribute to an increase in the output intensity. This is quantified by the emission coefficient

of the volume j_ν . Therefore, a general equation for the change of intensity of a ray traveling through a volume of thickness ds can be written as:

$$\frac{dI_\nu}{ds} = j_\nu - \kappa_\nu I_\nu \quad (\text{eq.A.3.1})$$

Equation (eq.A.3.1) is called the radiation transport equation. The emission coefficient (or emissivity) has units of intensity per unit length, and the absorption coefficient has units of inverse length. If we consider only the absorption of a ray of intensity I_ν traveling through a plasma of thickness L , the change in intensity is written as:

$$I_\nu = I_\nu^0 \exp(-\kappa_\nu L)$$

Where $\kappa_\nu L = \tau$ is defined as the optical depth of the plasma. For values of $\tau \ll 1$, all the radiation within the plasma is allowed to escape. No radiation is reabsorbed in the plasma, leading to strong cooling by radiation. In this case, the plasma is said to be optically thin, and the resulting intensity exiting the plasma is the sum of all emission along the path of the ray: $I_\nu + dI_\nu = \int j_\nu ds$. In the case where the optical depth is larger than unity, the plasma is said to be optically thick. In this limit all the radiation emitted is entirely reabsorbed in the plasma, and no radiation is allowed to escape the volume. Therefore, in this case there is no cooling of the plasma through radiation. Note that the reabsorption of radiation needs not take place at the same location where it was emitted. In fact, radiation is typically transported to other regions within the plasma, changing the local temperatures when it is reabsorbed.

Plasmas typically possess optical depths within these limiting cases: to compute the radiation transport of these plasmas, equation (eq.A.3.1) is solved for many finite volumes along the total length of the plasma for a wide range of frequencies, requiring significant computational time. However, there are several approximations that can be used to solve the radiation transport

equation. The most important approximate treatment of radiation transport method is the diffusion technique.

If the distance a photon travels before it interacts with the plasma (i.e. the radiation mean free path $\frac{1}{\kappa_\nu}$) is small compared to typical length of system, the radiation transport equation can be approximated using radiation diffusion techniques, often much simpler to solve than the complete transport equation. In this limit, the radiation can be treated as an ideal fluid with small corrections. Equation (eq.A.3.1) can be rearranged as:

$$I_\nu = \frac{J_\nu}{\kappa_\nu} - \frac{1}{\kappa_\nu} \left(\frac{dI_\nu}{ds} \right) \quad (\text{eq.A.3.2})$$

Since the assumption is that κ_ν is large, then the second term of (eq.A.3.2) is a small correction to the first term. Then we can use this equation to obtain I_ν by successive approximations. The first approximation is

$$I_\nu^0 = \frac{J_\nu}{\kappa_\nu} \quad (\text{eq.A.3.3})$$

This is a local balance approximation where the radiation is in equilibrium with the sources. The second step of the successive approximation is to use I_ν^0 to compute I_ν^1 :

$$I_\nu^1 = \frac{J_\nu}{\kappa_\nu} - \frac{1}{\kappa_\nu} \left(\frac{dI_\nu^0}{ds} \right)$$

For standard diffusion approximation, there is no need to include more terms, as if κ_ν is large indeed, then the next term would be too small to matter. Note that the diffusion radiation technique does not require the code to solve a complete atomic model, but rather relies on opacities that might not be available in tabular form as a result of the use of other codes, as will be shown in the next section.

A.3.3. Rosseland mean opacities and the multi-group technique

Another step can be taken to simplify the transport equation in the diffusion approximation: it is customary to define average opacities over frequencies, using a particular weight scheme. For example, if the sources and sink terms of equation (eq.A.3.3) are those for matter at a temperature T , then a Planck black body radiation energy density distribution $B_\nu(T)$ can be used as a weighting function to compute an average opacity κ . This is called the Planck mean opacity and is an alternative technique from calculating the opacity using an atomic model.

The Rosseland mean opacity [12] is another such technique, and is using the temperature derivative of the Planck function to weight the average opacity:

$$\frac{1}{\kappa} = \frac{\int_0^\infty d\nu \frac{1}{\kappa_\nu} \frac{dB_\nu(T)}{dT}}{\int_0^\infty d\nu \frac{dB_\nu(T)}{dT}}$$

where $B_\nu(T)$ averaged over all frequencies is taken as the black body radiation defined by σT^4 .

While it is possible to average the opacities over all frequency, it is usually more accurate to divide the spectral density of the plasma into several smaller sets of chosen frequency intervals also called groups. This technique known as multi-group radiation further helps reducing the computational power needed to solve the radiation transport equation. Each group is assigned a mean opacity value averaged over the frequencies within the particular group, using one of the aforementioned methods. In the particular case of the Rosseland mean opacities (as it is relevant for the code HYDRA used to simulates the plasmas herein), each group will have a radiation

temperature T_R , that is consequently used as another ideal fluid added to the plasma with its own conservation of energy equation.

Nowadays, the calculation of opacities has become very elaborate, and tables are available that contains opacity values for different conditions. Depending on the application, the particular table is read into memory and supply the code with values that can be extrapolated as needed. Los Alamos Opacity Library [13] is an example of large and complete opacity tables available for various conditions.

A.4. References:

[1] B. F. Lasinski, A. B. Langdon, S. P. Hatchett *et al.*, "Particle-in-cell simulations of ultra intense laser pulses propagating through overdense plasma for fast-ignitor and radiography applications." pp. 2041-2047.

[2] M.E. Jones, D.S. Lemons, R.J. Mason *et al.*, "A grid-based Coulomb collision model for PIC codes," *J. Comput. Phys.*, vol. 123, pp. 169-181, 1996.

[3] P. C. Liewer, and V. K. Decyk, "A general concurrent algorithm for plasma particle-in-cell simulation codes," *J. Comput. Phys.*, vol. 85, no. 2, pp. 302-322, 1989.

[4] J. T. Larsen, and S. M. Lane, "HYADES--A plasma hydrodynamics code for dense plasma studies," *Journal of Quantitative Spectroscopy and Radiative Transfer*, vol. 51, no. 1-2, pp. 179-186.

[5] M. M. Marinak, G. D. Kerbel, N. A. Gentile *et al.*, "Three-dimensional HYDRA simulations of National Ignition Facility targets." pp. 2275-2280.

[6] J. I. Castor, *Radiation Hydrodynamics*: University Press, Cambridge, United Kingdom, 2004.

- [7] L. H. Thomas, *Proc. Cambridge Philos. Soc.*, vol. 23, 1927.
- [8] R.M. More, K.H. Warren, D.A. Young *et al.*, “A new quotidian equation of state (QEOS) for hot dense matter,” *Physics of Fluids*, vol. 31, no. 10, pp. 3059-3078, 1988.
- [9] S. I. Braginskii, *Transport processes in a plasma*, 1965.
- [10] Y.T. Lee, and R. M. More, *Phys. Fluids*, vol. 27, pp. 1273, 1984.
- [11] R. P. Drake, *High-Energy-Density Physics: Fundamentals, Inertial Fusion, and Experimental Astrophysics (Shock Wave and High Pressure Phenomena)*: Springer Press, 2006.
- [12] S. Rosseland, *Monthly Notices of the Royal Astronomical Society*, vol. 84, no. 720, 1924.
- [13] W. F. Huebner, A. L. Merts, N. H. Magee *et al.*, Report LA-6760-M, Los Alamos, NM: Los Alamos Scientific Laboratory, 1977.

Appendix B. Analytic Spline Abel Inversion (ASAI) MATLAB Implementation

The ASAI algorithm used to obtain the phase information from the fringe shift maps of the plasma jets experiment is presented herein. The algorithm is based on M. Deutsch and I. Beniaminy (see Chapter 6), and was implemented in MATLAB.

```
%% Script to process the fringe shift maps and perform the Abel Inversion using
% the ASAI algorithm.
% Required external files: progressbar.m, abel_inversion.m
% <interferogram> MAT.mat file must be opened to provide fringe shift data from
% array ZI.
% Overview of script_fringe_synth.m %
% 1) Open data file to obtain fringe shift information and axis information.
% 2) Smooth data by flipping over symmetry axis.
% 3) Call Abel inversion algorithm one column of data at a time.
% 4) Multiply by correct factor to obtain density and plot.
close all;clear all;clc;warning('off'); %#ok<WNOFF>
```

```
% List of files to be used for each time
```

```
%%{
```

```
timing='050ns' ; % Cu 1118 5.0ns
```

```
load '91118036 MAT.mat'
```

```
plasmafn='91118036' ;
```

```
%%}
```

```
{
```

```
timing='070ns' ; % Cu 1118 7.0ns
```

```
load '91118084 MAT.mat'
```

```
plasmafn='91118084' ;
```

```
}
```

```
{
```

```
timing='090ns' ; % Cu 1118 9.0ns
```

```
load '91118083 MAT.mat'
```

```
plasmafn='91118083' ;
```

```
}
```

```
{
```

```
timing='100ns' ; % Cu 1118 10.0ns
```

```
load '91118053 MAT.mat'
```

```
plasmafn='91118053' ;
```

```

%}

%{
timing='110ns'; % Cu 1118 11.0ns
load '91118045 MAT.mat'
plasmafn='91118045';
%}

%{
timing='120ns'; % Cu 1118 12.0ns
load '91118029 MAT.mat'
plasmafn='91118029';
%}

%%

% Plots the phase map, then gets the zone with no information
fid=fopen([plasmafn, '.spe']);
plasmaInt=transpose(fread(fid, [1024, 1024], 'uint16'));
fclose(fid)

figure(1)
imagesc((1:1024), (1:1024), plasmaInt, [1000, 6000])
axis xy
axis image

```

```

colormap jet

% Loop to validate and improve no_resolve zone

flag=1;

while flag==1

    % Creates the zone with no resolve from interferogram

    no_resolve=imresize(roipoly, [1023, 1023]);

    % Determine line of symmetry location by summing perpendicular to

    % symmetry and determining location of the maximum of sums. NaNs must be

    % removed from data for sum() function.

    ZI_noNaN=ZI;

    ZI_noNaN(isnan(ZI_noNaN))=0;

    ZZI=ZI.*(1-no_resolve);

    ZZI(ZZI<=0)=0;

    [trash, data.center]=max(sum(ZI_noNaN, 2));

    % Cut fringe shift data along symmetry axis.

    data.set1 = ZI(data.center:end, :);

    data.set2 = flipud(ZI(1:data.center, :));

    data.length      =      [min([size(data.set1, 1)      size(data.set2, 1)])
size(data.set1, 2)];

```

```

% Smooth fringe shift data by averaging across symmetry axis.

N=zeros(data.length(1),data.length(2));

% As adding a number and NaN will result in NaN, must check if, while
% flipping, one of the values is NaN. If so, use only the other value, if
% both, set fringe shift to 0. Otherwise, average two numbers for
% smoothing.

for i=1:data.length(1)
    for j=1:data.length(2)
        N(i,j) = (data.set1(i,j)+data.set2(i,j))/2;
    end
end

% Gets the matrix that countains the NaNs
matrix_nan=isnan(N);

% Replaces all NaN with zeros, necessary for abel inversion program

for i=1:data.length(1)
    for j=1:data.length(2)
        if isnan(N(i,j))
            N(i,j)=0;
        end
    end
end

```

```

end

% Plots the matrix that will be passed to the abel inversion routine
figure(2)

imagesc(N)

% User may select the zone where data is irrelevant/incorrect (too
% close to the target surface).

no_resolve2=imresize(roipoly, [data.length(1), 1023]);

close all

figure(3)

imagesc(N.*(1-no_resolve2))

%ask if this part is OK

ButtonName=questdlg('Happy with the no_resolve zone?');

switch ButtonName

    case 'Yes'

        flag=0;

    case 'No'

        close

    case 'Cancel'

        return

end

```

```

end

N=N.*(1-no_resolve2);

%% ABEL INVERSION ROUTINE

% First, define the constants and necessary matrices

% Lambda used later and R must have same dimensions. Use centimeters.

R=data.length(1)*(YI(2,1)-YI(1,1))*1e-4;

% Create axis arrays r and y.

y=(0.0001:1:data.length(1))*(R/data.length(1));

r=y;

% knots = locations of endpoints for spline fits; change for better

% resolution

knots=0:.01*R:R;

g_calc=zeros(data.length(1),data.length(2));

progressbar;

% Call inversion algorithm.

disp 'Performing Abel inversion'

for i=1:data.length(2)

    progressbar(i/data.length(2));

    % N vector must be rotated to be a column vector.

```

```

    g_calc(:, i)=abel_inversion(r, rot90(N(:, i)), y, knots);
end

% Multiply by proper factors to obtain scaling of g(r) in cm-3.
lambda=46.9e-9;
lambda_microns=lambda*1e6;
lambda_cm=lambda*1e2;
n_cr=1.1e21/lambda_microns^2;
g_new=2*n_cr*lambda_cm*g_calc;

% Creates a meshgrid to read the data
rr=1e4*[flipud(r);r];
[xt, yt]=meshgrid(XI(1, :), rr);

% Plot inversion solution.
figure;

% Negative values may result from fittings, so remove for log plot.
h=g_new;
h(h<0)=NaN;
densities=[flipud(h);h];

% plots result of abel inversion
figure
pcolor(xt, yt, log10(densities));shading interp;colorbar;

```

```

set(gca, 'clim', [19, 22]);

% Saves the workspace in a MAT file
save(['abeldata_', timing])

%% Abel inversion algorithm.

function g_calc=abel_inversion(r, I, y, knots)

% Calculate necessary variables not passed through function call.
n=size(I, 2)+1;
R=max(r);
g=zeros(1, n-1);

% Create I_fit block with fit information.
% pieces = # of segments
% breaks = locations of endpoints of splines
I_fit.pieces=size(knots, 2)-1;
I_fit.breaks=knots;

% Fit segments with a cubic function and store coefficients.
%  $a*y^3 + b*y^2 + c*y + d$ 
for i=1:I_fit.pieces

```

```

[trash, start_loc] = min(abs(y-I_fit.breaks(i)));
[trash, end_loc] = min(abs(y-I_fit.breaks(i+1)));
I_fit.coefs(i,:) = polyfit(y(start_loc:end_loc),I(start_loc:end_loc),3);
end

%% ABEL INVERSION ALGORITHM %%
% See Deutsch and Beniaminy (1982) for exact expression. Note: algorithm as
% printed needs correction. See correction notes.
for i=1:n-2
    % Identify location of next break point.
    next=I_fit.breaks;
    next(next<r(i))=NaN;
    [trash,next_loc]=min(next);
    for j=next_loc:size(I_fit.breaks,2)-1
        g(i) = g(i) + I_fit.coefs(j,1)*(K4(I_fit.breaks(j+1),r(i))-
K4(I_fit.breaks(j),r(i))) + ...
            I_fit.coefs(j,2)*(K3(I_fit.breaks(j+1),r(i))-
K3(I_fit.breaks(j),r(i))) + ...
            I_fit.coefs(j,3)*(K2(I_fit.breaks(j+1),r(i))-
K2(I_fit.breaks(j),r(i))) + ...
            I_fit.coefs(j,4)*(K1(I_fit.breaks(j+1),r(i))-
K1(I_fit.breaks(j),r(i)));
    end

```

```

        g(i) = g(i) + I_fit.coefs(next_loc-1,1)*(K4(I_fit.breaks(next_loc),r(i))-
K4(r(i+1),r(i))) + ...
        I_fit.coefs(next_loc-1,2)*(K3(I_fit.breaks(next_loc),r(i))-
K3(r(i+1),r(i))) + ...
        I_fit.coefs(next_loc-1,3)*(K2(I_fit.breaks(next_loc),r(i))-
K2(r(i+1),r(i))) + ...
        I_fit.coefs(next_loc-1,4)*(K1(I_fit.breaks(next_loc),r(i))-
K1(r(i+1),r(i)));
        g(i) = g(i) +
(I_fit.coefs(end,1)*R^3+I_fit.coefs(end,2)*R^2+I_fit.coefs(end,3)*R+I_fit.coefs(end,4)
)/sqrt(R^2-r(i)^2) - ...
        (I_fit.coefs(next_loc-1,1)*r(i)^3+I_fit.coefs(next_loc-
1,2)*r(i)^2+I_fit.coefs(next_loc-1,3)*r(i)+I_fit.coefs(next_loc-1,4))/sqrt(r(i+1)^2-
r(i)^2);
    end

    g_calc=-g/pi;

function K1=K1(y,r)
s=sqrt(y^2-r^2);
K1=-1/s;

function K2=K2(y,r)
s=sqrt(y^2-r^2);

```

```
K2=-y/s+log(y+s);
```

```
function K3=K3(y,r)
```

```
s=sqrt(y^2-r^2);
```

```
K3=s-r^2/s;
```

```
function K4=K4(y,r)
```

```
s=sqrt(y^2-r^2);
```

```
K4=y*s/2-r^2*y/s+(3/2)*r^2*log(y+s);
```